ROMA
TRE
UNIVERSITÀ DEGLI STUDI

Engineering Department

_____

SCUOLA DOTTORALE / DOTTORATO DI RICERCA IN

XXV
_____
CICLO DEL CORSO DI DOTTORATO

Seismic Assessment of As-built and Isolated cases of an
Existing RC Bridge through Experimental PsD Testing
_____
Titolo della tesi

Arkam Mohamad

_____   _____
Nome e Cognome del dottorando   firma

Prof. Fabrizio Paolacci

_____   _____
Docente Guida/Tutor: Prof.   firma

Prof. Aldo Fiori

_____   _____
Coordinatore: Prof.   firma

Abstract

In Italy most of Infrastructures and highway bridge systems have been built before the issue of modern seismic design codes. Chiefly, the existing transportation systems that built in the late 60s and early 70s were designed primarily for gravity loads. As a result, such systems do not employ seismic details and hence their structural performance is inadequate under earthquake ground motions.

To decide for any retrofitting operation, the seismic behaviour of existing bridges must be assessed. Because the nonlinear procedures are becoming very popular in the frameworks of structural assessment, there is a need to accurately simulate authentic model to provide reliable indications about the performance required to this kind of structures.

Based on these observations, this thesis is devoted to the seismic assessment of existing RC bridges. In particular, the vulnerability of an old RC viaduct with portal frame piers equipped with plain steel bars has been numerically and experimentally investigated. Subsequently, the retrofitting has been evaluated using Friction Pendulum System isolation "FPS".

The nonlinear FE modelling has been executed using OpenSEES software framework. The local behaviour of the bridge has been taking into account, mainly, the bond-slip, strain penetration effect of the plain steel bars, bar buckling and the shear behaviour effect of the transverse beams of the portal frame piers.

Depending on a previous experimental campaign consisting of cyclically imposed displacements on 1:4 reduced scale models of a frame pier, belonging to the same RC highway viaduct, a new experimental activity has been proposed within the RETRO project funded by the European

Union. In particular, Two specimens (scale 1:2.5), 2 floors (total height is 5.8 m) and 3 floors (total height is 10.3 m) one-bay reinforced concrete frame respectively, were built and tested using the PsD technique with sub-structuring; the modelling of the entire viaduct is considered along with the non-linear behaviour of each pier.

During the test campaign, two different configurations for the analysed viaduct have been considered; "As-built" and "Isolated with Friction Bearings". The response of both cases has been compared to evaluate the effectiveness of the isolation system. To this end, two natural accelerograms were selected based on studying the seismiogenic zone of the bridge to represent, according to current seismic codes, the Serviceability and Ultimate limit states.

Analysis and interpretation of the experimental were achieved throughout the data recorded by the instrumentation used in the test campaign. The results have been used to calibrate numerical models and to provide a detailed analysis of the performance of the as-built configuration and to show the effectiveness of friction pendulum systems for seismic protection, which will ultimately lead to guidelines for the assessment and design of similar structures as part of pre-Normative research in support to the Eurocodes.

Keywords: Reinforced Concrete Bridges, Frame Piers, Plain steel bars, Numerical Simulation, Retrofitting of Bridges, Experimental investigation, Friction Pendulum System, PseudoDynamic Testing.

Preface

First and foremost I would like to thank my supervisor Prof. Fabrizio Paolacci for his extreme effort of help, advice and encouragement throughout my PhD study

Many thanks to University Roma Tre for awarding me the scholarship for PhD research study. I would like to circulate my thanks to all Engineering department faculty members, laboratory workers and all friends and colleagues for their encouragement and support.

I would like to recognize and thank the Joint Research Center for the invitation to work in ELSA laboratory during the experimental tests. I extend my thanks to all RETRO project team for their help and high collaboration.

Finally, I would like to thank my parents and family for their love, and endless moral support.

Acknowledgments

Table of Contents

List of Figures

List of Tables

List of Symbols

f_c	Compressive concrete stress
f'_{cc}	Compressive strength (peak stress) of confined concrete
f'_{co}	Compressive strength of unconfined concrete
ε_c	Longitudinal concrete strain
ε_{co}	Strain for unconfined concrete
ε_{cc}	Strain at maximum concrete stress
E_c	Initial modulus of elasticity of concrete
E_{sec}	Secant modulus of elasticity of concrete at peak stress
μ_f	Friction coefficient of the Isolator
R	FP device curvature radius
Δ_{iso}	Sliding displacement in the isolator
f'_t	Tensile strength of the concrete
A_c	Cross section area of Concrete
A_{sw}	Stirrups area
f_y	Steel strength
D	Distance between rebars at the top and bottom of the section
A_{sp}	Area of inclined rebars
P	Normal force
K_{eff}	Effective stiffness of the isolator
T_{eff}	Effective period of the isolator
K_{Geom}	Geometric stiffness of the scaled model
χ	Curvature
γ	Shear deformation

1. INTRODUCTION

1.1. Background and Motivation

The seismic vulnerability assessment of existing and new lifeline systems, especially transportation systems, is becoming of paramount importance in resilient social communities. Bridge systems and highways are primary elements that can be utilized for rescue operations in the aftermath of moderate-to-major earthquake ground motions. Most of today's existing transportation systems in Europe were built chiefly in the late 60s and early 70s and were designed primarily for gravity loads. As a result, such systems do not employ seismic details and hence their structural performance is inadequate under earthquake ground motions.

Recently, a comprehensive research program (Reluis DCP 2005-2008 – Research Thrust 3 –Prof. P.E. Pinto and G. Mancini) was initiated in Italy to formulate pre-normative European guidelines for the assessment of existing bridges. This novel program was motivated by the urgent needs to assess the seismic vulnerability and retrofit of existing bridge structures. The outcomes of the aforementioned research are summarized by Pinto & Mancini (2009). However, a number of design issues require further developments. The implementation of comprehensive guidelines for the seismic assessment and retrofit of existing bridges is time consuming, as it requires the thorough understating of complex local and global response mechanisms. Full scale testing programs should be employed to validate provisional models and to assess their reliability for parametric analyses. In the US it took more than ten years, dating back to the failures of modern bridges during the San Fernando (1971) earthquake, for the Federal Highway Administration (FHWA) to issue the "Retrofitting guidelines for Highway Bridges" (FHWA-ATC, 1983).

Since 1992, a refined research program funded by FHWA has been undertaken in the US to investigate a number of topics related to the seismic assessment and retrofit of bridges (FHWA 1995, FHWA-MCEER 2005). The European standards, i.e. Eurocodes, include a document for the seismic design of new bridges, namely Eurocode 8 Part 2. Part 3 of Eurocode 8 addresses existing buildings, but there is no part of Eurocode 8 covering existing bridges.

The assessment of the seismic vulnerability of existing bridges is a complex process. The assessment scheme requires a comprehensive dataset, which is often unavailable due to the lack of information, especially for reinforced concrete structures (adequate knowledge of the mechanical and geometrical characteristics of the structure and materials, information on structural modification occurred during the life of the bridge, a reliable estimation of the gravity load, etc.). These difficulties affect detrimentally the seismic response evaluation, and as a result, the structural vulnerability cannot be reliably estimated.

The evaluation of the expected seismic response of bridge structures is influenced by several uncertainties relative to mechanisms characterizing the post-elastic structural response. As a result, the effective use of methods and processing tools employing nonlinear analyses is often prohibitive and/or misleading. Nevertheless, non-linear procedures are becoming popular in the frameworks of structural assessment, thus, there is a need to accurately model the dissipative zones to provide reliable indications about the performance of the structure. In addition, the steel reinforcement of old constructions was comprised mainly by smooth steel bars. The influence of such bars in the response of the structure, especially their bond and anchorage mechanisms, has not been adequately investigated (both numerically and experimentally) in the past. Existing formulations simulating the behaviour of smooth bars and their anchorage shows that the existing experimental tests appear old and not comprehensive. Conversely, in recent years, this problem has been reconsidered and a systematic approach to the study of bond-slip and

anchorage efficiency of plain steel bars has been adopted (Fabbrocino et al. 2005, Feldman & Bartlett, 2005).

Another interesting issue is the rehabilitation of old bridges using innovative techniques. Seismic isolation is an effective way to reduce the response of bridges designed for vertical loads only. This technique, widely studied in the past, has been marginally investigated concerning its effectiveness on old bridges. In addition, further comparative analyses, numerical and experimental, are needed to better understand the performance of different isolation systems (Makris & Chang, 2000 Change et al. 2002).

Finally, the introduction of innovative retrofitting schemes, e.g. based on active/passive control technologies and application of FRPs in critical regions, call for models with predictive capacity. To do so, structural identification and monitoring are expected to play an important role. Considering that only a limited number of dynamic features of an existing bridge can be extracted from experimental modal analysis (Sohan et al. 2002), new non-linear identification techniques should be developed and tested in the future to capture the global dynamic response at the ultimate limit states (Bursi et al. 2009).

In view of the strategic nature of transportation infrastructures a further thorough study is becoming urgent and is deemed necessary. Towards this end, experimental test programs are vital to characterize the quality and quantity of typical structural systems (Verderame et al. 2009a-b, Marefat et al. 2009). Furthermore, a scarce experimental activity on old reinforced concrete structures renders this topic crucial for future assessment guidelines (Paolacci & Giannini, 2012, Arani et al. 2013). As a result, the state of the art on seismic assessment and retrofit of old bridges requires further advancement.

1.2. Objectives and Scope

According to the previous motivation and background, it is possible to conclude the aim of this study by investigating the seismic behaviour of existing reinforced concrete (RC) bridges and the effectiveness of innovative retrofitting systems. The research program focuses on old bridges, not properly designed for seismic action. In particular, the seismic vulnerability of an old Italian viaduct (Rio-Torto) with portal frame piers is evaluated. A proper isolation system has been designed using Slide Spherical Bearings. The non-linear response of the case study in "as-built" and "isolated" configurations has been tested through an experimental test campaign considering two prototype piers.

The experimental test campaign described herein follows a previous experimental campaign consisting of cyclically imposed displacements on 1:4 reduced scale models of a reinforced concrete portal frame pier, belonging to a typical old highway viaduct. In particular, two specimens (scale 1:2.5), a 2-level and a 3-level one-bay reinforced concrete frame, were constructed and tested using the pseudoDynamic (PsD) technique with sub-structuring, including the modelling of the entire viaduct. During the test, different configurations were considered, namely the retrofitted viaduct using Friction Pendulum Bearings and the "as-built" viaduct.

The main goals of the thesis are:

1)   Increase the knowledge on the non-linear behaviour of portal frame piers in presence of plain steel bars for which few studies have been carried out.
2)   Employment of large-scale experimental tests for the seismic assessment of existing bridges.
3)   Study of the effectiveness of traditional and innovative seismic isolation systems (FP isolators).

1.3.   Thesis Structure

This research is presented in 8 chapters as the follows:

Chapter 1 gives a background introduction about the motivations and scope of the research study. The seismic assessment state-of-the-art of existing bridges presented and the need of deep investigation regarding to a normative criteria discussed.

Chapter 2 shows the literature review about the seismic assessment of existing bridges by underlining the difference between existing and new structures and outlining the uncertainties difficulties of the existing bridges aspects. An overview on the national and international codes has been discussed.

In **Chapter 3**, the description of the case study "Rio-Torto" bridge has been presented. In particular, it comprises a description of the geometrical characteristics, material properties investigation and reinforcing steel bars. In addition, a brief study on the soil properties, seismogenic zone response spectra have been provided.

Chapter 4 presents the numerical modelling of Rio-Torto bridge procedure. The non-linear model simulation has been performed using Midas Gen and OpenSEES softwar. Firstly, The preliminary non-linear model including only the flexural behaviour of the bridge has been analysed using Midas Gen. Then, a refined model comprising the local behaviour of the elements (bond-slip of plain bars, nonlinear shear behaviour of transverse beams) has been built for both "as-built" and "isolated" cases using OpenSEES framework.

Chapter 5 analyses the seismic response of Rio-Torto Bridge through numerical simulations. A preliminary simulation of the seismic behaviour of the bridge in linear and non-linear field using simplified models was useful to provide a more clear view for the plan strategy of the

experimental campaign and the selection of the pier frames to be tested. The main non-linear analysis simulating the entire bridge at this stage is modal analysis and response spectrum analysis. Further, a focus analysis on piers under investigation "Pier 9 and 11" has been provided; specifically, static cyclic and dynamic analysis to give more confident response behaviour. Then, this chapter discusses the numerical analysis of the refined non-linear model using OpenSEES. Attention was paid on both "as-built" and "isolated" configurations, including the identification of input signals for both Serviceability and Ultimate Limit States.

Chapter 6 deals with the design aspects of the mock-ups piers. After a brief introduction on scaling problems and design criteria of isolators, the criterion and design of Pseudodynamic test setting up and instrumentations have been provided.

Chapter 7 discusses the experimental PsD tests and results of RETRO project campaign, starting from identifying the cyclic response of isolators. Then the results of the several seismic tests on isolated and non-isolated configuration are described and observations on global and local behaviour of the viaduct have been reported for each level of damage. Finally, comparisons of the different test results have been shown.

Chapter 8 reviews the conclusions of this study and outlines the orientation of future work.

2. LITERATURE REVIEW OF THE ASSESSMENT OF EXISTING BRIDGES

2.1. Introduction

The evaluation of the seismic vulnerability of an existing structure, and in particular for R.C. structure, is very different from that of a new structure, for several reasons:

➢ The geometrical characteristics are usually unknown due to lacking of design information (drawings, etc..)
➢ Inadequate knowledge of the mechanical characteristics of structure and materials.
➢ The design details, for example of the reinforcing bars placement, are very uncertain.
➢ A difficult and reliable estimation of the gravity loads.
➢ Lack of information about any structural modification occurred during the life of the bridge.

These difficulties have an important consequence: the practical difficulties to estimate the seismic vulnerability of such kind of structures.

➢ The evaluation of the expected seismic response of the bridge structures is conditioned by many uncertainties about the main mechanisms which characterize the post-elastic response.
➢ An effective utilization of methods and calculus instruments which imply non-linear analysis are difficult.

8

➢ Because non-linear analysis is becoming a popular analysis method, there is the necessity of correctly model the plasticization zones providing reliable indications about the performance required to the structure.

➢ In addition, the steel reinforcement of old constructions was often realized with plain steel bars, whose behaviour, especially regarding bond and anchorage, has not been widely investigated in the past.

The evaluation of the risk associated to the seismic vulnerability of the transportation infrastructure, and in particular to that of bridge structures has been the object of quite large number of researches. This has not been enough to stimulate the authorities to think about a code dedicated to the assessment of existing bridges. For the R.C. bridges in Italy, this is due to two main reasons:

➢ After the Friuli Earthquake (1976), limited damages have been observed in the bridges.

➢ After the Irpinia Earthquake (1980), the bridges on the Highway A16 suffered some damages, essentially due to inadequacy of the bearing devices, which has been changed with isolation devices

The delay in adopting specific technical codes for the assessment of the seismic risk of existing bridges is not only an Italian characteristic but it was all over the world. For example, in USA the first technical document on this subject was published by the Federal High Way Administration (FHWA), only after 24 years from the San Fernando earthquake (Fig 2.1), in spite of its inadequacy which was shown during the subsequent Earthquake of Loma Prieta (1989) (Fig. 2.2).

Figure 2.1 San Fernando Earthquake 1971

Figure 2.2 Loma Prieta Earthquake 1989 - Cypress viaduct

Even in Japan, usually considered a front-line country for what concerns the seismic problems, suffered very serious damages such as the damage happened during Kobe earthquake 1995 (Fig. 2.3).

Figure 2.3 Nishinomiya - Kobe Earthquake 1995

2.2. Typical seismic damages of bridges

Earthquakes cause damage to all structures, including bridges. Major earthquakes can bring about the collapse of dozens of buildings, but collapsed bridges are often the most visible signs of the havoc an earthquake can wreak. In general, the main reason of seismic damage could be due to insufficient seismic detailing which cause significant damage in the deck or columns or both of them.

Large sections of roadway may consist entirely of viaduct, sections with no connection to the earth other than through vertical columns. When concrete columns are used, the detailing is critical. Typical failure may be in the toppling of a row of columns due either to soil connection failure or to insufficient cylindrical wrapping with rebar. Both failures were seen in the 1995 Great Hanshin earthquake in Kobe, Japan (Fig. 2.4), where an entire viaduct, centrally supported by a single row of large columns, was laid down to one side.

In fact, ten spans of the Hanshin Expressway in three distinct location in Kobe and Nishinomiya were completely topples over, blocking a key link that carried 40% of two important cites "Oska-Kobe" road traffic. About

half of the elevated expressway's piers were damaged in some way, and the entire route stayed closed for 19 month.

Figure 2.4 Hanshin Expressway damage, Kobe, Japan (1995)

Sometimes viaducts may fail in the connections between components. This was seen in the failure of the Cypress Freeway in Oakland, California, during the Loma Prieta earthquake (Fig. 2.5). This viaduct was a two-level structure, and the upper portions of the columns were not well connected to the lower portions that supported the lower level; this caused the upper deck to collapse upon the lower deck.

Another example for deck damage is the East Bay Bridge in The Loma Prieta earthquake 1989 (Fig. 2.6). A 76-by-50-foot section of the upper deck on the eastern cantilever side fell onto the deck below. The quake caused the Oakland side of the bridge to shift 7 inches to the east, and caused the bolts of one section to shear off, sending the 250-short-ton section of roadbed crashing down like a house of cards. Immediately after Loma Prieta, the bridge was closed for a month as construction crews made repairs.

Figure 2.5 Cypress Freeway Viaduct collapse

Figure 2.6 East Bay Bridge Loma Prieta, 1989

Another important failure could happen is due to column piers. The damages of the piers are often due to the lack of ductility and/or shear strength of the sections like Gothic Avenue Viaduct in Northdridge Earthquake 1994 (Fig. 2.7).
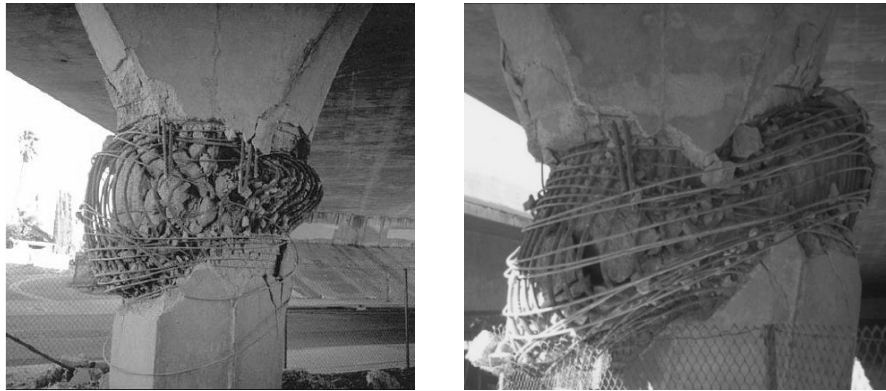
Figure 2.7 Gothic Avenue Viaduct, Northdridge 1994

Wishi Bridge also suffered the same shear failure of piers in Chi-Chi Earthquake 1999. It has 18 spans with a total length of 624.5 meters. This bridge is two parallel structures that were constructed during two different periods. The superstructure of the northbound bridge was constructed in 1981, but it used the original substructure (pier-wall type) that was constructed in the 1950s. The southbound bridge was completed in 1983. Both structures use PCI girders in their simply supported superstructures, and both have pier-wall-type substructures. The fault rupture occurred behind and under the northern abutments of both bridges. Although the two bridges suffered similar ground motions, they failed in different ways. The first and second spans of the older bridge (northbound) collapsed. This failure was due to the fault rupture, which caused a large ground movement, pushing the superstructure back and forth until it fell down from the "seats" atop the piers.

The bearings also failed due to large compression forces. The third pier of the northbound bridge was uplifted also. Both superstructures may have collided during the earthquake, causing some damage to the substructures. The piers of the northbound bridge suffered tension cracking and fractured, and the southbound bridge piers had severe shear cracks and failures (Fig. 2.8).

Figure 2.8 Wushi viaduct Chi-Chi, Taiwan 1999

The viaduct or the failure of the nodes of frame piers is also spreads in RC frame piers bridges due to inadequate seismic details of the connections such as in Shinkansen Viaduct, Kobe, 1995 (Fig 2.9).

Figure 2.9 Shinkansen Viaduct Kobe, 1995

2.3. National and International codes

Starting from the year 1992 a vast research program has been undertaken in the US (funded by the FHWA) to study several aspects related to the seismic assessment and retrofit of bridges.

The products of the above research are:

➢ Seismic Retrofit Manual for Highway Bridges" (FHWA, 1995).
➢ Seismic Retrofitting Manual for Highway Structures: Part 1 Bridges" (FHWA- MCEER, 2005).
➢ "Seismic Retrofitting Manual for Highway Structures: Part 2 Retaining structures, Slopes, Tunnels, Culverts and Roadways" (FHWA- MCEER, 2005).

In Europe the Eurocodes system includes a normative document for the seismic design of new bridges, which is at least partially based on the recent concepts of performance-based design: Eurocode 8 Part 2. For the existing structures, there is the Eurocode 8 part 3 that regards only existing buildings.

In Italy there are two main documents regarding existing buildings OPCM 3441 and NTC 2008. But there is nothing regarding existing bridges.

Within a wide research program funded by RELUIS and in particular from the research line 3 (existing bridges) new guidelines of existing bridges has been proposed.

2.4. Performance-Based Earthquake Engineering

Traditional design practice (code-based design) focuses on limiting displacements and forces to the levels indicated in codes. This is easy to understand for engineers and leads to straightforward design methods. This is the so called prescriptive approach. However, other stakeholders

(owner, architects, etc..) of the design process may not be familiar with these engineering measurements and this makes it hard to communicate to them the quality of the designed structure.

Earthquake engineering practice is undergoing drastic changes triggered by a variety of reasons. (knowledge about earthquake occurrences, ground motion, structural response characteristics..). It is widely acknowledged that seismic design should explicitly considers multiple performance objectives. There is a minimum level of required protection by society in order to safeguard adequately against partial collapse that could have series consequences on human lives (OLD). But there are other responsibilities in addition to life safety, including continuing operation of critical facilities, protection against the discharge of hazardous materials, and protection against excessive damage that may have important consequences for society on a local, regional, national, or international level.

Performance-based earthquake engineering (PBEE) is a new design approach that implies design, evaluation, and construction of engineered facilities whose performance under common and extreme loads responds to the several needs and objectives of owners, users and society. PBEE is based on the principle that performance can be predicted and evaluated with quantifiable confidence in order to make, together with the costumer, intelligent and informed trade-offs based on life-cycle considerations, rather than construction costs alone (Zarieian & Krawinkler 2006).

When a Performance-Based Design is carried out, the engineer will be able to communicate with the stakeholders in terms they understand clearly, such as the expected annual costs of repair or the annual saving that would result from using a given retrofit strategy (Fig. 2.10).
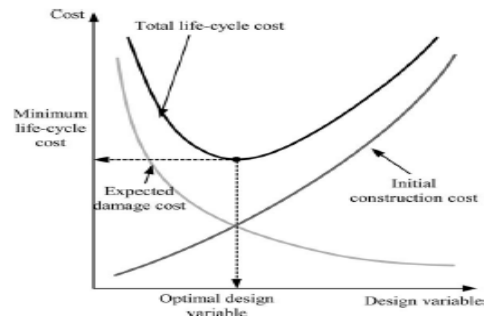
Figure 2.10 Total life-cycle cost curve

Performance objectives are quantified usually based on life-cycle cost considerations, which include various parameters affecting structural performance, such as, structural, non-structural or contents damage, and human casualties.

To guarantee a reliable confidence in predicting the performances of a structure, a probabilistic approach to the problem is required. So far, the uncertainties have been taken into account explicitly by partial safety coefficients and implicitly with a general conservative approach to design structures (for example, models for the cross-sectional capacity of reinforced concrete members have traditionally a conservative bias to account for unavoidable model uncertainty: the plane section hypothesis).

Moreover a cost-benefit is not usually accounted. For these reasons a great effort has been made in the past in defining a new design philosophy able to take into account all the uncertainties.

2.5. Code and Standards for PBEE

One of the guidelines that studying the PBEE is the NEHRP Guidelines and Commentary for Seismic Rehabilitation of Buildings (FEMA Publication 273, 1997) which has been funded in the 1990's by Federal Emergency Management Agency (FEMA), the Applied Technology Council (ATC) and Building Seismic Safety Council (BSSC).

This development effort marked a major milestone in the evolution of performance-based seismic design procedures and articulated several important earthquake-related concepts essential to a performance-based procedure. The key concept was the definition of performance objectives, consisting of the specification of the design event (earthquake hazard), which the building is to be designed to resist, and a permissible level of damage (performance level).

Another important feature was the introduction of standard performance levels, which quantified levels of structural and nonstructural damage, based on values of standard structural response parameters.

Performance levels are defined in terms of global performance, as global displacements (e.g. roof displacements). These levels are associated to a certain probability of occurrence of the seismic action (Fig. 2.11).
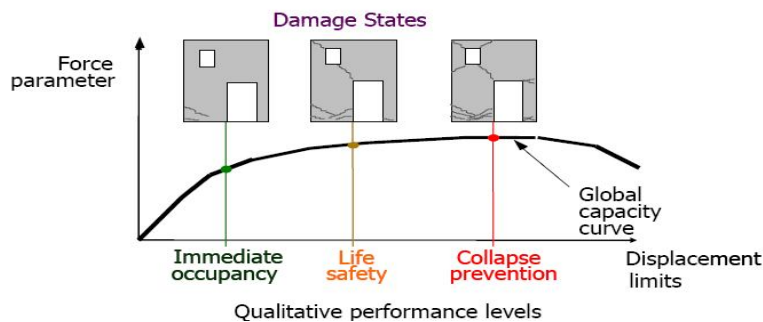
Figure 2.11 Damage states at different qualitative performance levels

Another projects extended the method developed in FEMA-273/274. In particular: ATC-40, Methodology for Evaluation and Upgrade of Concrete Buildings and Vision-2000 Framework for Performance-based Seismic Design Project (Fig. 2.12).

These technologies were further refined by the American Society of Civil Engineers in their conversion of the FEMA-273/274 reports into the Pre-standard for Seismic Rehabilitation of Buildings, the well known FEMA-356.

Together, the FEMA-356, ATC-40, and Vision-2000 documents define the current state of practice of the First-Generation Performance-Based Seismic Engineering (FG-PBEE). It is clear that this approach in essentially deterministic and by the time it becomes implemented in most of the codes and standards such as (EN1998 – NTC2008).
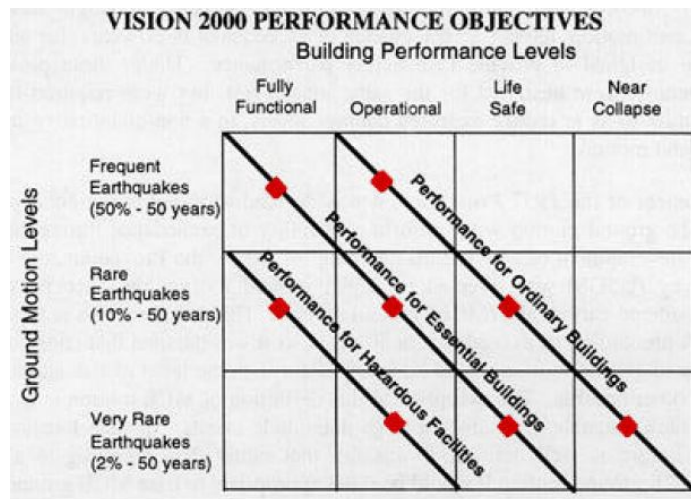
Figure 2.12 Building performance levels in Vision 2000 performance

The recognized randomness of the several variables included in the Performed-based Earthquake Engineering approach has induced the scientific community to develop a full- probabilistic version of PBEE, the so called Next-generation PBEE. For this reason FEMA sponsored a large project (widely known as the SAC Steel Project) to develop seismic evaluation and design criteria for that class of buildings. Key products of the project included a series of recommended design criteria documents included probabilistic nature of the problem (FEMA-350)

FEMA has also contracted with the Applied Technology Council (ATC) to develop a next generation of performance-based seismic design guidelines for buildings, a project known as ATC-58. Although focused primarily on design to resist earthquake effects, the next generation

performance guidelines will be compatible with performance-based procedures being developed at this time for other hazards including fire and blast.

The philosophy of FEMA-58 has been fully-implemented in the PEER approach (Pacific Earthquake Engineering Research Center). The procedure provide the mean rate of exceeding (probability of occurrence in a given time) of a so called Decision Variable (DV). An example of a DV for building evaluation is mean annual loss, for bridges the critical DV is the likelihood of closure of the facility (Fig. 2.13).
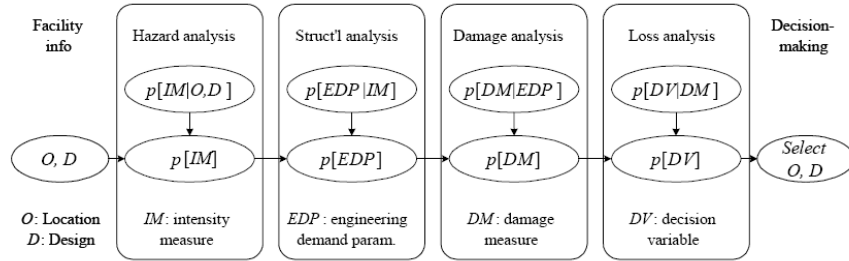
Figure 2.13 Decision making for building evaluation depending on Decision Variable

In this approach all the randomness are taken into account:

➤ Randomness of seismic input (Hazard Analysis)
➤ Randomness of structural response (Structural Analysis)
➤ Randomness of the Structural Capacity (Damage Analysis)
➤ Randomness of objective function (Loss analysis)

It is possible to present the previous randomness within this equation:

$$\lambda(DV) = \int_0^\infty \int_0^\infty \int_0^\infty G(DV \mid DM)\, \left|dG(DM \mid EDP)\right| \left|dG(EDP \mid IM)\right| \left|d\lambda(IM)\right|$$

2.6. Description of RETRO project

This thesis study focuses on the non-linear numerical modelling and seismic response analysis of the existing RC bridges in order to increase the knowledge of Assessment of existing RC bridges. For this reason it comes as part of RETRO project briefly described in this section.

RETRO project is a new experimental campaign that studies the "Assessment of the seismic vulnerability of an old **R**.c viaduct with frame piers and study of the **E**ffectiveness of different isolation systems through Pseudodynamic **T**est on a la**R**ge scale m**O**del". This project comes because of the urgent need to investigate the seismic behaviour of old RC bridge widespread in Italy.

The project is funded by the Seismic Engineering Research Infrastructure for European Synergies "SERIES", where the experimental activates have been performed in the European Laboratory for Structural Assessment "ELSA" at the Joint Research Center "JRC" in Ispra, Italy (http://www.series.upatras.gr). RETRO project extended from 2010 to 2013 and six universities have been involved:

- ➢ University Roma Tre
- ➢ University of Patras
- ➢ University of Naples and Sannio
- ➢ Politecnico di Torino
- ➢ Univertsity of Bogazici
- ➢ ALGA Spa Milan

In the aforementioned project, a case study bridge with frame piers "Rio-Torto Bridge" has been chosen to be studied because of its high seismic vulnerability. In particular, two specimens of scale 1:2.5 of frame piers belonging to a typical RC highway viaduct have been tested using the PseudoDynamic technique with sub-structuring, as shown in (Fig. 2.14).

The first specimen is a frame pier of 2 levels (height 5.8 m) and the second is frame pier of 3 levels (height 10.3 m).
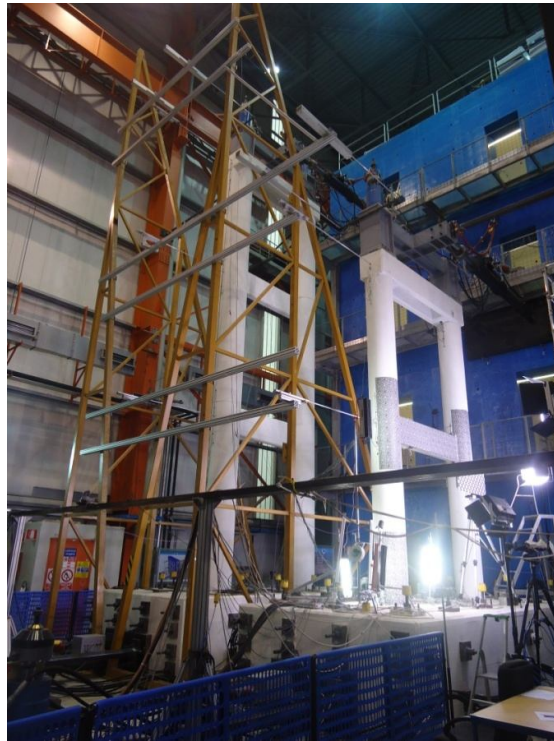
Figure 2.14 RETRO project frame piers tested at ELSA

The objectives of the project are: increasing the knowledge on the non-linear behaviour of RC frame piers and studying the effectiveness of different seismic isolation systems. The strategic aim is to provide comprehensive guidelines for the seismic assessment and retrofit of existing bridges.

In more specific, the RETRO research activities aim to:

1. Improve the knowledge on the seismic behaviour of old bridges with frame piers and in particular:

a. Study of the local behaviours (bond-slip, strain-penetration effect, bars buckling, etc...), especially under cyclic loading.
b. Assessment of the dynamic behaviour of an entire viaduct and evaluation of the seismic vulnerability using PsD technique with sub-structuring.
c. Study of the reliability of existing models for the simulation of the seismic behaviour of this kind of bridges.

2. Analysis of the effectiveness of the seismic isolation systems for old bridges, and in particular:

a. Critical analysis of the proposed design methods of isolation systems already present in literature, especially under optimization and in presence of an asynchronous ground motion.
b. Proposal of an alternative design method based on the Performance Based Engineering and optimization concepts.
c. Experimental evaluation of two isolation systems using PsD technique with substructuring: Spherical Sliding Bearings.
d. Numerical simulation of the seismic response of the tested bridge with and without isolation systems.
e. Numerical experimental comparison of the effectiveness of the isolation systems.

2.7. ReLUIS campaign analysis and testing (2005-2008)

RETRO project was proposed in the light of the results of a comprehensive research program (Reluis DCP 2005 - 2008) that was initiated in Italy to formulate pre-normative European guidelines for the assessment of existing bridges. This work was devoted to experimental activities on large-scale models of portal frame bridge piers, highly vulnerable to seismic action (Paolacci & Giannini, 2011).

The tests conducted piers belong to "Rio-Torto"; an old Italian viaduct on the Florence-Bologna highway. The specimens used are three identical 1:4 one-bay two-floor reinforced concrete frames built using plain steel bars for pier 12. The selected scale, mainly mandated by the laboratory infrastructure, is compatible with the nonlinear phenomena expected in the analyzed pier.

2.7.1. Reluis Case study and specimens

The preliminary analysis on the dynamic behaviour for pier 12 shows a critical condition in terms of flexural and shear capacity of columns and transverse beam against earthquakes, thus making it particularly suitable for an experimental campaign. The pier has two columns of diameter D=120cm, with a longitudinal and transverse reinforcement consisting, respectively, of 16 plain steel bars ϕ 20mm and spiral stirrups ϕ 6mm with spacing s = 14 cm. The transverse beam has a rectangular section 40*130 cm with a symmetrical longitudinal reinforcement realized with $10 + 10\ \phi$ 20mm, reduced in the middle of the beam to $6 + 6\ \phi$ 20mm, and stirrups ϕ 8mm with variable spacing (s=10cm at nodes and s = 14 cm in the middle). The cap-beam presents a U-shaped section with top and bottom longitudinal reinforcement $4\ \phi\ 24 + 8\ \phi$ 20mm and stirrups ϕ 8mm with variable step.

The three 1:4 scale mock-up's of pier 12 have been built to carry out quasi-static cyclic tests. Each pier is a reinforced concrete frame, 3.5m high, consisting of two circular columns of diameter D= 30 cm, a transverse beam with a rectangular section 10*32.5 cm placed at mid height (1.75 m), and finally an inverted U-shaped cap beam. The foundation is a rectangular beam with section 30*60 cm. The reinforcement details are shown in (Fig. 2.15).
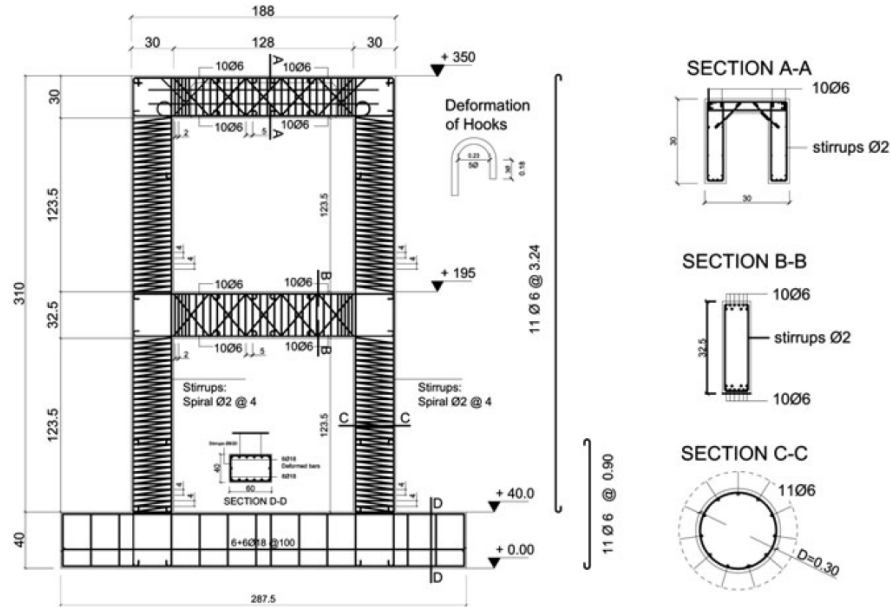
Figure 2.15 Reinforcement layout and cross section of Pier 12 (dimensions in cm)

Non scaled concrete and steel reinforcing bars ϕ 6 and ϕ 2 were used to respect the similitude requirements (Krawinkler et al. 1988). Actually, while the similitude requirements for the flexural behaviour and the confinement were fully respected, for the shear this was not totally true, where the diameter of stirrups was slightly larger than the required one. For example, for the columns a diameter of 2mm was used in lieu of 1.64 mm. This acceptable approximation was dictated by the minimum diameter available on the market (2mm). Similar conclusions can be drawn for the transverse beam.

More delicate is the scaling effect on concrete–steel bond conditions. Past experimental tests have shown that the scaling may have a relevant influence on the bond of deformed bars, especially in terms of slippage and cracks propagation (Ichinose & Kanayamab, 2004). In the case of plain steel bars, its influence can be still considered significant (Bazant & Sener, 1988, Pinto & Mancini, 2009), but because the experimental evidence has proved that in this case the anchorage effect of hooks

prevails (Fabbrocino & Verderame, 2005), the simple geometrical scaling can be accepted.

As far as the experimental test of the mock-up is concerned, horizontal displacement imposed at the top of the pier in quasi-static manner has been applied using a 250-kN hydraulic actuator in displacement control. The foundation of the mock-up is anchored to the laboratory base concrete slab using anchor bars (Fig. 2.16).
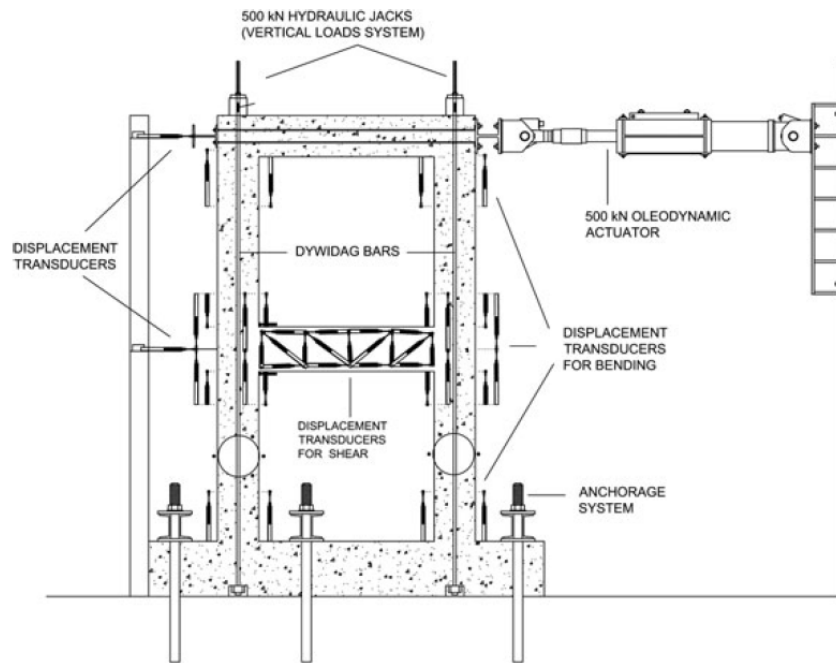
Figure 2.16 Pier 12 experimental test setup

Vertical loads are simulated by prestressing forces applied to the columns using ϕ 24mm Dywidag bars and measured by two 500 kN load cells. Because in the last two tests a greater number of channels were available, a larger number of sensors were used. In particular, a net of sensors was placed on the transverse beam to measure the eventual shear cracking

width. The complete scheme of the sensors for the specimens #2 and #3 is shown in (Fig. 2.17).

The displacements along the height and the horizontal force applied at the top were measured using draw wire transducers (Fig. 2.17a) and a 250-kN load cell, respectively, whereas the mean curvature at the columns and beam edges was monitored using pairs of longitudinal linear potentiometers with lengths B1 and B2, equal to 30 cm (Fig. 2.17b).
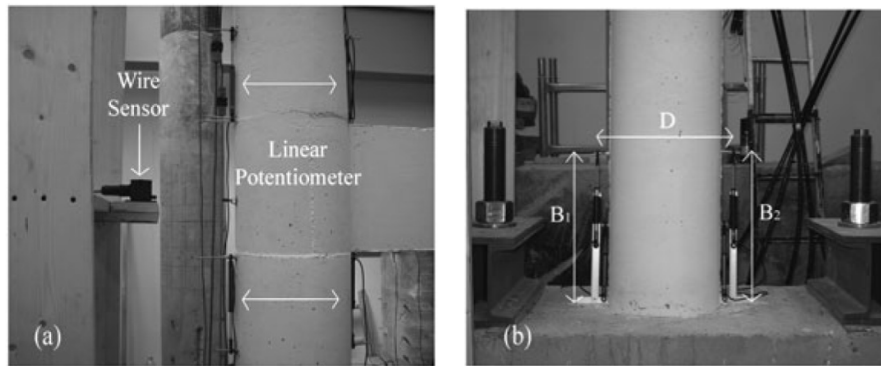
Figure 2.17 (a) Linear potentiometer at a beam–column joint and, (b) linear potentiometer at a column base

2.7.2 Reluis campgin results

The experimental test on the piers consists of displacements cyclically imposed at the top of the specimen. The time-history of the displacements is shown in (Fig. 2.18a). The amplitude of the cycles varies from 0.1mm to 60 mm, and for each amplitude three cycles of displacements have been imposed, for a total number of 52 cycles. The frequency of the applied signal is equal to 0.05Hz to realize a quasi-static test. The dead load acting on the real scale pier is equal to 6600 kN; therefore, a vertical load of about 200 kN has been applied to each column using the prestressing system previously described (Pinto & Molina, 2003).

The dead loads were expected to be constant for simulating the effects of an earthquake, in case of the absence of the vertical component of the

acceleration. Actually, because of an inaccurate control of the pressure in the actuators, the load cells have recorded a time-variable force, with the same frequency as the applied horizontal displacements (Fig. 2.18b). The two vertical forces are out of phase, showing an initial value of 200 kN and maximum and minimum equal to 260 kN and 190 kN, respectively.
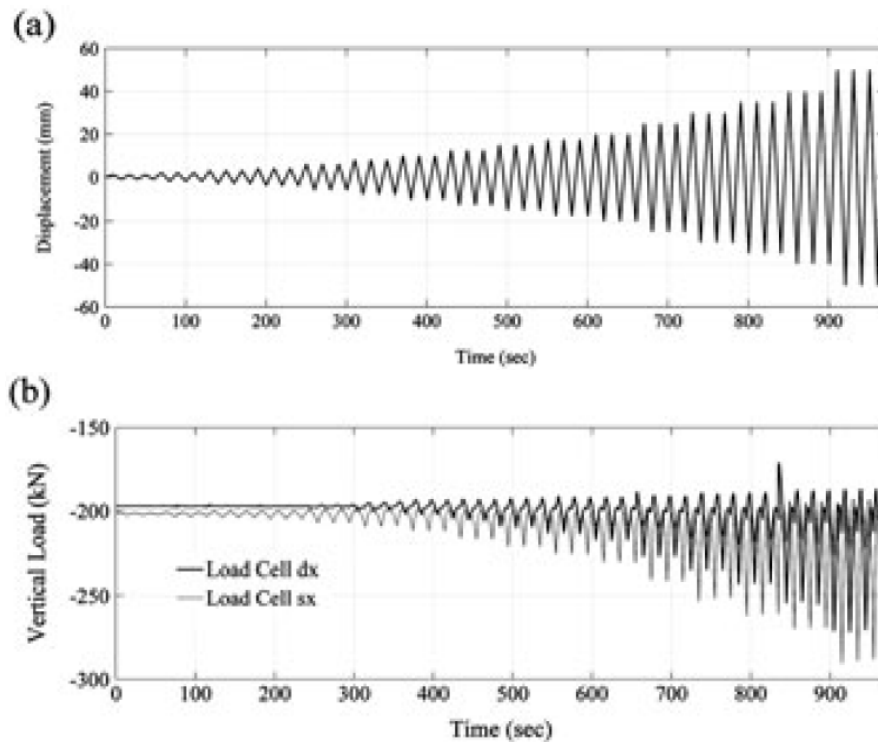
Figure 2.18 (a) Time-history of the imposed displacements, (b) time-history of the vertical loads

The time-history is not symmetric and shows an increasing average value. The global cyclic behaviour measured in the experimental test during the first six cycles is, as expected, quite linear, even if a reduced dissipated energy, probably because of an initial settlement of the specimen, was observed. In Figures 2.19a and 2.19b the complete cyclic history of the three specimens is shown. Because the cycles are symmetric, only the behaviour for positive forces and displacements is commented. For

negative values similar conclusions may be drawn. As far as the shape of cycles is concerned, a marked pinching is observed, which shows that the behaviour is dominated by low dissipation mechanisms. For high values of displacements a decreasing of the global stiffness has also been observed, whereas, a limited degradation in terms of force has been identified for cycles with the same amplitude.
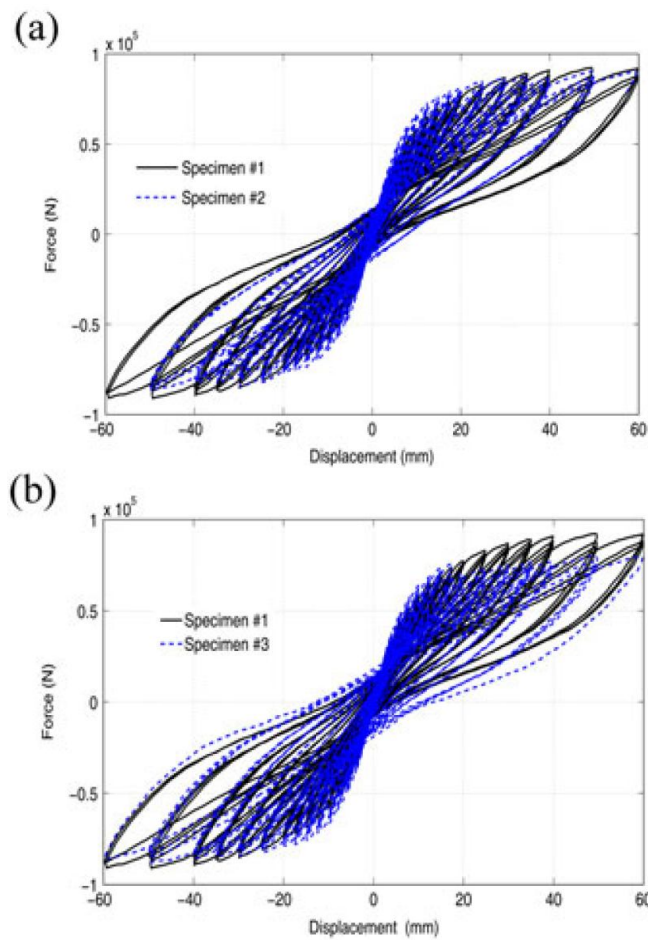
Figure 2.19 Force-deflection response: (a) specimens #1 and #2, (b) specimen #1 and #3

The damage mechanism of three specimens is about the same: cracks opening at the bottom and top of the columns, followed by the failure of the transverse beam. The latter occurred in three different ways; in the first specimen a clear shear failure occurred in the proximity of both edges of the transverse beam (Fig. 2.20a) together with the formation of flexural cracks at the base of the columns (Fig 2.20b). In the second specimen both the beam–column joints of the first level failed (Fig. 2.20c), whereas in the third specimen a shear failure of the transverse beam (left edge) occurred nearly contemporaneously with the failure of the beam–column joint on the right. The alternate failure of transverse beam and nodes means that the two concurrent mechanisms have very similar resistances; small random differences in the concrete cast or in the positioning of the steel bars could induce different damage mechanisms.
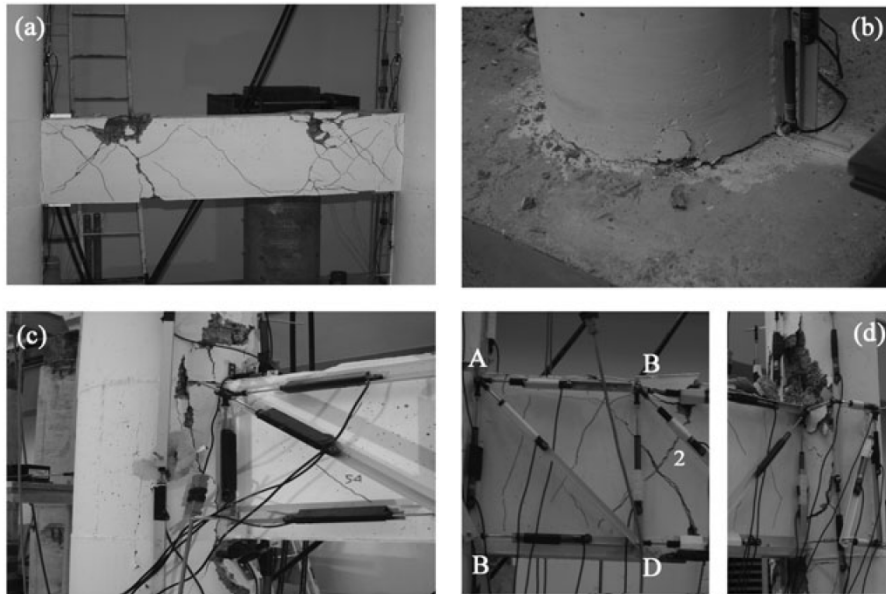
Figure 2.20 (a) Shear cracking pattern of the transverse beam of specimen #1; (b) crack at the base of a column of specimen#1; (c) failure of both the joints of specimen #2; and (d) failure mode of specimen #3: shear failure of the transverse beam and joint

The presence of the sensors for measuring the cracking pattern on the transverse beam of specimen #2 and #3 has made it possible to analyze their shear behaviour, as described in detail in the following section. Actually, only specimen #3 has suffered serious shear damage in the transverse beam. The shear cracking pattern is shown in (Fig. 2.20d), where the two major inclined cracks (1,2) resulting from the cyclic action may be observed, whose angle of inclination is about 60°.
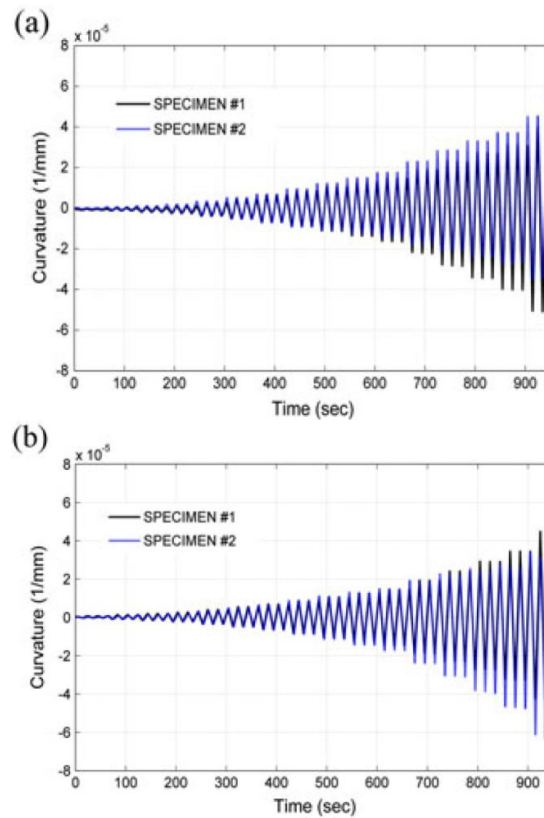
Figure 2.21 Curvature of the columns at bottom section: (a) left column and (b) right column

In addition, the curvature calculated at the bottom section of the columns is shown in (Fig. 2.21a and 2.21b) for #1 and #2 respectively. The slight differences between the signals again show that the different failure

modes of the transverse beam do not have significant influence on the behaviour of the three piers. For the interpretation of the local measurements a comparison with a numerical model is required. For this reason, in the next section the above results will be discussed in detail using a very complete model implemented in the nonlinear analysis code OpenSEES.

However, from the analysis of the experimental behaviour of the three specimens, the following preliminary conclusions may be drawn:

a) The behaviour is stable during the repetition of the cycles, proving that the degradation depends mainly on the amplitude of the cycles and not on the dissipated energy;

b) The maximum force, with the exception of the third specimen, grows continuously with the displacement, whereas, within the maximum amplitudes (drift ~2%), only degradation phenomena in terms of stiffness were observed;

c) In spite of the different failure mechanisms of the transverse beam, all three specimens have shown a similar global behaviour; only in the last test a lower strength was observed, together with a less evident pinching effect;

d) Another contribution to global hysteresis behaviour is due to the strain penetration effect, as it will be highlighted in more detail in the following section where numerical experimental comparison will be shown. In fact, it is well known that for equal flexural moment, bond-slip produces a local decrease of deformation of the elements and at the same time induces rigid rotations of the joints, and thus more flexibility.

e) During the tests, other local damage phenomena have also been observed, in particular, cracks at the column-foundation interface,

column-transverse and column-cap beam joints. Moreover, a slight buckling phenomenon of the longitudinal bars of the columns was detected, which is due to relatively wide stirrup spacing.

On the basis of Reluis results, RETRO project proposed to increase the knowledge about the seismic performance of Existing RC bridges. The same bridge has been chosen to be studied and tested. The following chapters presents the research activates of seismic response of Rio-Torto bridge including numerical modeling aspects, design of the mock-ups and design of PsD test campaign.

3. DESCRIPTION OF THE CASE STUDY "RIO-TORTO" BRIDGE

This chapter showing an overview about the case study Rio-Torto bridge. The portal frame bridge was chosen because of its high vulnerability to the seismic action. The chapter will discuss the Geometrical characteristics, the materials properties, an estimation of the load and reinforcement details of the steel rebars.

In addition, the soil conditions and the seismogenic zone have been illustrated by showing the life safety conditions and the response spectra according to the Italian code.

3.1. Geometrical characteristics of Rio-Torto Bridge

The bridge object of this study is an old reinforced concrete viaduct consisting of a thirteen-span bay deck with two independent roadways sustained by 12 couples of portal frame piers (Fig. 3.1), each of these piers composed of two solid or hollow circular columns of variable diameter (120-160 cm), connected at the top by a cap-beam and at various heights by one or more transverse beams of rectangular section (Fig 3.2).

Figure 3.1 Longitudinal view of the viaduct Rio-Torto
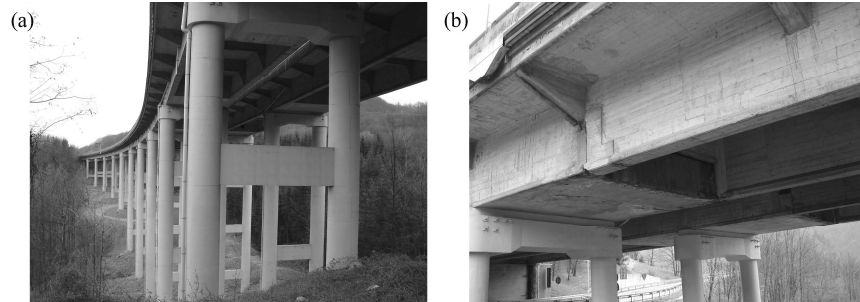
Figure 3.2 (a) A view of the bridge, (b) Detail of the deck

The height of the piers varies between 13.8m, near the abutments, to 41 m, at the centre of the bridge. The deck is constructed by two "∏" shape reinforced concrete beams 2.75m high (Fig. 3.3) interrupted by Gerber saddles (Fig. 3.4) placed at the second, seventh and twelfth bays. The deck is connected to the piers by two steel bars inserted in the concrete, whereas the bearings at the abutments are constructed with fixed devices.
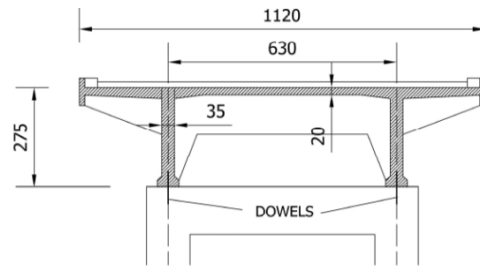
Figure 3.3 Cross-section of the deck

Figure 3.4 Garber Saddles

The cross section properties of the deck are given in (table 3.1) illustrated in following:

Table 3.1 Deck characteristics

Area [m^2]	J [m^4]	I$_y$ [m^4]	Iz [m^4]
4.6621	0132375	51.87	3.466

36

The columns have two types of cross-sections: a solid circular one with diameter of 120 cm and a hollow section with external and internal diameters equal to 160 cm and 100 cm respectively. Geometry and details of the longitudinal steel bars in these two sections are illustrated in (Fig. 3.5) for piers 9 and 11.
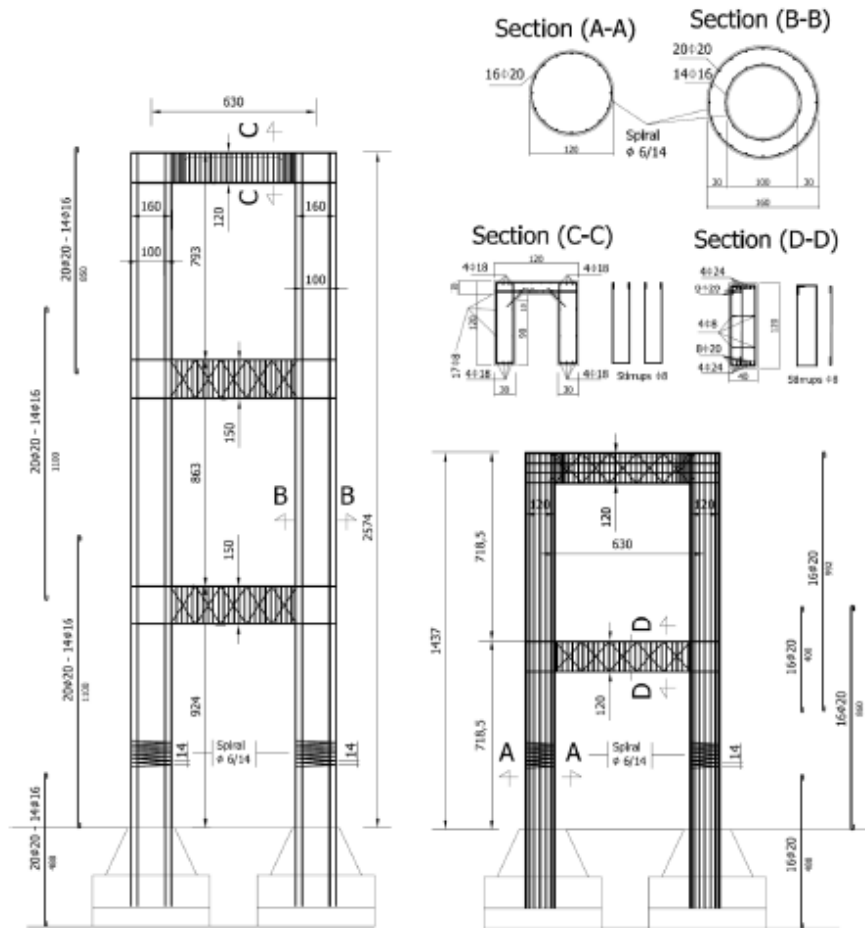
Figure 3.5 Reinforcement details of pier 9 and 11

In order to carry out the PsD test of the viaduct with sub-structuring, piers 9 and 11 were reproduced at a scale of 1:2.5, whereas the remaining part

of the viaduct was numerically simulated. The details of the geometry of each pier can be found in (Paolacci & Mohamad, 2010). The overall dimensions of the piers are illustrated in (Fig. 3.6).
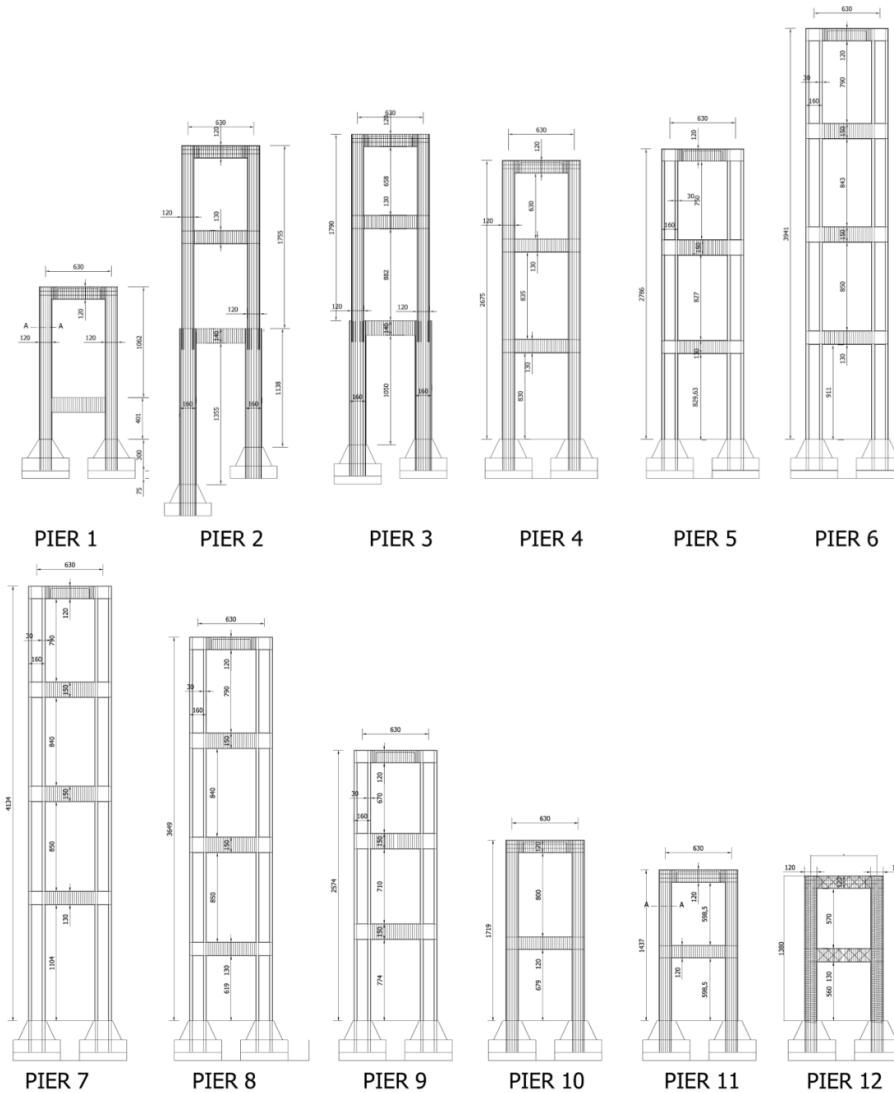
Figure 3.6 Overall dimensions of all piers (full scale)

3.2. Material properties

Limited data about the materials used in the bridge is available. The only information known is the class of concrete corresponds to a mean resistance of 30 MPa, while the class of steel used in Italy when the bridge was constructed was AQ42, corresponding to a mean strength of 350 MPa (Verderame & Stella, 2001). To increase the knowledge on the material properties of the bridge, in-situ tests should have been carried out. More detailed discussion about characterization of steel rebars used for constructing the specimens will be held in section 6.5.

The bond mechanism of straight steel bars and bars with circular hooks was characterized by pull-out tests within an experimental campaign carried out at the University Roma Tre (Paolacci & Gennini, 2012). The tests consist of static displacements applied monotonically to a 10 mm steel bar anchored in a concrete block; a plastic pipe is used to avoid interaction between the rebar and the surrounding concrete except in the embedded zone, equal to 10 diameters of the bar. The force in the bar and the slip between the bar and concrete were continuously measured during the tests using a load cell and a linear potentiometer in conjunction with an extensometer. Figure 3.7 and 3.8 show one of the specimens during the preparation phase and the set-up of the pull-out test.

Figure 3.7 Preparation of the specimens
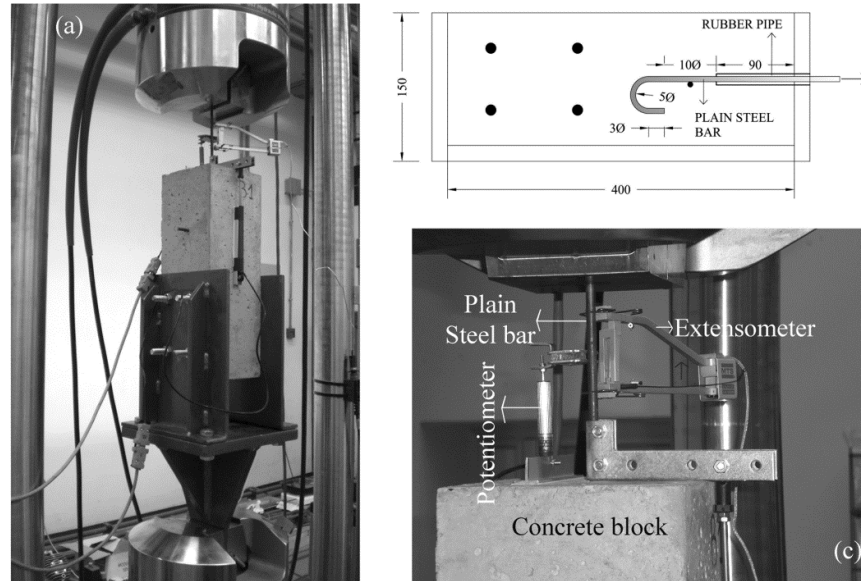
Figure 3.8 Set-up of the pull-out test

The significant parameters of the stress-slip law of the anchorage device will be identified; An example of stress-slip law is shown in (Fig. 3.9), derived in a previous experimental campaign for the case without (Fig. 3.9a) and with end-circular hook (Fig. 3.9b) respectively. Figure 3.9a shows the applied load versus slip at the loaded end of the bar for pullout specimens; the load-slip curves displayed a characteristic shape: the maximum tensile load occurred at a very small slip and then dropped asymptotically to a residual value as the slip increased. The residual value of the bond stress, representing the friction-based force between bar and concrete, is variable with a mean of 1.5 MPa. This value is in agreement with theoretical bond stress–slip relationship suggested by Model Code 90 (MC90), already shown in (Fig. 3.9a), (Paolacci & Gennini, 2012).

Figure 3.9b shows the stress-slip relationship as proof of the efficiency of the anchorage device. The yielding of the bar is fully reached, even if an important slippage is observed. In particular, in proximity with the yielding condition a slippage of about 0.5 mm was measured, whereas for

ultimate conditions a relevant slippage, greater than 10 mm, was noted. Similar interesting test campaign may be found in (Fabbrocino & Verderame, 2005).
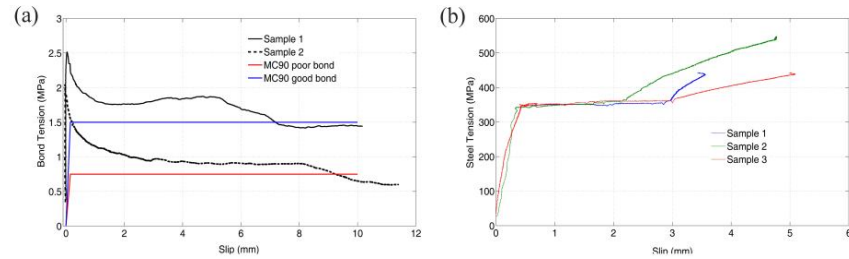
Figure 3.9 Results of the previous experimental campaign at University Roma Tre

3.3. Vertical loads

The distributed weight of the single component of the deck is indicated in the following Table 3.2:

Table 3.2 Vertical loads

Element	Thickness [m]	Area [m^2]	Volume weight [kN/m^3]	Total weight [kN/m]
R.C. Deck	--	4.48	25	112
Slab				6
Stiffeners				10
Concrete asphalt (thickness 15 cm)	0.15	2	24	30
Guard Rail	--	--	--	2
Waterproofing membrane	0.04	0.5	20	1
Parapet				5
TOTAL				≈ 170 kN/m

This means that to each pier a vertical load variable between 5600 kN and 7140 kN is applied, being the length of the bays variable between 33 and 42 m. Thus, the total weight acting on the piers 9 and 11 is equal to 5600 kN (2800 kN for each column).

3.4. Reinforcement details of the piers

The details on the placement of the longitudinal steel bars in the solid and hollow circular sections of the columns are illustrated in (Fig. 3.10). The solid section has bars ϕ 16 mm, whereas the hollow section has ϕ 16 and ϕ 14 mm steel bars, externally and internally, respectively. The transverse reinforcement for all the columns consists of a ϕ 6 mm steel spiral with a spacing of 14 mm.
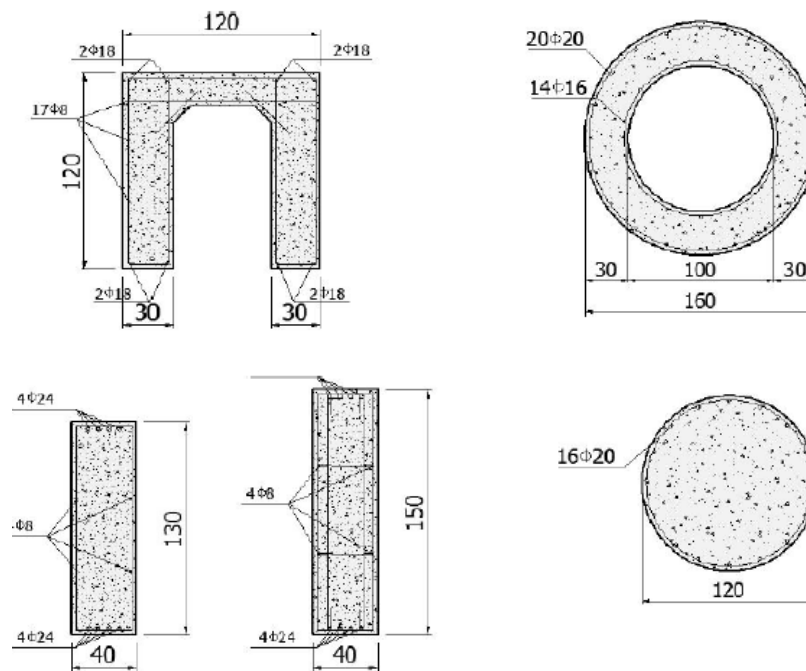
Figure 3.10 Full-scale cross-sections of the cap-beam, transverse and the columns

The transverse beams have a rectangular section with a width of 40 cm and a height varying between 120 cm and 150 cm. The longitudinal reinforcement consists of ϕ 24 and ϕ20 steel bars. The transverse

reinforcement consists of ɸ 8 steel bars spaced at 20 cm and inclined at 45°. The cap-beam of all piers presents a U-shape section, with ɸ 18 longitudinal steel bars andɸ 8 mm transverse reinforcement, as shown in (Fig. 3.11). The details of the reinforcement of each portal frame each pier can be found in (Paolacci & Mohamad, 2010).

Figure 3.11 Reinforcement details of the transverse beam

3.5. Soil conditions

Figure 3.12 shows the geological map of the zone where the Rio-Torto viaduct is placed. From the analysis of the map emerges that the viaduct was built on an extensive zone of argillite calcareous (light green zone) and on lens of sandstones (white-red zones).

Figure 3.12 Geological conditions of the zone

This justifies the presence of a shallow foundation (plinths) in all the piers as the (Fig 3.13) shows.

Figure 3.13 Shallow foundation (Plinths) of the Rio-Torto viaduct

3.6. Seismogenic zone and response spectra

The viaduct was constructed on a zone with moderate-to-high seismic activity. The seismogenic zone (913, according to the Italian catalogue) where the bridge is placed is indicated in (Fig. 3.14a).

The associated shaking map (from INGV) shows (Fig. 3.14b) that the expected PGA ranges between 0.23g and 0.25g for the life safety condition (probability of 10% in 50 years), whereas for the collapse prevention condition (probability of 2% in 50 years) PGA ranges between 0.30g and 0.35g.
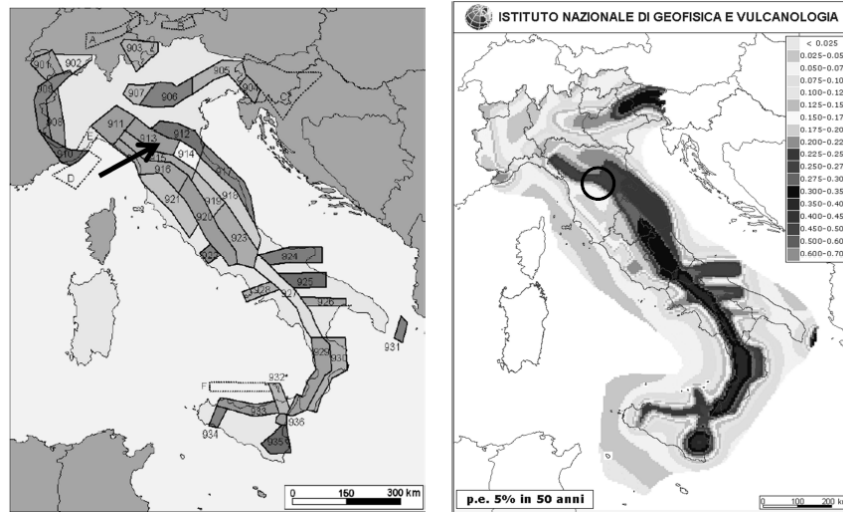
Figure 3.14 (a) Seismogenic zones, (b) Italian ground shaking intensity map on Bedrock (INGV)

For the current Italian seismic code, assuming rigid soil conditions (soil A), nominal life=100 years and class of construction = IV, the maximum PGA for the following limit states is: PGA = 0.147g for immediate occupancy, PGA=0.308g for life safety and PGA=0.334g for collapse prevention. This is consistent with the indications of the INGV shaking map. The response spectra for the different limit state conditions are illustrated in (Fig.3.15).
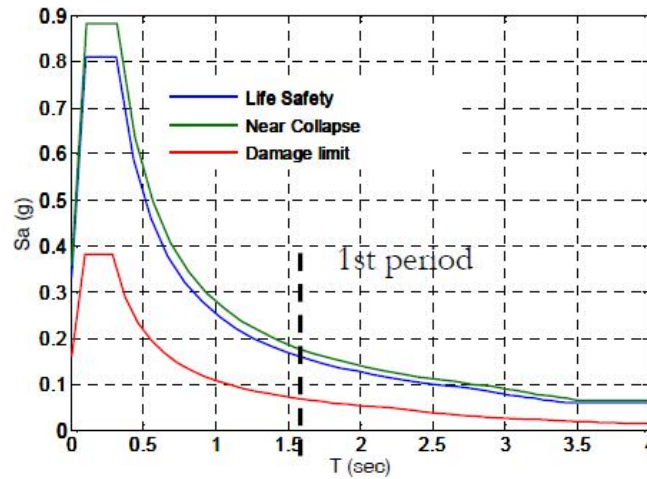
Figure 3.15 Response spectra of the viaduct according to the current Italian code (Soil A)

The most recent database on the historical seismic activity of zone 319 evidences earthquakes with magnitude ranging from 6.13 to 6.6; no active faults have been identified.

According to the research program of RETRO project and to individuate the most credible seismic scenario the Bogazici Unit has performed a Hazard analysis to provide the most probable shaking map in terms of PGA, PGV and Sa(T) of the seismic zone of the Rio-Torto viaduct. At the end the software ELER has been used taking into account all the local conditions in terms of soil, faults, etc..

In order to obtain preliminary results on the seismic hazard at the site the results obtained using the MathHazard software are presented (Giannini, 2000). The program is based on the Gutemberg-Richter law to estimate the probability of occurrence of the earthquake and on the Sabetta-Pugliese attenuation law to provide the probability of occurrence for a given exposition time. The results are summarized in (Fig.3.16), where the seismogenic zones used in the simulation and the corresponding hazard function for an exposition time of 50 years are shown.
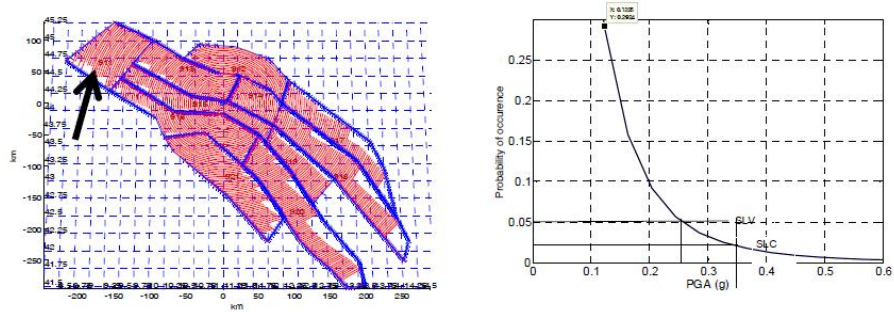
Figure 3.16 (a) Seismogenic zone of the viaduct (b) seismic hazard in terms of PGA for 50 years

The results are in agreement with the hazard result provided by the Italian regulation and the INGV. In particular, PGAs of 0.25g (Life safety limit state - SLV) and 0.33g (Collapse limit state - SLC) are obtained for probabilities of occurrence of 5% and 2% over a 50 year period, respectively.

4. NUMERICAL MODELLING OF RIO-TORTO BRIDGE

The numerical modelling is playing a significant role in the assessment of any existing structure. To study the seismic behaviour, it is important to build a reliable F.E nonlinear model for the Rio-Torto bridge taking into account the global and local behaviour of the bridge.

Two software have been used for the numerical simulation. The first one is Midas Gen; an integrated software for analysis and design system for buildings and general structures. The preliminary model implemented in Midas for As-built configuration only. The only flexural model has been studied with neglecting the local behaviour effects.

In the second software OpenSEES, The model has been implemented for the both cases As-built and Isolated configurations. In this refined models the main non-linear phenomena (flexural behaviour of columns and beams, strain penetration, shear deformation, P-Delta effect, etc.) are included.

This chapter discusses the numerical procedures used for both software by focusing on the restraints and boundary condition assumptions, the materials constitutive laws.

4.1. Preliminary Model using Midas Gen

As a preliminary investigation for the behaviour of Rio-Torto bridge, the numerical model has been developed using MIDAS Gen software. The details on the constitutive laws of the materials are provided together with the model assumptions like finite element types, restraint and boundary

conditions, modelling and position of the masses, etc…In this model, the flexural behaviouris taken into account only. P-Delta effect is also included.

The model has been created for one line of the bridge using Midas Gen software. It has many advantages which make it easy and fast in non-linear analysis implementation, permitting the definition of the sections with grateful possibility of rapid changing. The model used here is in full scale (Fig. 4.1).
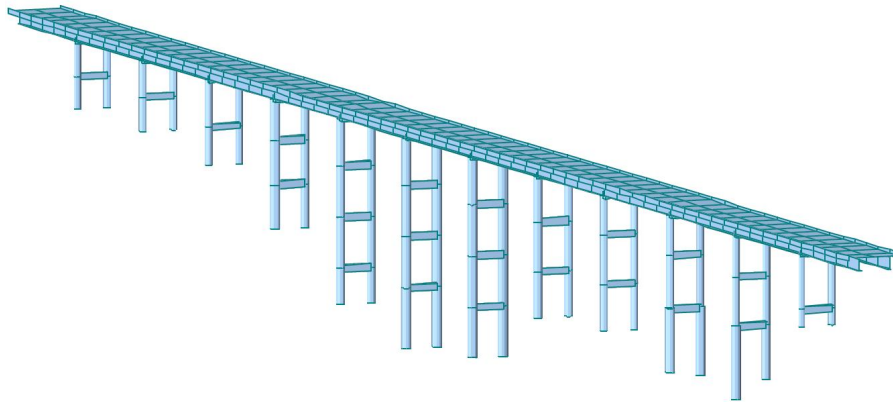
Figure 4.1 Longitudinal 3-D view of the RIO-TORTO viaduct – MIDAS

The model is composed by fiber beam elements reproducing the real disposition of the reinforcing bars into the sections of beam and columns of the piers. An example of fiber section subdivision for a column and a transverse beam is illustrated in (Fig. 4.2 and 4.3).
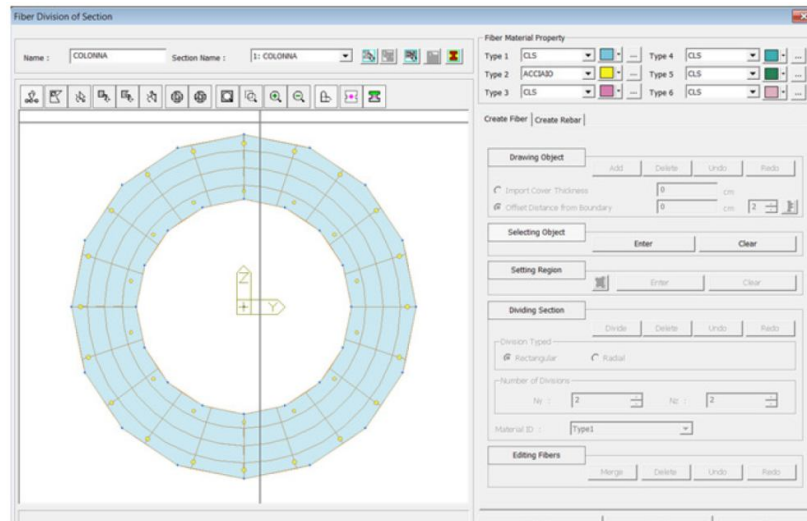
Figure 4.2 MIDAS - Fiber subdivision of a column of pier #9
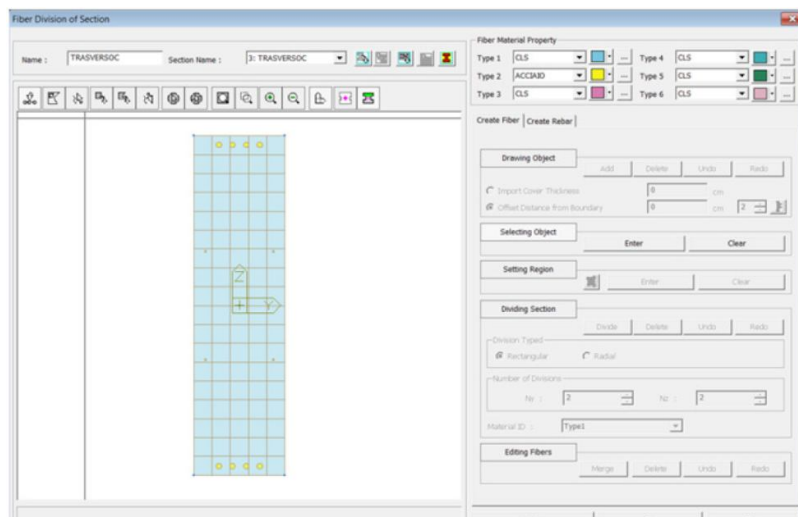
Figure 4.3 MIDAS - Fiber subdivision of one of the transverse beams of pier #9

In order to assign the masses along the deck, each span of the bridge was divided into 5 parts (with length ranging from 5.81 to 6.60 m). Then the translational mass has been defined on these pieces along the longitudinal,

transverse and vertical direction while the rotational mass (m_x, m_y and m_z) has been defined only around longitudinal direction (global y-axis).
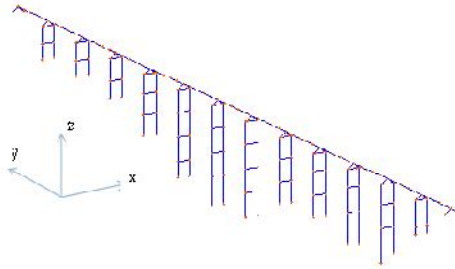
Figure 4.4 Elements and nodes of the MIDAS model
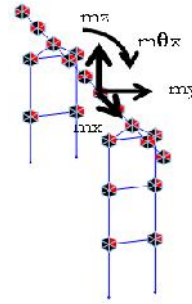
Figure 4.5 Masses placement in the MIDAS model

The translational and rotational masses of each node are indicated in the following Table 4.1:

Table 4.1 Masses of the bridge

Bay length (m)	$m_x=m_y=m_z$ (kN/g)	$m_{\theta x}$ (kN/g m^2)
6.60	115	1154
5.81	101	1016

For piers, the mass has been calculated also and assigned in the joints for the longitudinal and transversal directions as shown in (Fig 4.6).
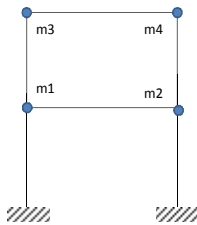
Figure 4.6 Masses symbols of the piers

The following Table 4.2 shows all the quantities of the mass assigned on all the piers:

Table 4.2 Mass at each node in all piers

Pier number	m1 [kN/g]	m2 [kN/g]	m3 [kN/g]	m4 [kN/g]	m5 [kN/g]	m6 [kN/g]	m7 [kN/g]	m8 [kN/g]
1	27.52	27.52	22.27	22.27	-	-	-	-
2	57.5	48.36	29.7	29.7	19	19	-	-
3	53.8	56	30	30	18.1	18.1	-	-
4	31	31	28.95	28.95	17.74	17.74	-	-
5	32.9	32.9	33.53	33.53	20.7	20.7	-	-
6	34.86	34.86	35.78	35.78	34.76	34.76	21.3	21.3
7	37.92	37.92	35.77	35.77	34.76	34.76	21.3	21.3
8	34.96	34.96	35.77	35.77	34.76	34.76	21.3	21.3
9	31.49	31.49	30.78	30.78	19.47	19.47	-	-
10	27.72	27.72	20.08	20.08	-	-	-	-
11	23.75	23.75	17.22	17.22	-	-	-	-
12	22.83	22.83	16.82	16.82	-	-	-	-

4.1.1. Non-linear constitutive laws for materials

The section of each element is subdivided into fibers so that it is possible to assign for each material the constitutive law and the exact position and dimension of the reinforcing bars. The constitutive law of each material is described and the parameters adopted are provided.

4.1.1.1. Constitutive laws for Concrete

The Mander model is adopted for the behaviour of concrete. For monotonic loading, the compressive concrete stress f_c is given by the Popovics curve expressed as:

$$f_c = \frac{f'_{cc} \times r}{r\text{-}1+x^2} \tag{4.1}$$

Where the parameters of this equation are defined by following equations:

$$f'_{cc} = k \times f'_{co} \tag{4.2}$$
$$x = \varepsilon_c/\varepsilon_{cc} \tag{4.3}$$

$$\varepsilon_{cc} = E_{co} \times \left[1 + 5\left(\frac{f_{cc}'}{f_{co}'} - 1 \right) \right] \tag{4.4}$$

$$r = \frac{E_c}{E_c - E_{sec}} \tag{4.5}$$

$$E_c = 5000 \sqrt{f_{co}'} \tag{4.6}$$

$$E_{sec} = \frac{f_{cc}'}{\varepsilon_{cc}} \tag{4.7}$$

where k is the confinement factor, f_{co}' is the compressive strength of unconfined concrete, f_{cc}' is the compressive strength (peak stress) of confined concrete, ε_c is the longitudinal concrete strain, ε_{co} is the strain at unconfined stress f_{co}, ε_{cc} is the strain at maximum concrete stress f_{cc}', E_c, is the initial modulus of elasticity of concrete and E_{sec} is the secant modulus of elasticity of concrete at peak stress as shown in (Fig. 4.7).

In the simulations, especially using Opensees, the Kent-Scott-Park model is also adopted. This constitutive law has a first parabolic branch up to compression peak stress equal to 30 MPa with a corresponding strain equal to 0.25 % and a decreasing linear branch to 26 MPa with corresponding strain of 0.6%. The Opensees result will be object of next section.

According to the results reported in literature, especially from experimental tests, the contribution of concrete in modelling structures with plain steel bars and poor seismic details, the tensile strength of the concrete has been neglected (Marfet et al. 2009). Nevertheless, in the simulation that use Mander model, it has been accounted for, according to the formula:

$$f_t' = 0.62 \sqrt{f_{co}'} \quad \text{MPa} \tag{4.8}$$

Whereas when the Kent-Park model is used it is neglected.

4.1.1.2. Constitutive laws for Steel bars

The reinforcing steel bars are modeled according to the Menegotto-Pinto constitutive law. A yield stress equal to 360 MPa is assumed here, along with a modulus of elasticity equal to 205000 MPa and a hardening parameter equal to 0.025 as shown in (Fig 4.8). The transition parameters from elastic to plastic behaviour are chosen according to (Menegotto & Pinto, 1973).
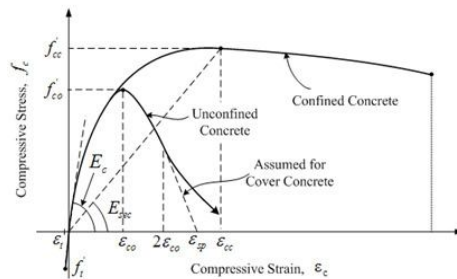
Figure 4.7 Concrete constitutive law: Mander Model
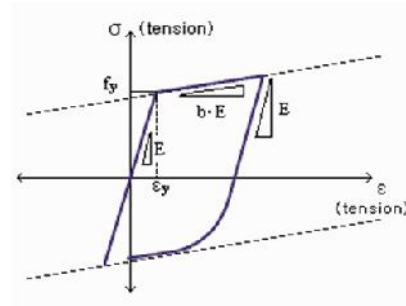
Figure 4.8 Steel constitutive law: Menegotto-Pinto model

In Table 4.3, the parameters are reported of both the constitutive laws for steel and concrete adopted to model the Rio-Torto viaduct.

Table 4.3 Parameters used in concrete and steel constitutive laws

Concrete	E_c [MPa]	ε_{c0}	ε_{cc}	f_{co} [MPa]	f_{cc} [MPa]
	27000	0.002	0.0025	27	30
Steel	E_s [MPa]	fy [MPa]	b		
	205000	350	0.03		

4.1.2 Restraints and boundary conditions

The supports of the piers has been considered as fully fixed in all directions while for abutments of the both sides of the bridge have been assumed to be simple rested in the longitudinal direction (global y) but restrained in the direction of x and z (Fig. 4.9 - 4.11).

Regarding to the Gerber saddles, the saddles has been modeled as hinges, thus with the possibility of transfer shear in longitudinal and transversal direction. The reasons of this choice are several:

a) It is difficult to believe that in the transversal direction free movement of the saddles can be considered, at least under an equilibrium point of view of the piece between two saddles.
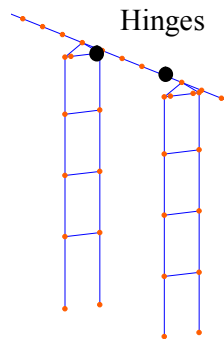
| Figure 4.9 Hinge model for the Gerber saddles | Figure 4.10 Restraint conditions between deck and abutment | Figure 4.11 Restraint conditions between deck and abutment |
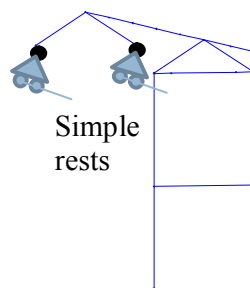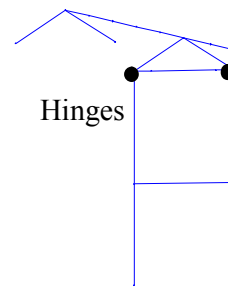
b) The viaduct has a slight curvature (as in the picture below); this can induce the transmission of shear forces in the transversal direction due to the rotation in vertical direction of the adjacent parts of the deck that can induce pounding.

c) The presence of saddles in longitudinal direction would suggest the use of a gap element. This means that the four parts, in which the viaduct can be divided, would behave independently from each other. Thus the hypothesis of considering hinges is certainly more conservative.

As for connecting the deck to the piers, two rigid beams have been created from the center of mass of the deck to the top of the piers. The stiffness of the beams is assumed to be infinite because it is reasonable to consider it undeformable (Fig. 4.12).
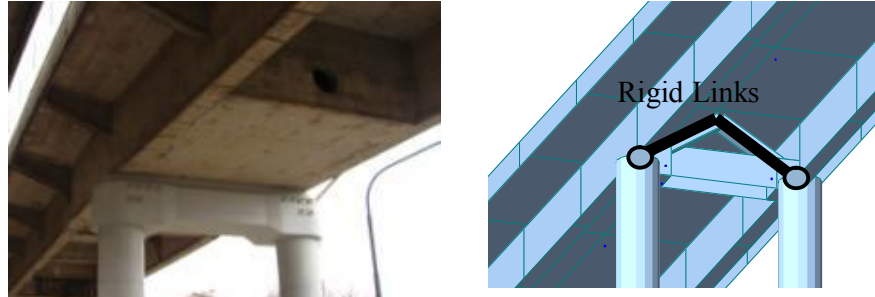
Figure 4.12 Rigid beams to connect the deck to the piers

4.2. Refined model simulation of the bridge using OpenSees for As-built and Isolated cases

4.2.1. Opensees F.E model of the As-built configuration

This section is showing the description of the refined numerical model developed in OpenSees. In this model the main non-linear phenomena (flexural behaviour of columns and beams, strain penetration, shear deformation, P-Delta effect, etc.) are included.

4.2.1.1 Description of the main non-linear phenomena of the Rio Torto viaduct

As described in Chapter 2, a previous investigation campaign as a part of ReLuis project aiming at studying the cyclic behaviour of the piers was carried out both numerically and experimentally. A test campaign, performed at the structural laboratory of University Roma Tre, consists of quasi-static cyclic displacements imposed to three 1:4 scale specimens of pier 12. Details on the experimental results can be found in (Paolacci & Giannini, 2012). The results confirmed that the response of the pier is highly affected by the behaviour of local details, such as non-linear shear deformability of the transverse beam or strain-penetration of the plain steel bars. In (Fig. 4.13a) the numerical and experimental cyclic force-deflection responses of pier 12 are shown, whereas in (Fig. 4.13b) the experimental shear crack pattern of the transverse beam is shown.
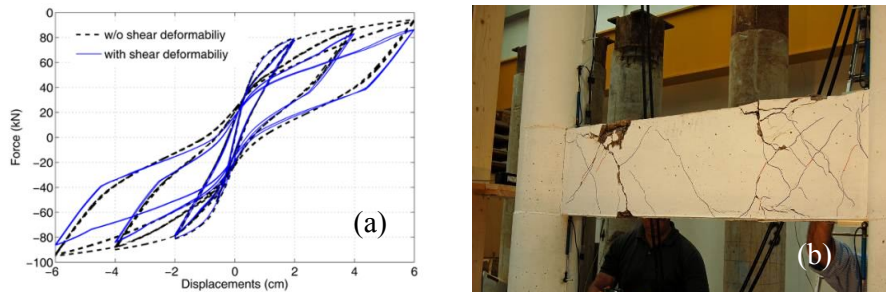
Figure 4.13 Experimental investigation at University Roma Tre: (a) Force-deflection cycle of pier 12, (b) Shear Damage in the transverse beam of pier 12

4.2.1.2 Geometry and constitutive laws

The model was created for one lane of the bridge with full scale dimensions using OpenSees framework software. (Fig. 4.14).
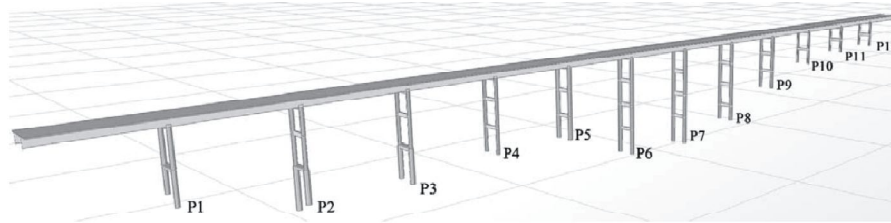
Figure 4.14 Rio-Torto viaduct - Opensees

The model is composed by fibre beam elements reproducing the location of the reinforcing bars into the sections of beam and columns of the piers. For example, the finite element scheme of pier 12 is illustrated in (Fig. 4.15)
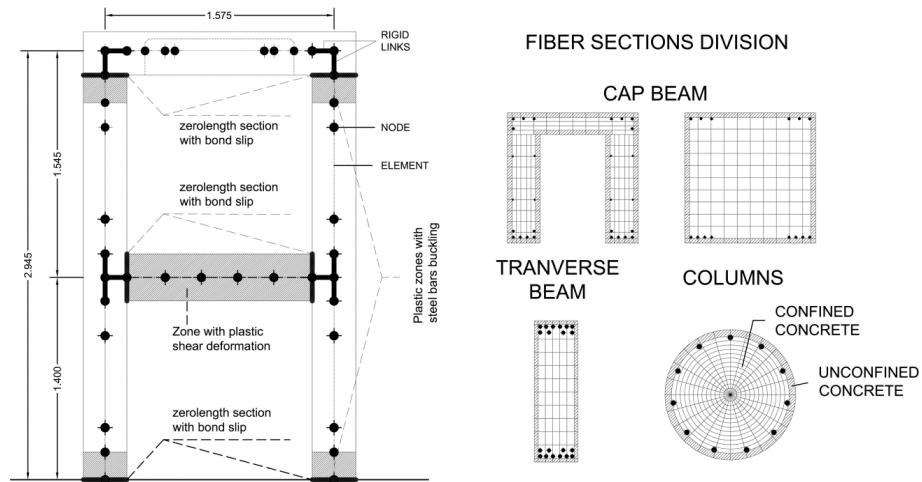
Figure 4.15 Numerical model of pier 12

The structural elements are modelled by nonlinear beam elements with flexibility formulation. All degrees of freedom are fixed at the base of the finite element model.

The section of each element is subdivided into fibres so that it is possible to assign for each material the constitutive law and the exact location and dimension of the reinforcing bars. The cross sections are also indicated in (Fig.4.15). The Kent-Scott-Park model is adopted for the stress-strain behaviour of concrete. This constitutive law has a first parabolic branch up to the peak compression stress equal to 26 MPa at a corresponding strain equal to 0.25%, and a decreasing linear branch to 22 MPa at a corresponding strain of 0.6%. According to the results reported in the literature, especially from experimental tests, the contribution of concrete tensile strength in modelling structures with plain steel bars and poor seismic details can be neglected (Marfet et al. 2009).

The same Menegotto-Pinto constitutive law previously discussed has been used for the Opensees model. The yield stress equal to 360 MPa is assumed here, along with a modulus of elasticity equal to 205,000 MPa and a hardening parameter equal to 0.025, as shown in the previous section.

The same configuration of restraints and boundary conditions used in Midas model has been adopted in the OpenSees model. This includes dividing of the bridge deck and assigning of the mass along the deck and piers to simulate translational masses.

4.2.1.3. Strain penetration effect of the plain steel bars

An important aspect to consider is the bond-slip effect in proximity to the bottom and top of the columns. This phenomenon is due to the difference between the deformation of the bars and concrete which yields a typical crack pattern (Fig. 4.16). In literature, the bond-slip problem and its contribution to the lateral flexibility of structures for horizontal forces has been widely investigated. It is worth pointing out that this effect may be pronounced for plain bars due to the low bond between concrete and steel. Following the approach proposed by (Zhao & Sritharan 2007), one way to

account for the bond-slip effect consists of concentrating the rotation due to the slippage of the bars in a section.

Figure 4.16 Crack opening for bar slippage
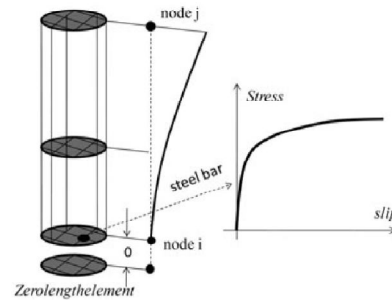
Figure 4.17 Zhao and Shritaran model

This may be done in OpenSEES by using a fibrezeroLengthSection element, for which a unit length is assumed. This implies that element deformations correspond to section deformations and then the moment-curvature is equivalent to the moment-rotation relationship. In this way, the rotation due to bond slip effect may be accounted for by defining a proper stress-slip relationship for steel, describing the interaction between concrete and the steel bar (Fig. 4.17). It was used to model the sections at the top and bottom of the columns and the end sections of the transverse beam. The bond-slip parameters are chosen according to experimental results of pull-out tests as previously described. In particular the value of slip sy, corresponding to the yielding of the bars, is equal to 0.5 mm, whereas the ultimate slip su was assumed equal to 40×sy.

Depending on the anchorage detail and the corresponding slippage mechanism, it is possible for steel bars with sufficient anchorage length to exhibit pinching in the hysteretic behaviour. For this reason the cyclic behaviour associated with the strain-penetration effect modelled by Zhao and Sritharan contains a coefficient Rc that permits the pinching characteristic to be accounted for in the analytical simulation of flexural members. The value adopted here for Rc is 0.5.

4.2.1.4. Modelling of non-linear shear behaviour

In order to calibrate the numerical model of the pier, a shear model of the transverse beam must be implemented. It is well known that shear response plays an important role especially for existing structures that do not meet seismic engineering design criteria. In literature, several studies concerning the shear behaviour of reinforced concrete beams or walls and their interaction with flexural response are reported and compared with experimental results (Ceresa & Petrini, 2007, Hildago & Jordan, 2002).

Considering these formulations and the relatively scarce information about experimental results for shear behaviour in the presence of plain longitudinal bars, a phenomenological shear-strain hysteretic relationship for shear behaviour of the transverse beam was assumed. It consists of a tri-linear envelope curve with stiffness and strength degradation with pinching response which is always observable in reinforced concrete elements subjected to shear forces. The model is similar to the one proposed in (D'Ambrisi & Filippou, 2009, Lee et al. 2005), except for both the influence of axial force on the shear relationship, here neglected, and the use of a tri-linear backbone curve.

The force-deformation relationship for shear is implemented by using the OpenSEES command "Section Aggregator", which groups the behaviour of different materials into a single section force-deformation model; in this way, the shear and flexural behaviour are linked by means of equilibrium equations, even though their mechanical formulations are uncoupled.

In this case, a uniaxial material is chosen to represent the sectional shear behaviour. It is defined through three points of the envelope curve (Fig. 4.18).
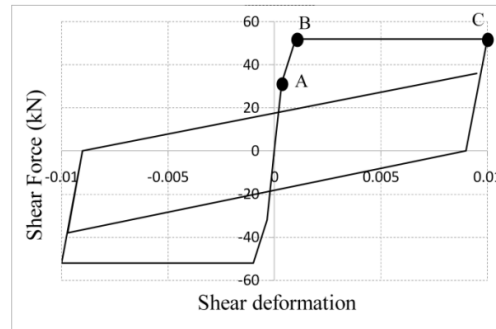
Figure 4.18 Shear force-deformation relationships

The first point (A), corresponding to the onset of shear cracking, was evaluated experimentally for pier 12; it is characterized by a shear deformation γ_a equal to 3.5×10^{-4} and a shear strength V_a equal to 200 kN. The second point (B) was partially evaluated using the experimental data of pier 12. In particular, the force V_b equal to 900 kN was obtained with the formula proposed by (Priestly et al 1996), and confirmed using the software Response 2000 (Bentz et al. 2000), based on the Modified Compression Field theory (Vecchio & Collins, 1998). The shear deformation γ_b equal to 1.0×10^{-3} was indeed obtained from the experimental data of pier 12, as already explained. The third point (C) has ordinate $V_c=V_b$ and shear deformation equal to $\gamma_c=10\cdot\gamma_b$, which implies that the overall shear force remains constant for the last cycles. For comparison, the shear strength V_b was also evaluated using the formula of Eurocode 8 part 3, regarding the assessment and retrofitting of existing buildings, which depends on several parameters, among them the level of flexural ductility μ. Because the experimental results have shown for all the piers a very limited flexural damage, a ductility $\mu=1$ was considered reasonable. The corresponding strength V_b is about 900 kN.

In order to account for the hysteresis phenomenon in the shear force-deformation relationship, a hysteresis law was used, characterized by several parameters which modify pinching and stiffness, namely the damage level as function of the ductility level, the damage related to the

dissipated energy and the unloading stiffness as function of ductility (Balan & Filippou, 1998).

4.2.2. OpenSees F.E. model of Isolated configuration and Implementation of the isolators

4.2.2.1. Design of the FP isolation system

The isolation system adopted in this test includes the Friction Pendulum (FP) system (e.g. Zayas et al. 1990, Mokha et al. 1991, among many others). The design of the FP devices was carried out with a displacement-based procedure focusing on two objectives:

(a) Keep the piers in the (quasi-) elastic range of response.
(b) Minimize the displacement demand on the expansion joints located at the abutments.

In general, there are three basic types of FP devices used for new and existing constructions:

(i)   Isolators with one spherical sliding surface that may be at the top or at the bottom of the device, connected to a spherical hinge.
(ii) Isolators with two main spherical surfaces and an interposed point rocker articulation that allows relative rotations (Fenz & Constantinou, 2006).
(iii) Devices with two perpendicular cylindrical surfaces and two perpendicular cylindrical articulations allowing two relative rotations (Marin et al. 2006).

The selection of the FP device to be used in a specific project depends on the structure to be retrofitted. The type of FP depends on the allowable displacement of the structural system. Such displacements generally control the design of the isolators. The second type is often used to

minimize the plan dimensions of the isolator and to limit the vertical load eccentricity caused by the horizontal displacement. The third type is used when a different behaviour is required in two perpendicular directions. The first type is the most commonly adopted due to its simplicity and was adopted to seismically isolate the Rio-Torto bridge, which is characterized by relatively low displacements and similar response along the lateral and transverse directions. The basic elements of a single-surface FP, as shown in Fig. 4.1, are: the upper anchor plate (1), the sliding surface (2), the sliding material interface (3), the rotation element (4), the rotation sliding surface (5) and the lower anchor plate (6) (De Risi, & Di Sarno, 2011).

From a mechanical standpoint, the FP devices are characterized by a bilinear force displacement relationship:

$$V_{FPS} = \mu_f . N + \frac{N}{R} . \Delta_{iso} \tag{4.9}$$

Where μ_f is the friction coefficient, N is the normal force, R is the device curvature radius and Δ_{iso} is the sliding displacement in the isolator. Figure 4.19 provides a typical hysteretic behaviour obtained during dynamic tests on a FP with a single sliding surface.
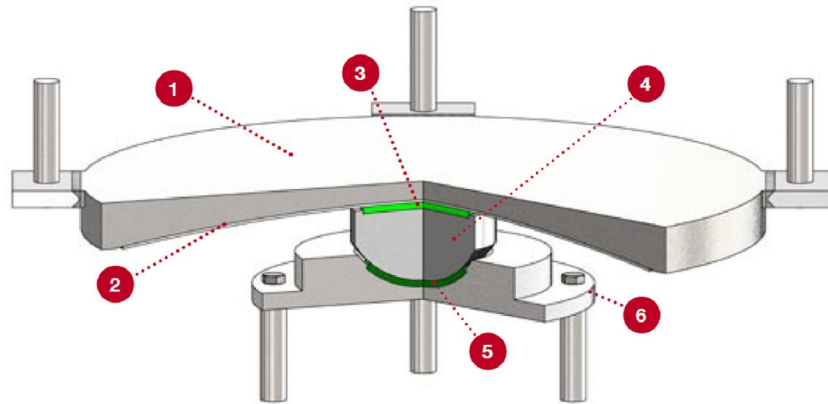
Figure 4.19 Single sliding surface friction pendulum system (courtesy of ALGAS.p.A)
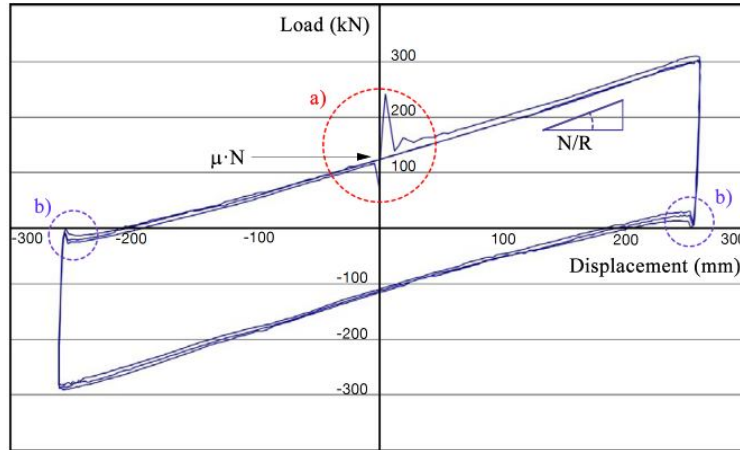
Figure 4.20 Hysteretic behaviour obtained during dynamic tests on single concave surface sliding pendulum

The variation of the friction coefficient relative to the breakaway of the motion (a) and change in sign of velocity (b) is also displayed in (Fig. 4.20). The FP isolation system was designed according to a displacement-based design method that is presented in detail in (Della Corte & De Risi, 2013). The method is based on the direct displacement based procedure proposed by (Priestley et al. 2007). A few modifications have been proposed to the general method and specific design tools were developed for the case of isolation by means of FPS. It is worth mentioning that the adopted methodology for the specific case study is focused on the design of FP systems, but it can be easily extended to other systems exhibiting a bilinear hysteretic behaviour. The FPS used for the seismic retrofitting of the Rio Torto had a radius of 3 m, a friction coefficient of 4%, an articulated slider of 9 cm height and an initial yield displacement of 0.5 mm. Nonlinear response history analyses for the base isolated model of the Rio Torto bridge were carried out by using the 20 and 29 May Emilia (Italy) earthquakes.

4.2.2.2. OpenSees F.E. model of Isolated configuration

The 3D model was developed to simulate accurately the seismic response of the Rio-Torto bridge. The numerical model is similar to the FE system

used for the non-isolated case: joints and elements labelling, modelling of the piers (considering all the nonlinear sources, i.e shear behaviour and fix-end rotation), deck represented as elastic beam, piers fixed to the base and end supports assumptions. Two differences were, however, included for the base isolated system: the Gerber-saddle was removed (i.e. a continuous beam was obtained) and isolation devices between the piers and the deck were introduced to represent the seismic retrofitting scheme. The use of base isolators for the bridge deck increased the number of vertical coordinates of the deck joints.

The FP devices used to seismically isolate the bridge deck of the Rio Torto were modelled in the computer program Opensees. The command used to simulate numerically the response of the FP is a "singleFPBearing" element object (Schellenberg, 2010), which defined by two nodes. The i-Node represents the concave sliding surface and the j-Node represents the articulated slider. The element can have zero length or the appropriate bearing height. The bearing has unidirectional (2D) or coupled (3D) friction properties (with post-yield stiffening due to the concave sliding surface) for the shear deformations, and force-deformation behaviours defined by UniaxialMaterials in the remaining two (2D) or four (3D) directions. To capture the uplift behaviour of the bearing, the user-specified UniaxialMaterial in the axial direction was modified for no-tension behaviour. By default P-Delta moments are entirely transferred to the concave sliding surface (i-Node). It is important to note that rotations of the concave sliding surface (rotations at the i-Node) affect the shear behaviour of the bearing. To avoid the introduction of artificial viscous damping in the isolation system (sometimes referred to as "damping leakage in the isolation system"), the bearing element does not contribute to the Rayleigh damping. If the element has non-zero length, as in this case, the local x-axis is determined from the nodal geometry unless the optional x-axis vector is specified in which case the nodal geometry is ignored and the user-defined orientation is utilized.

The mechanical properties used to define singleFPBearings in Opensees are the type of friction material, the curvature radius and the height of the device. The Coulomb approach was used for the simulation of the devices for the Rio Torto bridge; thus kinetic friction is independent of the sliding velocity, in compliance with Coulomb's law. The latter assumption is compliant with the PSD test procedure.

5. SEISMIC RESPONSE ANALYSIS OF RIO-TORTO BRIDGE

This chapter is presenting the preliminary investigation about the seismic behaviour of the bridge. The seismic response analysis of the non-linear model discussed previously in chapter 4 for flexural behaviour using Midas Gen Software analysis has been presented. However, the preliminary numerical simulation was necessary because it gave more clear view for the plan strategy for the experimental campaign design of pier frame specimens. The main non-linear analysis simulating the entire bridge at this stage is modal analysis and response spectrum analysis. Further, a focus analysis on piers under investigation "Pier 9 and 11" has been given; specifically, static cyclic and dynamic analysis to give more confident response behaviour.

Then, this chapter discussed also the seismic response of the refined non-linear numerical model using OpenSEES software framework. Attention paid on the detailed "as-built" and "isolated" configurations, including identifying the level of damage expected by defining the signal data input for both Serviceability and Ultimate Limit States.

5.1. Preliminary evaluation of the seismic response of As-built configuration

The preliminary results based on the numerical model developed in MIDAS are described. Firstly, a preliminary analysis of the non-linear behaviour of the pier 9 and 11are illustrated and discussed. The cyclic

behaviour is analyzed for pier 9 and 11 in 2-D built using MIDAS in order to acquire information on stiffness and yielding strength and over strength of the single pier. A preliminary dynamic analysis of both the piers has been conducted aiming at evaluate the influence of the rotational mass of the deck and the distributed mass of the pier on the dynamic behaviour of the bridge.

Subsequently preliminary results on the full 3D model of the entire viaduct are presented. In particular a free vibration analysis of the viaduct has been performed in order to individuate the most important vibration modes and the influence of the several hypotheses included in the model on the dynamic behaviour of the bridge. Moreover a preliminary analysis of the seismic behaviour of the entire bridge in the non-linear field has been conducted whose results are used to understand the level of post elastic behaviour of each pier.

5.1.1. Static cyclic analysis in 2-D of pier 9 and 11

Using MIDAS software the cyclic behaviour of pier #9 and #11 is here illustrated. The model is fully non-linear in bending, whereas any local behaviour (strain-penetration, buckling, shear, etc..) is for now excluded.

To acquire information on their cyclic behaviour a quasi-static horizontal displacement has been applied at the top of each pier, whose time-history is illustrated in (Fig. 5.1 and 5.2). The application of the horizontal displacement is preceded by a step-by-step application of the gravitational loads using a linear law.
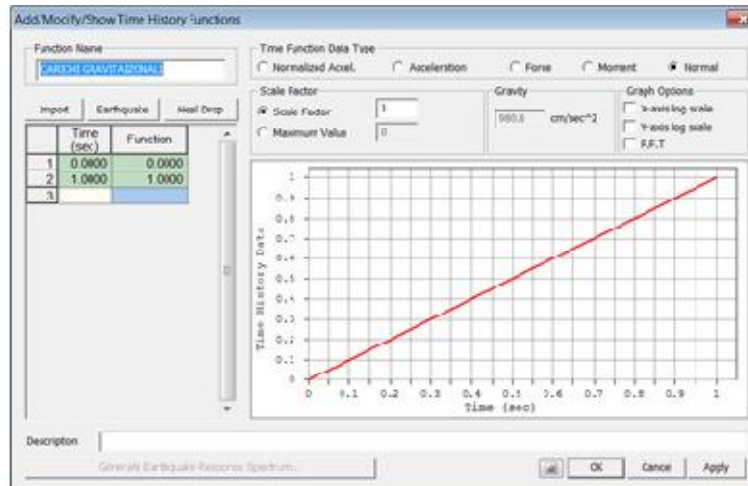
Figure 5.1 T-H of the gravitational load
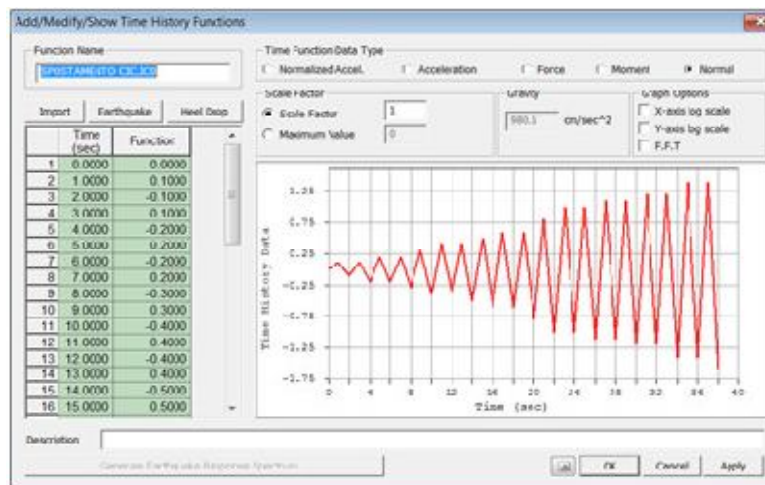
Figure 5.2 T-H of the horizontal displacements

In (Fig 5.3 and 5.3) the global cyclic response of pier 9 and 11 are shown in terms of force deflection relationship.
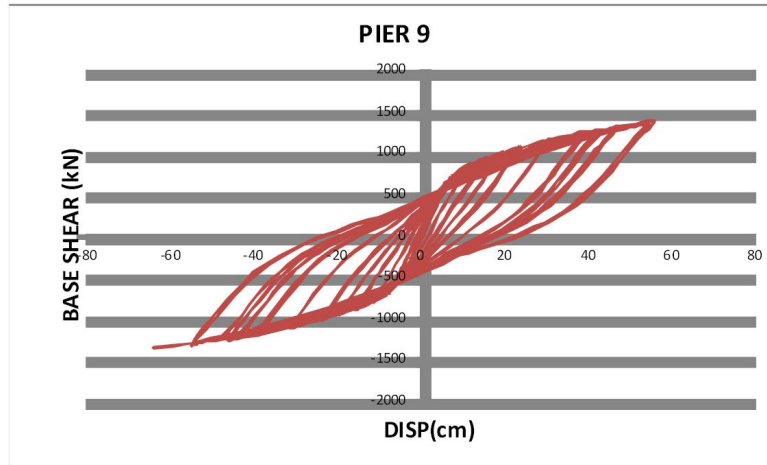
Figure 5.3 Force-deflection cycle: pier 9
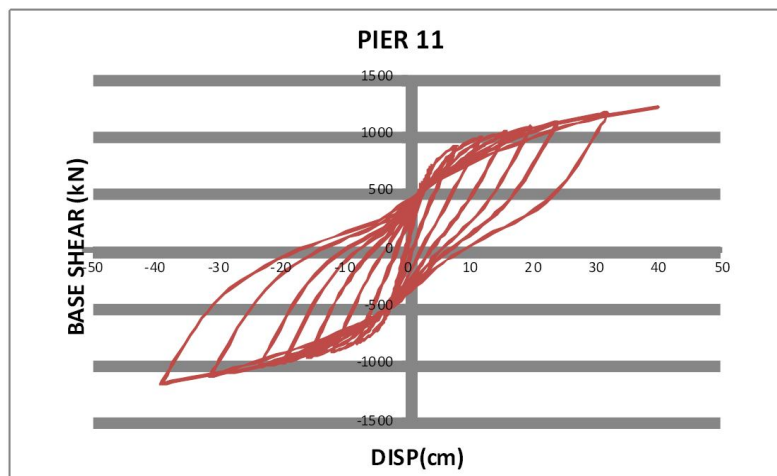
Figure 5.4 Force-deflection cycle: pier11

Because the maximum expected displacement under seismic action for both the piers is on the order of 20-25 cm, the results show that the piers can be subjected to high plastic deformations. This is also shown by the local behaviour of the elements. For example in (Fig 5.5 - 5.8) the Moment curvature relationship of the section at the base of one of the columns is shown, together with the Moment-curvature of one of the transverse beams.

The maximum base shear corresponding to 25 cm is about 1000 kN either for the pier 9 and pier 11. This means that using a scale factor 1:2 the maximum base shear would be around 250 KN.

The sequence of the plastic hinges formation for the pier #9 is illustrated in (Fig 5.9) that shows a scenario of high plastic deformations to which the piers would be subjected during the PsD test. Yellow indicated that the hinges are plasticized.
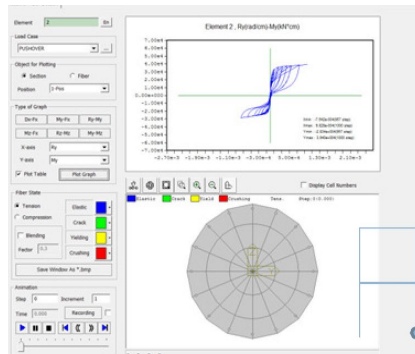
Figure 5.5 Moment-curvature relationship of the base section of column dx – pier 9 (scale 1:2)
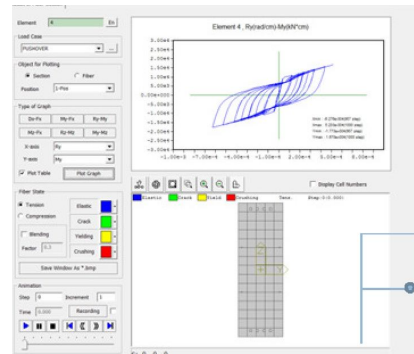
Figure 5.6 Moment-curvature relationship of the transverse beam – pier 9 (scale 1:2)
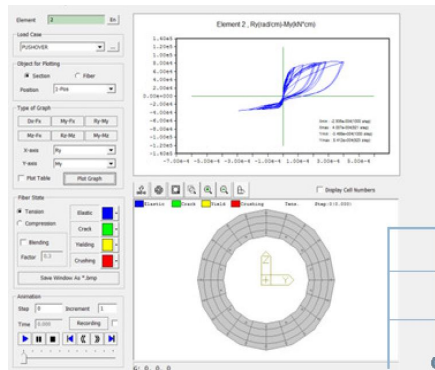
Figure 5.7 Moment-curvature relationship of the base section of column dx – pier 11 (scale 1:2)
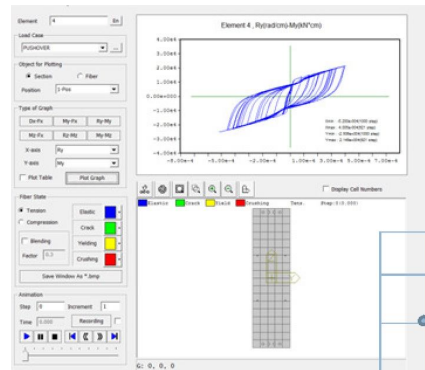
Figure 5.8 Moment-curvature relationship of the transverse beam– pier 11 (scale 1:2)
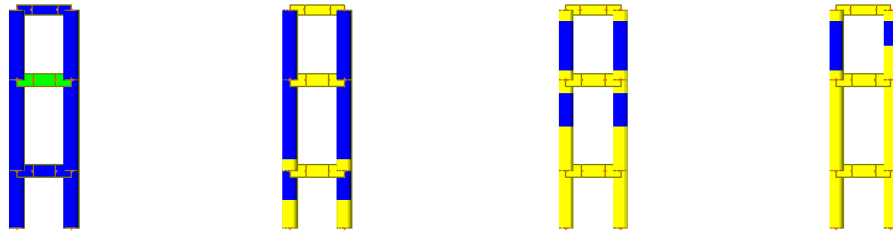
Figure 5.9 Sequence of plastic hinge formation in the pier 9 for cyclic imposed displacements

5.1.2. Dynamic analysis in 2-D of pier 9 and 11

In this section the main results of the dynamic analysis of pier 9 and 11 are illustrated. The free vibration analysis is shown for pier 9 and 11 in 2-D to demonstrate the effect of the distributed mass along the height of the piers and the rotational mass of the deck.

The effect of the distributed mass along the height is important only in the very high piers, for this reason the analysis limited here to pier 9. The analysis in performed under the hypothesis that the translational and rotational masses of the pier are their tributary masses, excluding the influence of the other piers. Table 5.1 shows the periods with and without rotational mass.

Table 5.1 Periods and participating mass of pier 9

	With rotational mass of the deck and distributed mass of the pier		Without rotational mass of the deck and distributed mass of the pier	
MODE	**Period [sec]**	**Mass(%)**	**Period [sec]**	**Mass(%)**
1	1.42	86.0	1.43	86.5
2	0.31	11.13	0.32	11.8
3	0.17	2.12	0.175	2.15

From Table 5.1 and (Fig. 5.10 and 5.11), is clearly seen the negligible influence of the rotational mass and the distributed mass along the height of the pier.

This is confirmed by the results of a response spectrum analysis performed using EC8 spectra, adopting a behaviour factor q=1 and a damping ratio 5%.

The results in terms of bending moment clearly show again that the rotational and distributed masses have no influence on the dynamic response of the pier as shown in (Fig. 5.12 and 5.13).
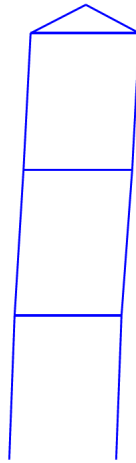
Figure 5.10 1st vibration mode of pier # 9
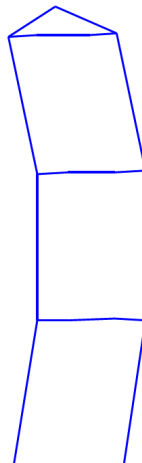
Figure 5.11 2nd vibration mode of pier # 9
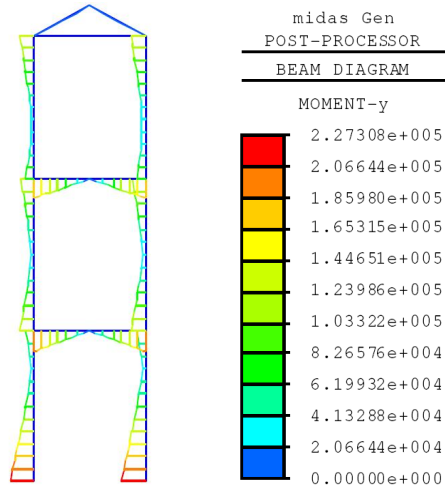
Figure 5.12 Response spectrum analysis - Bending moment pier 9 – with masses
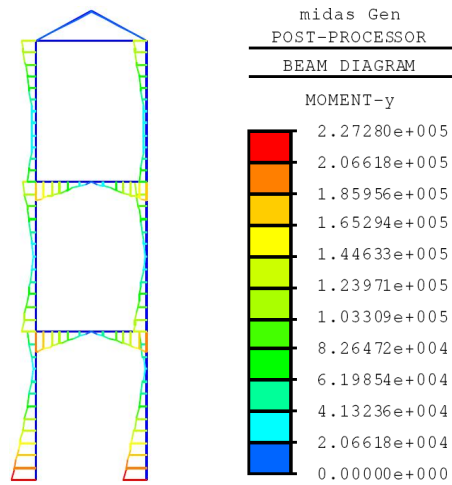
Figure 5.13 Response spectrum analysis - Bending moment pier 9 - without masses

5.1.3. Elastic 3-D analysis of the entire viaduct

In this section the dynamic analysis of the entire viaduct is illustrated. The analysis has been conducted on an elastic 3D model of the bridge using the structural conditions described before (masses, restraint conditions, etc…).

Firstly, the modal analysis of the viaduct is presented and discussed. After that the results of the response spectrum analysis are shown and commented. They have been obtained using the Italian regulation spectra according to the hazard conditions previously identified. In particular soil condition A and B have been used in the analysis.

5.1.3.1. Modal analysis of the Rio-Torto viaduct

The (Figures 5.14 - 5.15) show the main modes of the viaduct. The first mode is in the longitudinal direction with a period of 3.2 sec. The second mode is in the transversal direction which involves pier 9 and 11, as well as the 6th vibration mode with percentage of mass equal to 27.3 and 22.47 respectively. This means that almost 50% of the entire mass participates to the vibration modes that involve pier 9 and 11. This observation suggests that the seismic response of the viaduct from pier 7 to 11 could be analyzed separately from the remaining part of the viaduct.

Table 5.2 Eigenvalues and excited masses of Rio-Torto viaduct

Mode	UX		UY		UZ		RX		RY		RZ	
Mode No	Frequency (rad/sec)		(cycle/sec)		Period (sec)		Tolerance					
1	1,9414		0,309		3,2365		0,00E+00					
2	3,9721		0,6322		1,5818		2,51E-60					
3	4,3224		0,6879		1,4536		1,11E-56					
4	4,4882		0,7143		1,3999		9,10E-55					
5	6,7137		1,0685		0,9359		2,12E-35					
6	6,9384		1,1043		0,9056		6,55E-34					
7	7,7614		1,2353		0,8095		3,35E-29					
8	9,2529		1,4726		0,679		1,44E-17					
Mode No	TRAN-X MASS(%)	SUM(%)	TRAN-Y MASS(%)	SUM(%)	TRAN-Z MASS(%)	SUM(%)	ROTN-X MASS(%)	SUM(%)	ROTN-Y MASS(%)	SUM(%)	ROTN-Z MASS(%)	SUM(%)
1	0	0	92,4172	92,4172	0	0	13,9337	13,9337	0	0	0	0
2	27,3054	27,3054	0	92,4172	0	0	0	13,9337	0,9955	0,9955	1,3052	1,3052
3	2,9052	30,2106	0	92,4172	0	0	0	13,9337	0,2135	1,209	1,2687	2,5739
4	24,8943	55,105	0	92,4172	0	0	0	13,9337	2,2725	3,4816	21,2671	23,841
5	7,1446	62,2496	0	92,4172	0	0	0	13,9337	1,7836	5,2652	19,5858	43,4268
6	22,4731	84,7226	0	92,4172	0	0	0	13,9337	4,5089	9,7741	25,4406	68,8673
7	4,5444	89,267	0	92,4172	0	0	0	13,9337	1,0031	10,7772	13,5839	82,4512
8	0,0058	89,2728	0	92,4172	0	0	0	13,9337	1,3529	12,1302	0,01	82,4612

The significant eigenvalues and the participating masses of the viaduct are presented in Table 5.2, where the corresponding vibration modes are illustrated in (Fig. 5.14 - 5.22)
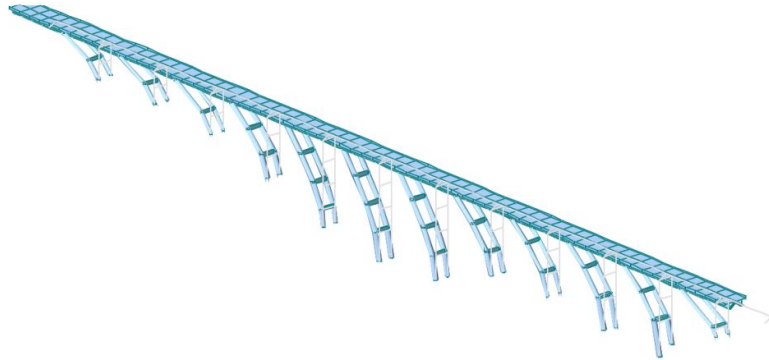
Figure 5.14 Modal analysis – 1st vibration mode of Rio-Torto bridge
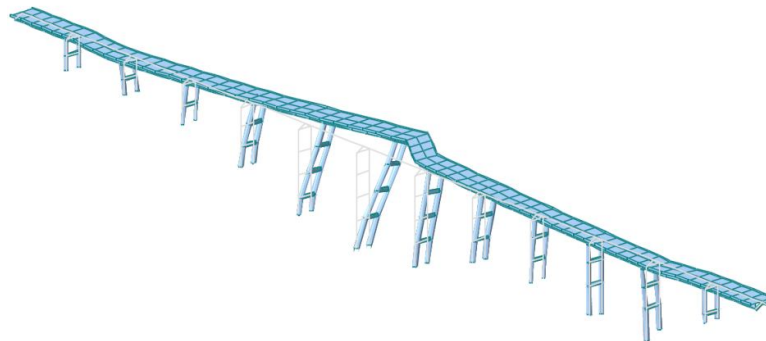
Figure 5.15 Modal analysis – 2nd vibration mode of Rio-Torto bridge
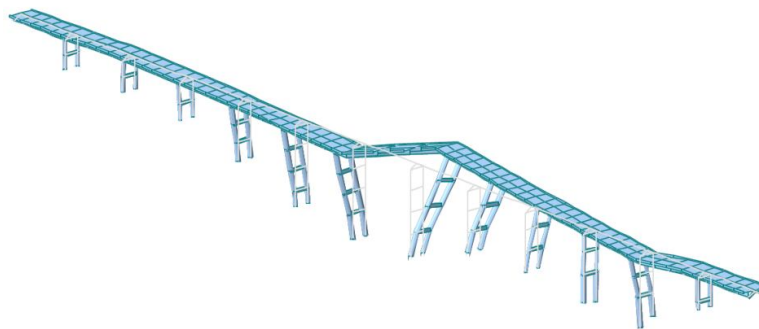
Figure 5.16 Modal analysis – 3rd vibration mode of Rio-Torto bridge
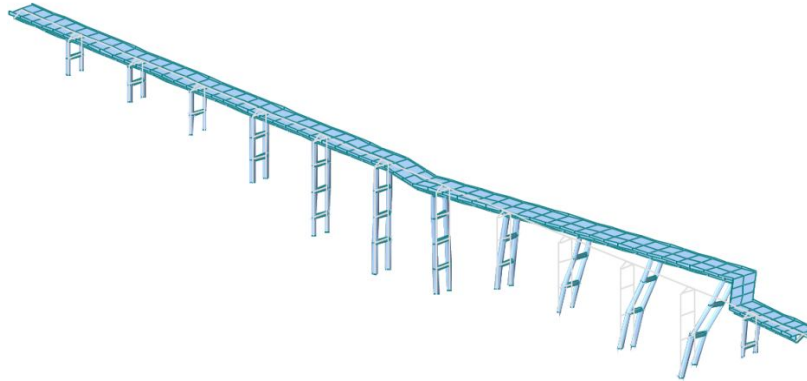
Figure 5.17 Modal analysis – 4th vibration mode of Rio-Torto bridge
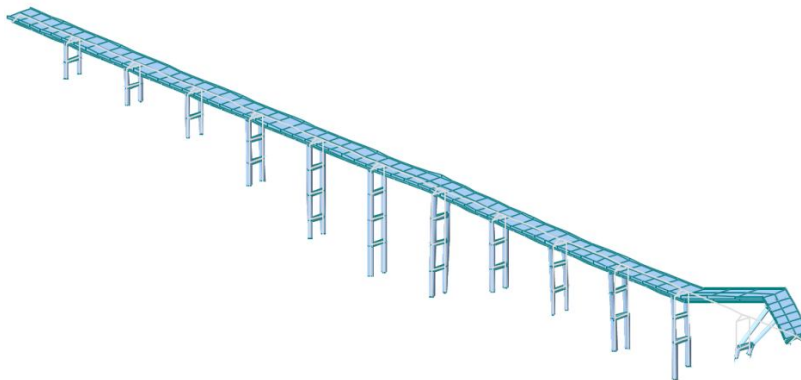
Figure 5.18 Modal analysis – 5th vibration mode of Rio-Torto bridge
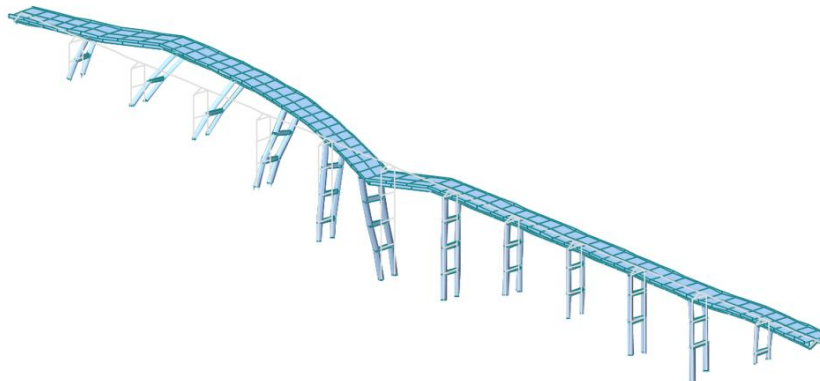
Figure 5.19 Modal analysis – 6th vibration mode of Rio-Torto bridge
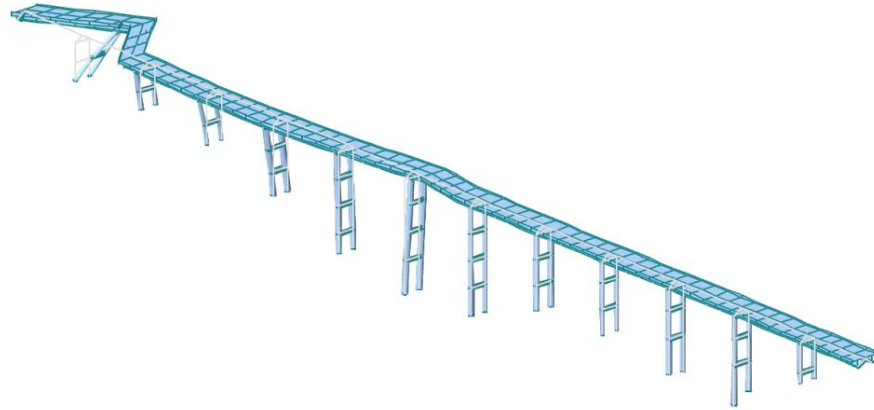
Figure 5.20 Modal analysis – 7th vibration mode of Rio-Torto bridge
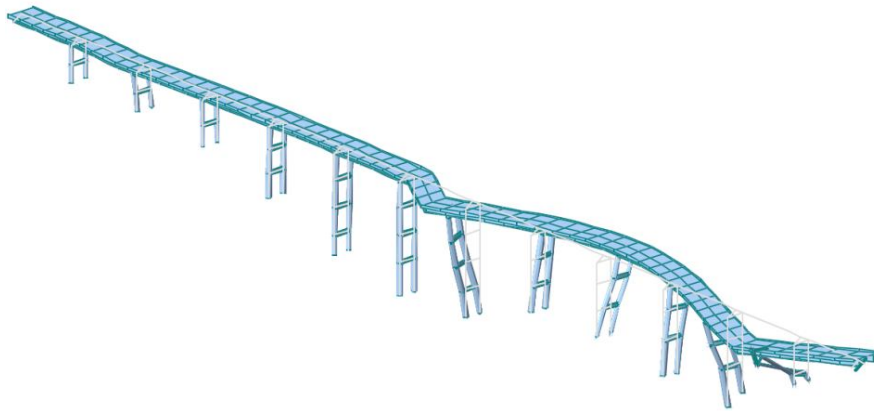
Figure 5.21 Modal analysis – 8th vibration mode of Rio-Torto bridge

The modes in which a local vibration of the piers and then its distributed mass is involved are very stiff modes. As an example, mode 24 is shown in (Fig 5.22) which is proves again that the mass of the piers can be neglected in calculating the seismic response of the viaduct.
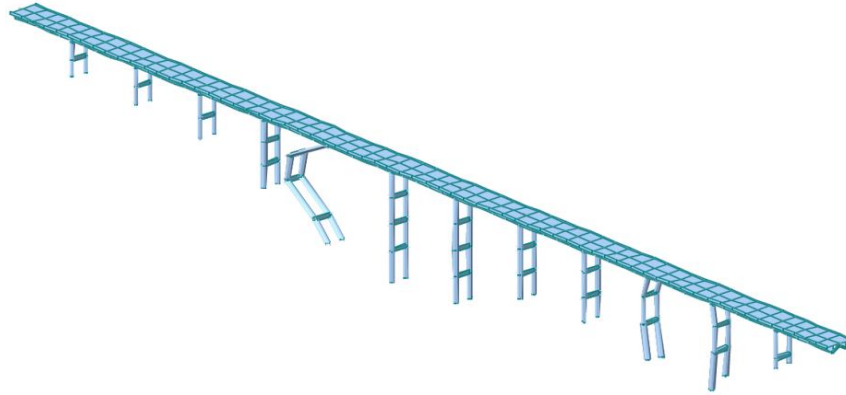
Figure 5.22 Modal analysis – 24th vibration mode of Rio-Torto bridge

In order to study the distributed mass of the piers along the height, another model for the viaduct with neglecting the masses of the piers has been carried out. The study of the modal analysis is shown in Table 5.3 as following:

Table 5.3 Comparison between modal analysis with and w/o the piers' masses

| Mode | direction | With pier masses | | Without pier masses | |
		Period [s]	Participation mass [%]	Period [s]	Participation mass [%]
1	Longitudinal	3.23	$Dy = 93.0$	3.10	$Dy = 99.99$
2	Transversal	1.58	$Dx = 27.3$	1.47	$Dx = 27.0$
3	Transversal	1.45	$Dx = 2.9$	1.34	$Dx = 4.0$
4	Transversal	1.40	$Dx = 24.89$	1.32	$Dx = 24.0$
5	Transversal	0.94	$Dx = 7.14$	0.91	$Dx = 8.38$
6	Transversal	0.91	$Dx = 22.47$	0.87	$Dx = 26.36$
7	Transversal	0.81	$Dx = 4.55$	0.78	$Dx = 3.95$
8	Transversal	0.68	$Dx = 0.0058$	0.679	$Dx = 0.0058$

The analysis is clearly demonstrated the limited influence of the mass distribute along the height of the piers. It is also important to underline

that the influence of the rotational mass of the deck on the seismic response of the viaduct is very limited. It is true that piers during the lateral displacement rotate, but the excited mass involved in this movement is very limited.

So the variation of the normal forces in the pier's columns is very limited too and its variation is due only to the horizontal force applied at the top of the piers. Moreover, the elastic torsional modes of the deck are negligible and therefore their contribution is negligible as well.

5.1.3.2. Response spectrum analysis

Using the spectra illustrated in (Fig. 5.23) the response spectrum analysis of the entire viaduct has been carried out. The vertical action has been excluded from the analysis, and the two horizontal components have been combined with the SRSS rule.
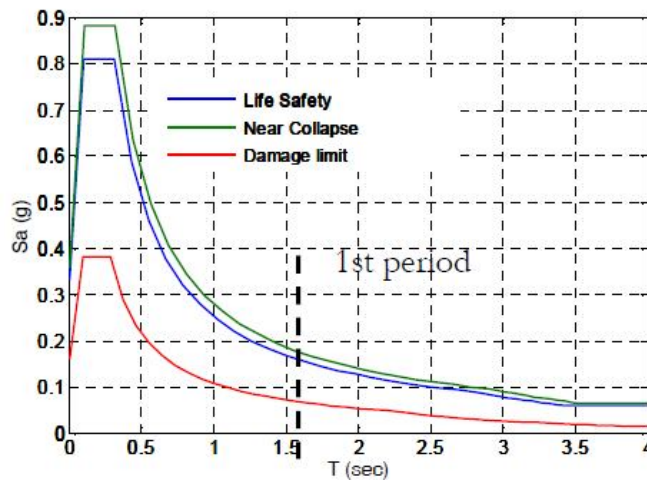
Figure 5.23 Response spectra of the viaduct according to the current Italian code (Soil A)

Figure 5.24 shows the deformation of the entire bridge. It indicates clearly the high involvement of pier 9 and 11, beyond that of pier 7 and 8 that are the most solicited. The maximum displacement of pier 9 and 11 is about

12 cm that corresponds to the maximum stress in terms of axial force, bending moment and shear indicated in (Fig. 5.25 - 5.27).
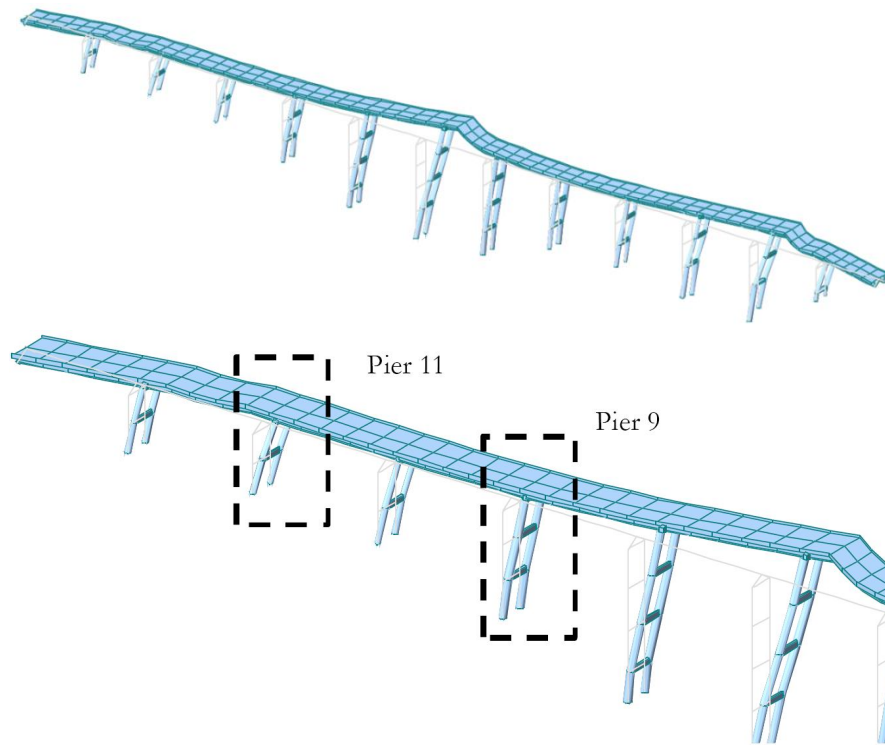
Figure 5.24 Response spectrum analysis: Deformation of Rio-Torto viaduct

Figure 5.25 Response spectrum analysis stresses: Axial force (kN)

Figure 5.26 Response spectrum analysis stresses: bending moment (kN.m)
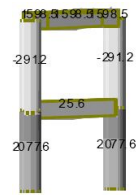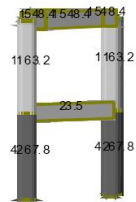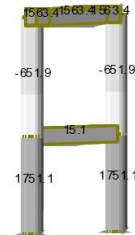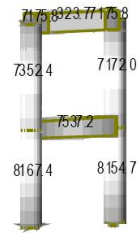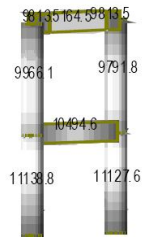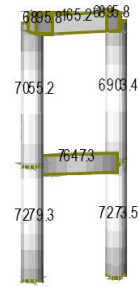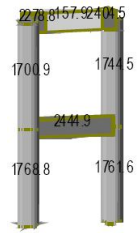
Pier 12
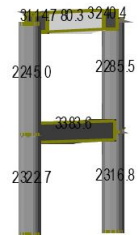
Pier 11
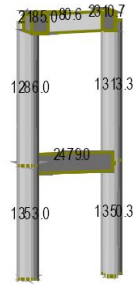
Pier 10
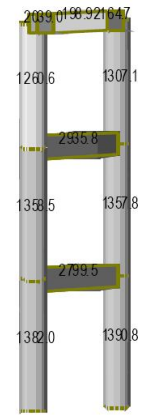
Pier 9
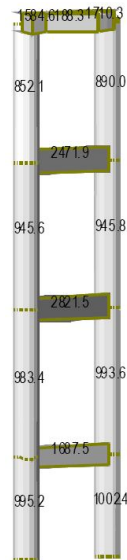
Pier 8
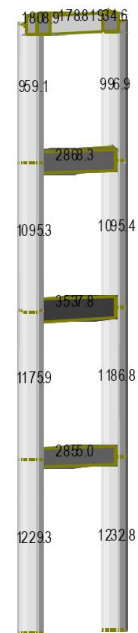
Pier 7
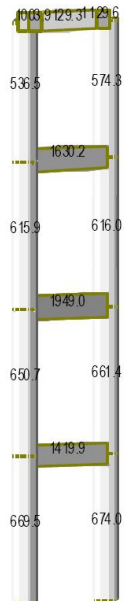
Pier 6
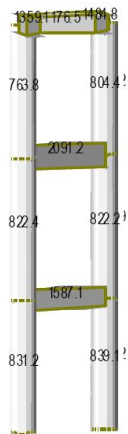
Pier 5

Figure 5.27 Response spectrum analysis stresses: shear (kN)

The results show clearly that the maximum strength in terms of shear of the transverse beams and of bending moment of the column exceeded the elasticity limit. For example, for pier 11 the maximum displacement is about 12 cm. This corresponds to a base shear of about 2300 kN as shown in (Fig. 5.27). The non-linear cyclic behaviour of the piers illustrated in (Fig. 5.28) shows that the pier would be fully plasticized in case of non linear behaviour.

A similar conclusion can be drawn for the transverse beam, where the elastic shear and moment are greater than the maximum strengths. In conclusion the viaduct under the seismic action would be subjected to a fully non-linear behaviour. This proves that there is a need for accurate modelling including all the local phenomena (e.g. shear deformations, buckling, strain penetration, etc…) that has an important influence on the seismic behaviour of this kind of bridges.
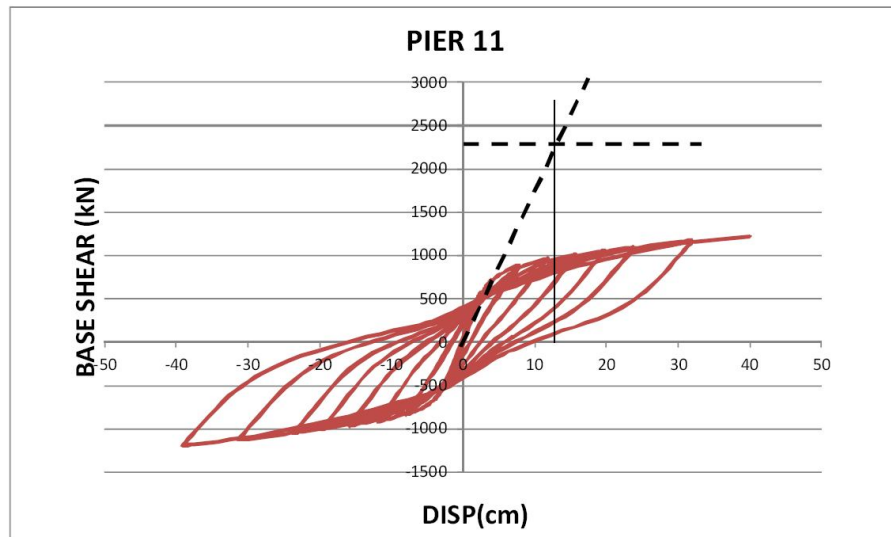
Figure 5.28 Comparison between linear and non-linear response

5.2. Seismic response analysis of the refined model using OpenSEES

This section is showing the choosing of data input to be used for the PsD testing for the Serviceability Limit State and Ultimate Limit State. Then, the response of the refined model implemented by OpenSEES is shown for both as-built and Isolated cases.

5.2.1 Selection of the data input

5.2.1.1 Definition of Serviceability Limit State (SLS)

The Serviceability Limit State defined to present the slight damage condition corresponds to the formation of hireline cracks in the transverse beams and at bottom sections of columns. According to this definition and the experimental campaign conducted at University Roma Tre (Paolacci & Gennini, 2012), it has been possible to identify the displacement at the top pier 9 and 11 corresponding to slight damage conditions. Table 5.5 shows the values of displacement and drift corresponding to three different level of damage in the transverse beam carried out for pier #12: a) slight damage, b) moderate damage c) extensive damage (Fig. 5.29), which corresponds to a drift level 0.003, 0.01 and 0.02 respectively (Alessandri et al. 2012) . Extending these results to pier #9 and #11, we obtain a limit displacements for slight damage equal about to 4.0 cm and 7.0 cm, respectively (Fig. 5.30, 5.31).

Figure 5.32 and 5.33 show the shear-deformation cycle of the transverse beams and the Moment-curvature cycle of the bottom section of columns of pier #9 and #11. Slight conditions correspond substantially to an elastic behaviour of the members.
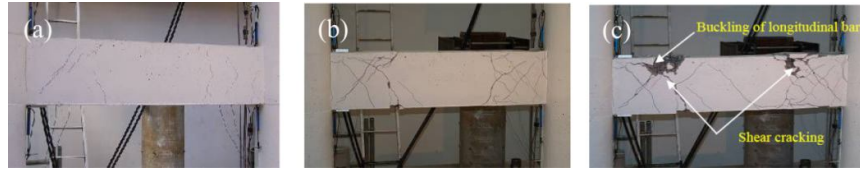
Figure 5.29 Cracks pattern in the transverse beam observed during the experimental test at University Roma Tre: a) hairline cracks, b) moderate crack c) extensive cracks
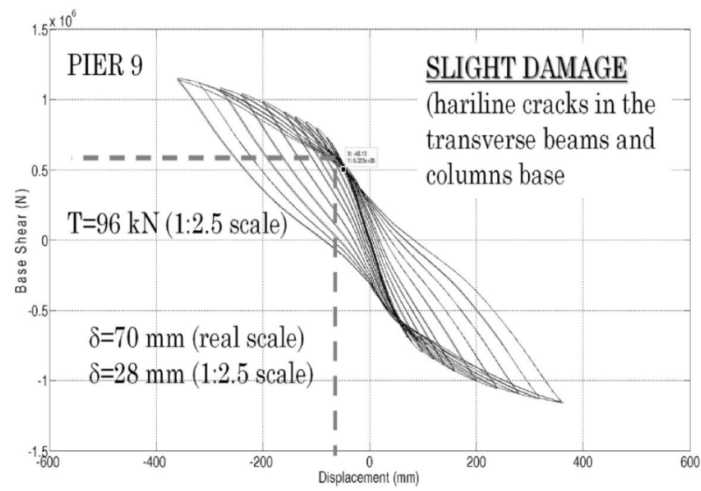
Figure 5.30 Serviceability Limit State - Pier 9
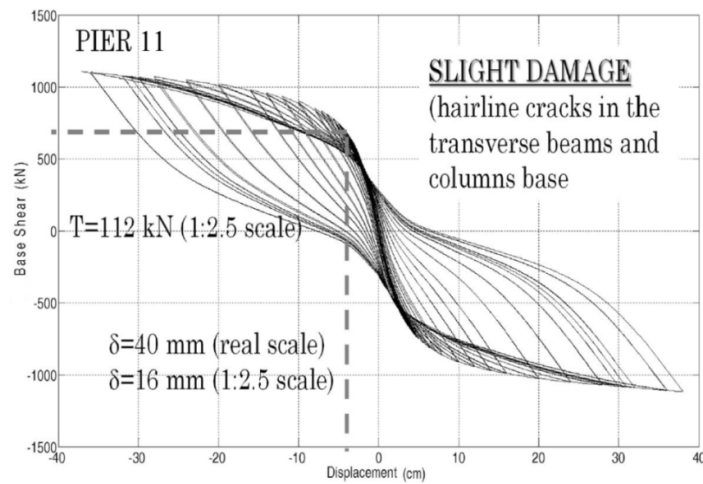
Figure 5.31 Serviceability Limit State - Pier 11

Table 5.4 Drift for the observed damage in the transverse beam of pier #12

Observed damage description	Symbol	Drift mean value
Low damage (Hairline cracks)	θ_1	0.0030
Medium damage (Onset of concrete spalling – development of shear cracks)	θ_2	0.01
Severe damage (Wide cracks widths – longitudinal bar buckling)	θ_3	0.02
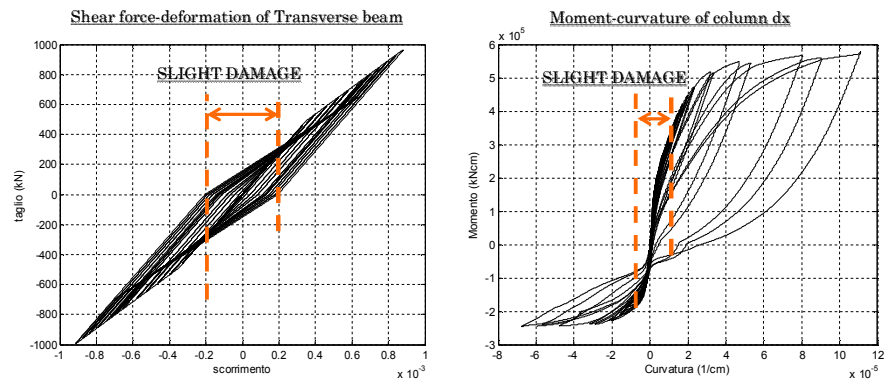
Figure 5.32 Serviceability Limit State - Pier # 9
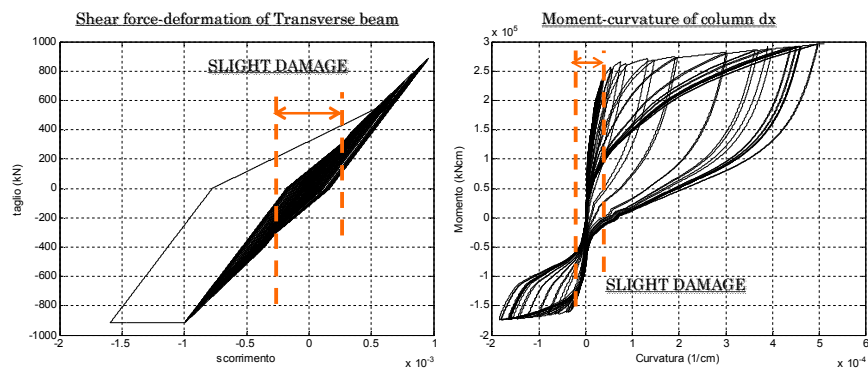
Figure 5.33 Serviceability Limit State - Pier # 11

5.2.1.2 Selection of the input signals

Two limit states are considered for the seismic performance assessment of the "as built" Rio-Torto bridge: Serviceability Limit State (SLS) and Ultimate Limit State (ULS), respectively. Given the geographical position of the bridge and the recent earthquake swarms occurred in the region (especially the earthquake records of the 20th and 29th May 2012), it was assumed to use the seismic records of the 2012 Emilia (Italy) earthquakes. The Mirandola records (MRN station) were utilized because of their seismological characteristics, i.e. PGAs and duration of the accelerograms. The record of May 29th East-West was used for the SD and the North-South component was used to assess the seismic performance at the ULS.

5.2.1.2.1. Serviceability Limit State Slight (SLS)

The earthquake record, velocity and displacement time histories for the 29th May 2012 East-West component are shown in (Fig. 5.34). In the figure, the red line are the uncorrected signals, the black lines are the correct one. The correction is realized with a baseline correction on the acceleration profile and then it is applied a pass-band Butterworth filter in the interval [0.25 Hz - 25.0 Hz]
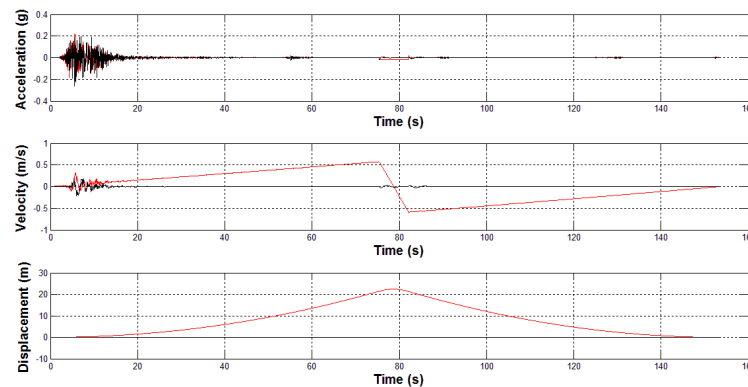
Figure 5.34 Record of the 29th May 2012 (W-E Component): acceleration (top), velocity (middle) and displacement (bottom) response histories
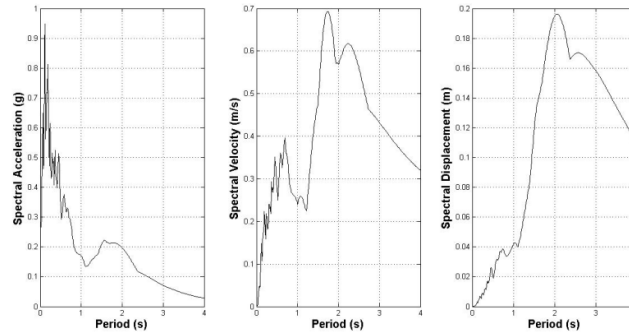
Figure 5.35 Response spectra of the record of the 29th May 2012 (East-West Component): acceleration (left), velocity (middle) and displacement (right) spectra

The response spectra of the sample record are provided in (Fig. 5.35). It shows a significant amplification for low-periods (between 0.5 and 1.0 seconds); values of spectral accelerations around 0.20g are also found in a period range 1-1.5 seconds, i.e. similar to the important natural periods of the part of the "as built bridge" in which pier 9 and 11 are placed. The length of the signal has been reduced assuming for its significant length that for which the Arias intensity is up to 99.4% (see Fig. 5.36). The filtered signal is shown in (Figure 5.37).
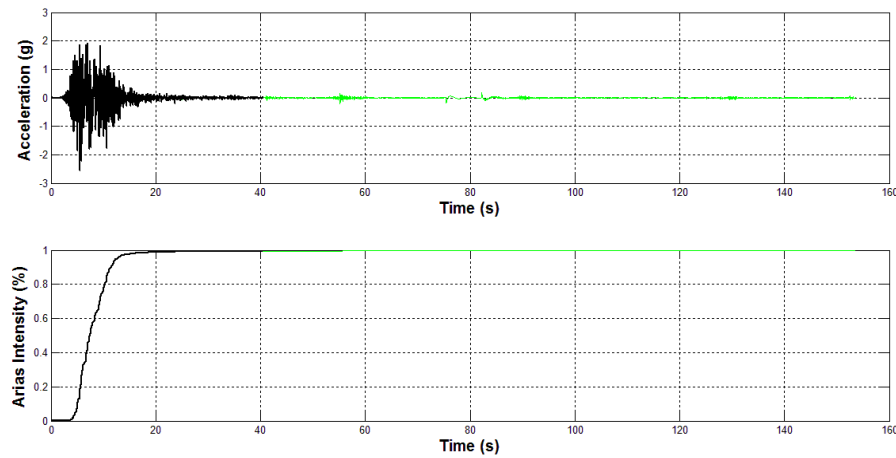
Figure 5.36 Reduction of the signal length
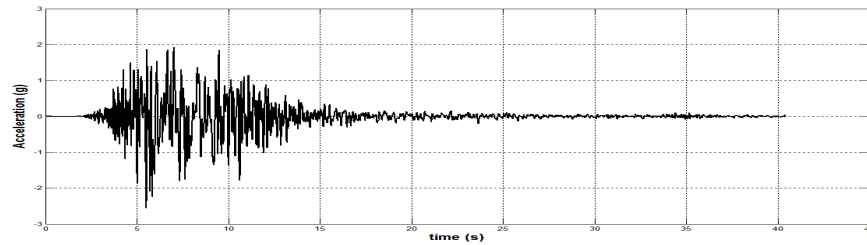
Figure 5.37 Final signal used in the numerical simulations

5.2.1.2.2 Ultimate limit state (ULS)

The earthquake record relative to the North-South component of the 29th May seismic event, as recorded in Mirandola, is shown in (Fig. 5.38), along with the velocity and displacement response history. As discussed earlier, the red line in the above figure are the uncorrected signals, the black lines are the correct one. The correction is realized with a baseline correction on the acceleration profile and then by applying a pass-band Butterworth filter in the interval [0.25 Hz - 25.0 Hz].
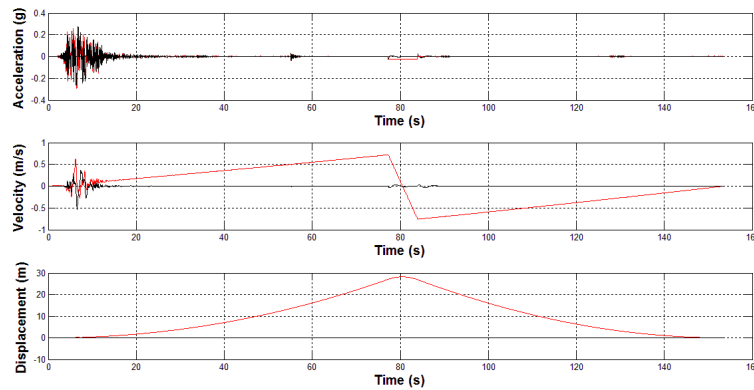
Figure 5.38 Record of the 29th May 2012 (N-S Component): acceleration (top), velocity (middle) and displacement (bottom) response histories
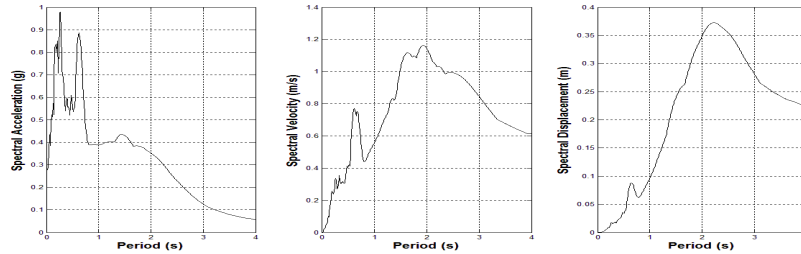
Figure 5.39 Response spectra of the record of the 29th May 2012 (East-West Component): acceleration (left), velocity (middle) and displacement (right) spectra

The response spectra of the sample record are provided in (Fig. 5.39). It shows a significant amplification for low-periods (between 0.5 and 1.0 seconds); values of spectral accelerations around 0.40g are also found in a period range 1-1.5 seconds, i.e. similar to the important natural periods of the part of the "as built bridge" in which pier 9 and 11 are placed. The length of the signal has been reduced assuming for its significant length that for which the Arias intensity is up to 99,4% (see Fig. 5.40). The input has been selected in order to respond to the compatibility criteria with the ULS design spectra dictated by EN1998:1. The signal used in the analysis is shown in (Fig. 5.41).
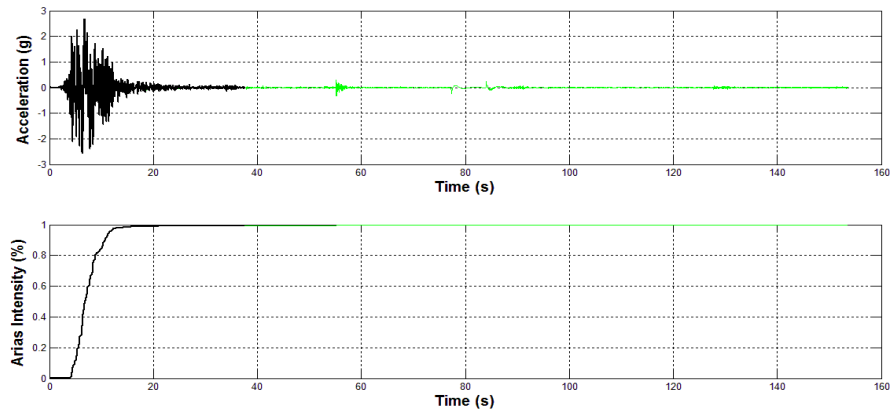
Figure 5.40 Reduction of the signal length
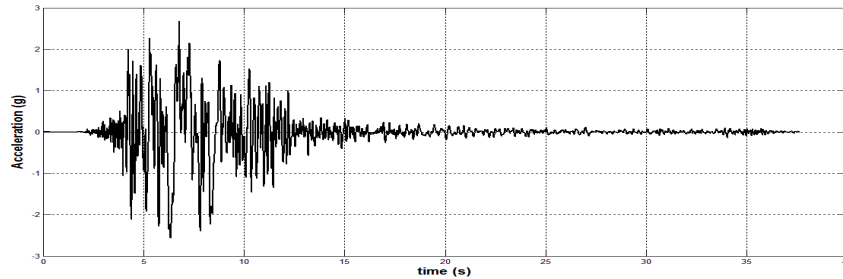
Figure 5.41 Final signal used in the numerical simulations

5.2.2. Modal analysis of the viaduct using OpeSEES model

Figures 5.42 - 5.45 show the main modes of the viaduct. The first mode is in the longitudinal direction with a period of 3.2 sec. A so long period depends on the introduction of gap elements for the Gerber saddles. Because, PsD test will be carried out only in the transversal direction, the saddles in the final numerical model have been considered a pinned connection, thus without relative longitudinal movement. The second mode is in the transversal direction which involves pier 9 and 11, as well as the 5th vibration mode with % of mass equal to 30.35% and 19.48% respectively.

This means that almost 50% of the entire mass participates to the vibration modes that involve pier 9 and 11. This observation suggests that the seismic response of the viaduct from pier 7 to 11 might be analyzed separately from the remaining part of the viaduct. But because, in the isolated case the deck will be continuous, for an effective comparison, it is decided to analyze the entire bridge also in the "as built case ".
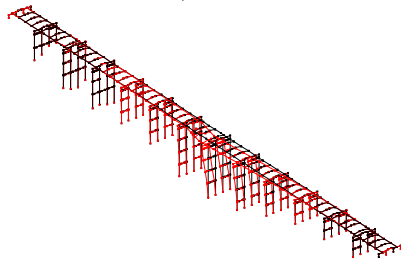
Figure 5.42 Opensees 2nd Eigenmode
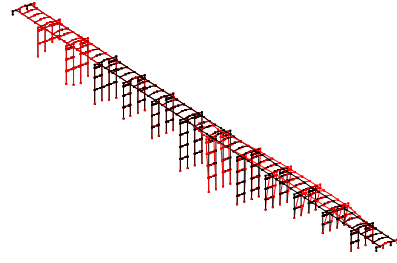
Figure 5.43 Opensees 5th Eigenmode

$T_{11} = 0.410$ s
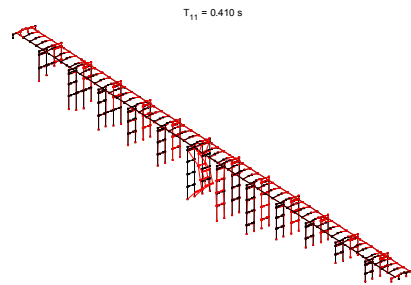
Figure 5.44 Opensees 20th Eigenmode

$T_7 = 0.663$ s
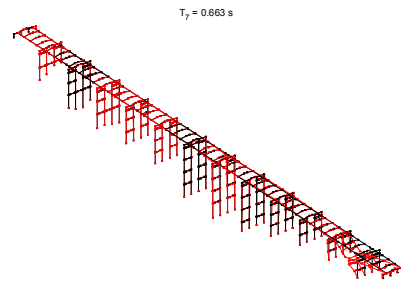
Figure 5.45 Opensees 25th Eigenmode

The significant eigenvalues and the participating masses of the viaduct are reported in (Table 5.5)

In order to study the distributed mass of the piers along the height, another model for the viaduct with neglecting the masses of the piers has been carried out. From the analysis, whose results are omitted for brevity, is demonstrated the limited influence of the mass distribute along the height of the piers.

It is also important to underline that the influence of the rotational mass of the deck on the seismic response of the viaduct is very limited. It is true that piers during the lateral displacement rotate, but the excited mass involved in this movement is very limited. So the variation of the normal forces in the pier's columns is very limited too and its variation is due only to the horizontal force applied at the top of the piers. Moreover, the

elastic torsional modes of the deck are negligible and therefore their contribution is negligible as well.

The modes in which a local vibration of the piers and then its distributed mass is involved are very stiff modes. An example is shown in the following figures. This proves again that the mass of the piers can be neglected in calculating the seismic response of the viaduct.

Table 5.5 Eigenvalues and excited masses of Rio-Torto viaduct - Opensees

Mode	Period (sec)	Trans. X (%)	Trans. Y (%)	Rot X (%)	Rot Y (%)	Rot Z (%)
1	3.05	0.00	91.63	11.81	0.00	0.00
2	1.58	30.35	0.00	0.00	1.05	1.73
3	1.45	3.32	0.00	0.00	0.23	1.77
4	1.40	26.69	0.00	0.00	2.24	26.29
5	0.90	19.48	0.00	0.00	3.60	27.95
6	0.82	5.94	0.00	0.00	1.27	13.02
7	0.72	4.80	0.00	0.00	0.80	14.87
8	0.65	0.18	0.00	0.00	0.26	0.18
9	0.58	0.01	0.00	0.00	0.01	0.00
10	0.53	0.07	0.00	0.00	6.15	0.00

5.2.3 Simulation of NL response of the As-built configuration

In this section some results based on the numerical model developed in OpenSEES are described. After having described the selection of input signals, the non-linear behaviour both globally and locally of each pier will be reassumed. For this purpose, the non-linear model, previously described, has been used.

5.2.3.1 Analysis of the response of SLS

In this section the response to the accelerogram SLS is presented and discussed. The results are presented in terms of maximum lateral displacement of piers, maximum base shear of piers, cyclic response of each pier, maximum shear in the transverse beam and maximum slip at bottom section of columns (Figure 5.46 – 5.58).

Figure 5.46 and 5.47 show the maximum lateral displacement and the maximum base shear of each pier. It can be noticed that the maximum absolute displacement (~ 20 cm) is, as expected, in the taller pier (#7), whereas pier #9 and #11 present a maximum displacement of 65 mm and 55 mm, respectively. This clearly shows that the Serviceability Limit State is fully respected for pier # 9, whereas for pier # 11 is overcome of about 35%. Therefore, during the test it is suggested to increase the PGA starting from a value of 50% of the maximum PGA for SDC (0.25 g).

The maximum base shear is about 870 kN for pier #11 and 1000 kN for pier #11. These values are greater than the values predicted in the static cyclic analysis. This is due to the dynamic component of the motion.
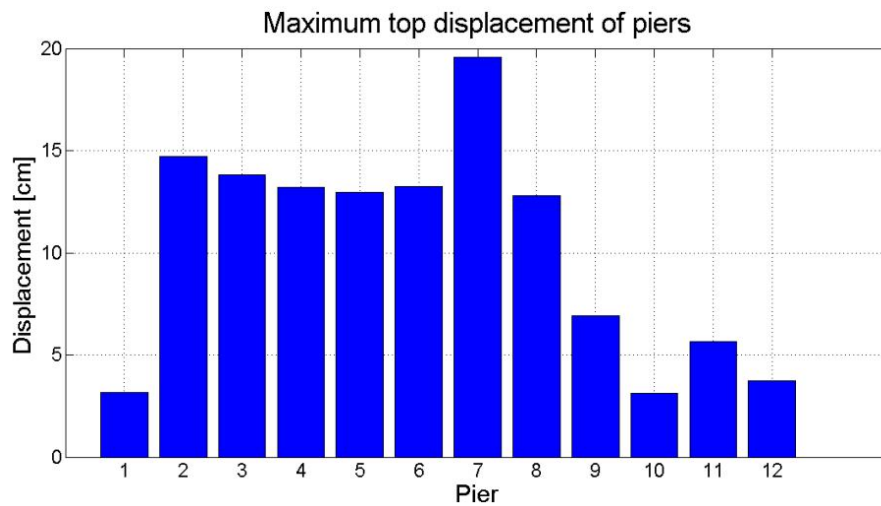
Figure 5.46 Maximum lateral displacement of piers
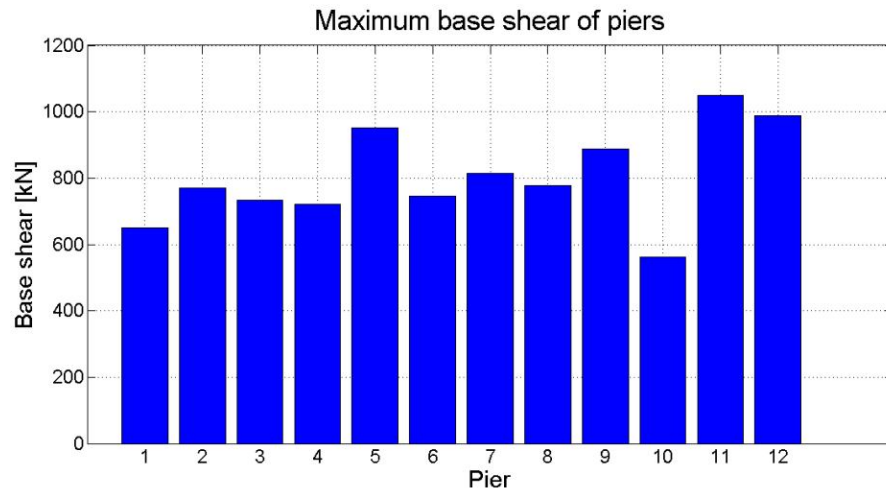
Figure 5.47 Maximum base shear of piers
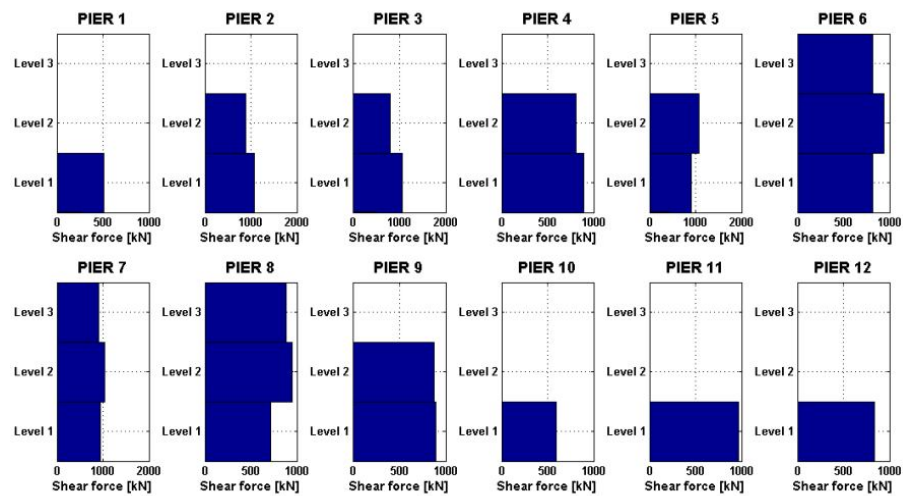
Figure 5.48 Maximum shear force in the transverse beam
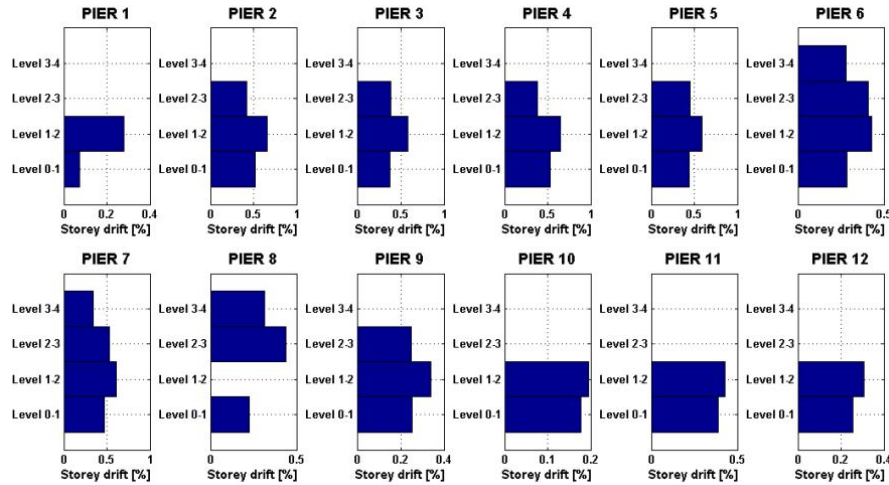
Figure 5.49 Maximum inter-storey drift

Global and local cyclic response of the piers show that their behaviour is confined to the elastic field as demonstrated both in (Fig. 5.50), where the force-deflection cycles of each piers is shown, and in (Fig. 5.51 and 5.52) whose behaviour is therefore elastic. Similarly, transverse beams behave linearly, at least for shear actions, as clearly shown in (Fig. 5.54, 5.56, 5.58). This is also demonstrated by the maximum drift level that is < 0.6% (Fig. 5.30*). Under flexural action, transverse beam shows hysteresis, which is not negligible even if the number of cycles is very limited to (~1) and the plastic excursion is restricted to a maximum ductility of 2, and not for all piers (Fig. 5.53, 5.55, 5.57).

In conclusion the application of the input signal recorder during the Emilia earthquake of 29 May 2011 (Component WE) seems to respond to request of SLS. It will be applied during the PsD test in the preliminary phase of the test, to induce in the viaduct, and in particular in pier #9 and #11, a limited level of damage before the test in the isolated configuration.
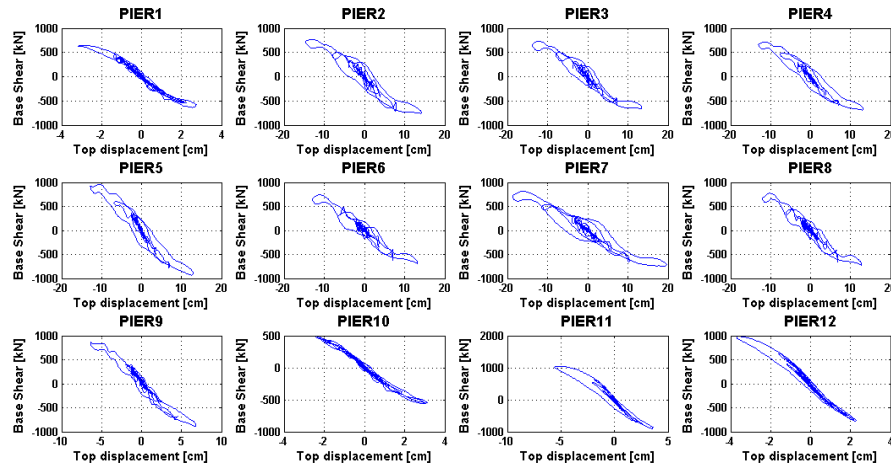
Figure 5.50 Hysteretic cycle response of piers
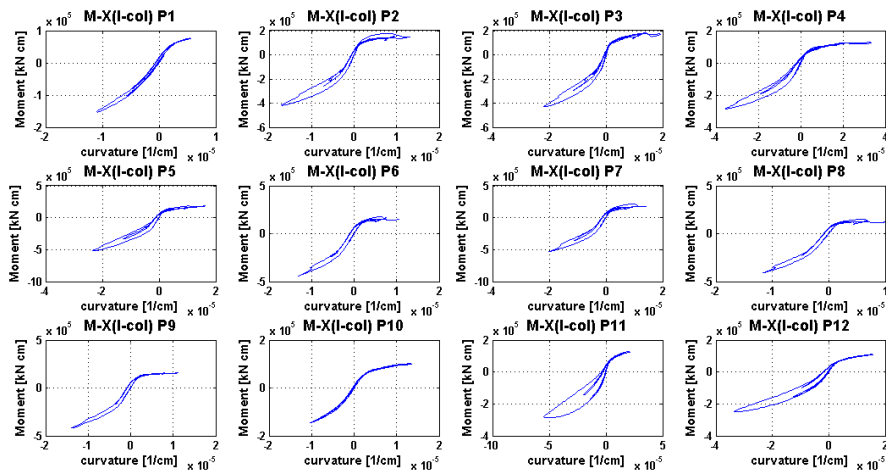
Figure 5.51 Moment-curvature cycles at bottom section of the left column of each pier
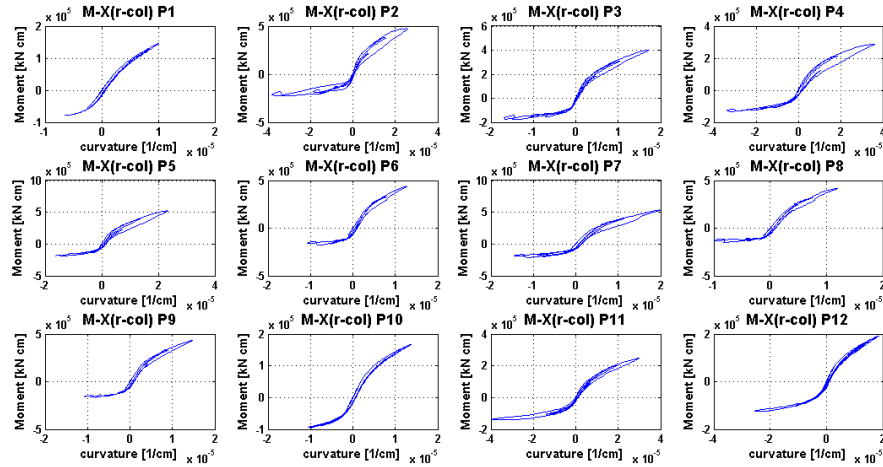
Figure 5.52 Moment-curvature cycles at bottom section of the right column of each pier
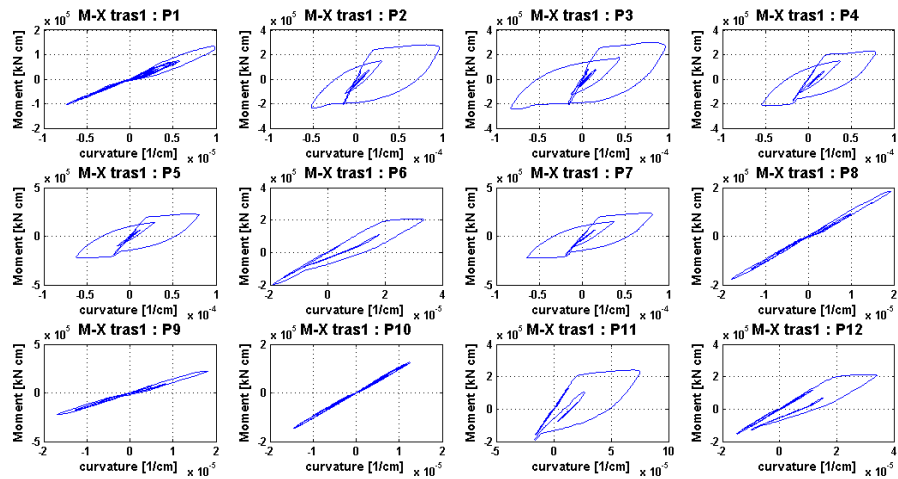
Figure 5.53 Moment-curvature cycles of the transverse beam at 1st level of each pier
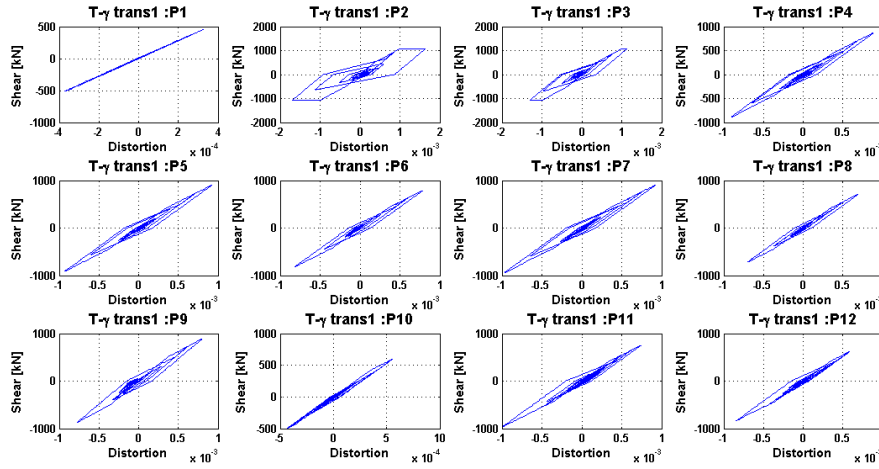
Figure 5.54 Shear force-deformation cycles of the transverse beam at 1st level of each pier
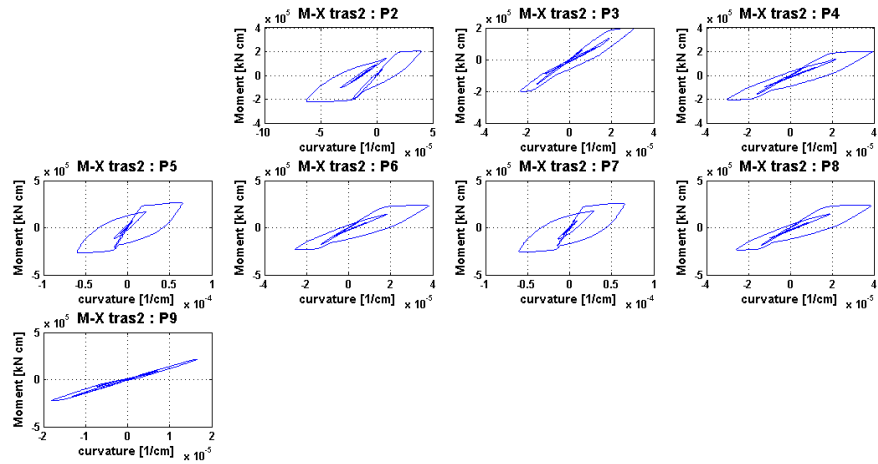
Figure 5.55 Moment-curvature cycles of the transverse beam at 2nd level of each pier
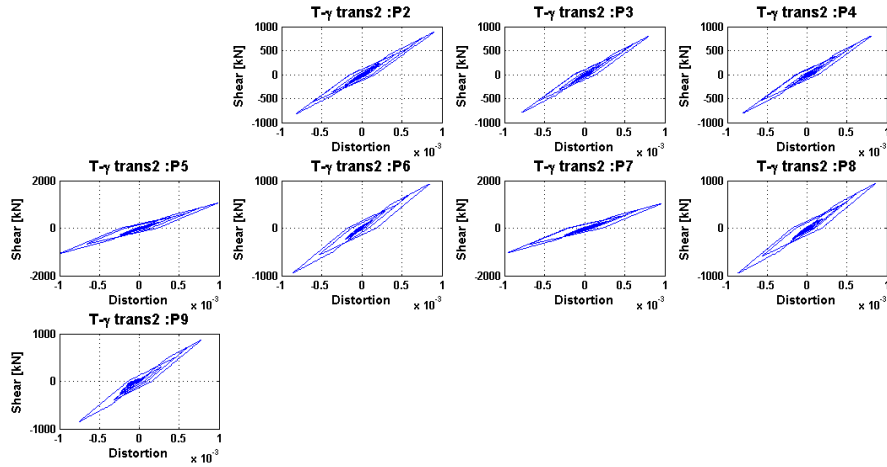
Figure 5.56 Shear force-deformation cycles of the transverse beam at 2nd level of each pier
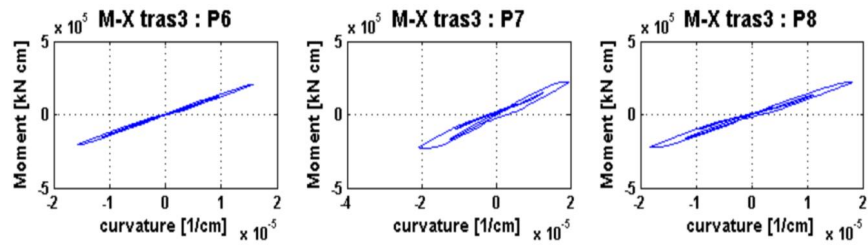
Figure 5.57 Moment-curvature cycles of the transverse beam at 3rd level of each pier
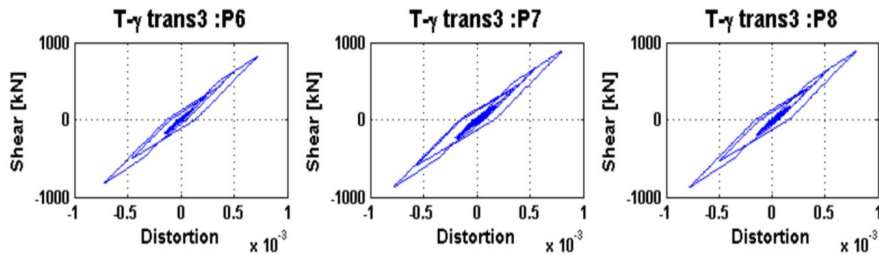
Figure 5.58 Shear force-deformation cycles of the transverse beam at 3rd level of each pier

5.2.3.2 Analysis of the response for ULS

In what follows, the results of numerical simulation of the entire viaduct, subjected to the Emilia earthquake of 29th May 2011 (NS component) are presented and briefly discussed. In addition the response to the sequence N-S and WE components (main shock – aftershock sequence) is also presented.

In this section the response to the accelerogram SDC is presented and briefly discussed. The results are presented in terms of maximum lateral displacement of piers, maximum base shear of piers, cyclic response of each pier, maximum shear in the transverse beam and maximum slip at bottom section of columns (Fig. 5.59 - 5.70).
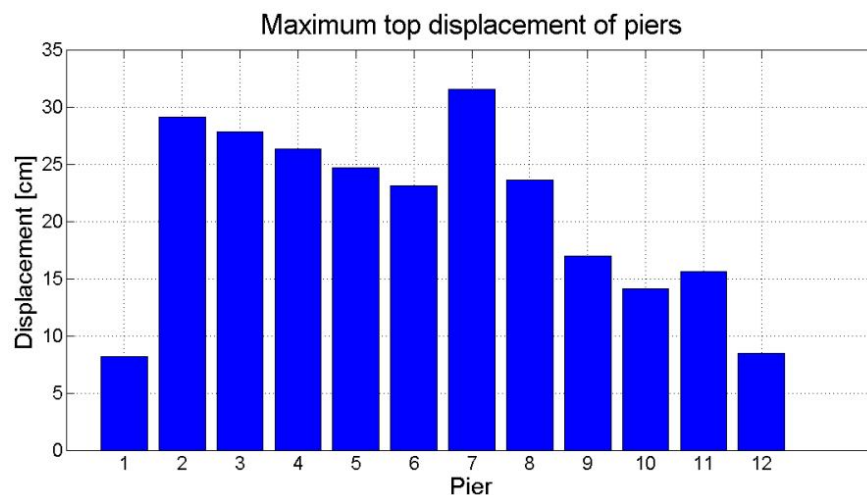
Figure 5.59 Maximum lateral displacement of piers
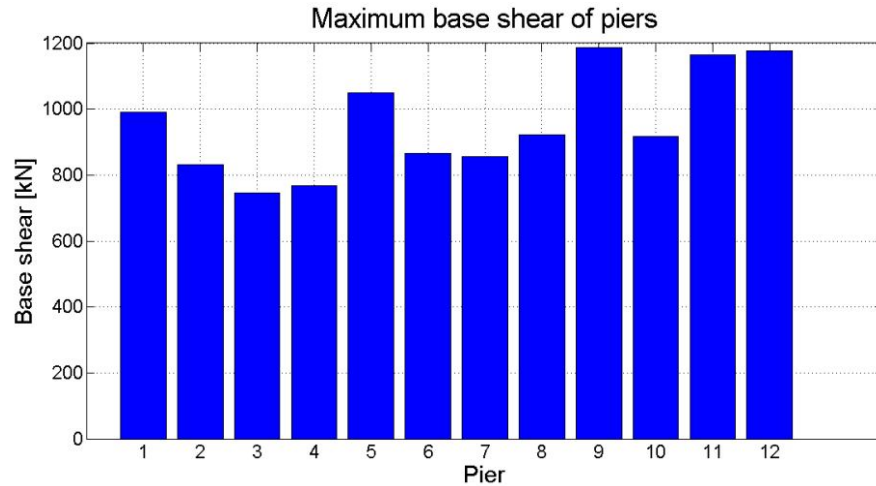
Figure 5.60 Maximum base shear of piers

Figure 5.59 and 5.60 show the maximum lateral displacement and the maximum base shear of each pier. It can be noticed that the maximum absolute displacement (~ 32 cm) is, as expected, in the taller pier (#7), whereas pier #9 and #11 present a maximum displacement of 17 cm and 15 cm, respectively. The maximum base shear is about 1200 kN both for pier #9 and #11. The analysis of the cyclic response (Fig. 5.63) shows the high plastic deformations to which pier #9 and # 11are subjected. A pronounced pinching effect is also present in the cyclic response of pier #11. This is due to the effect of shear and bond.

The expected level of crack width at the column base due to the bar slippage is of the order of 1.5 – 2 mm, as confirmed by the numerical model. In any case, the slippage is not enough to avoid flexural damage in the columns as shown by Moment-Curvature cycles in (Figure 5.64 and 5.65); in fact the maximum ductility is about 3.
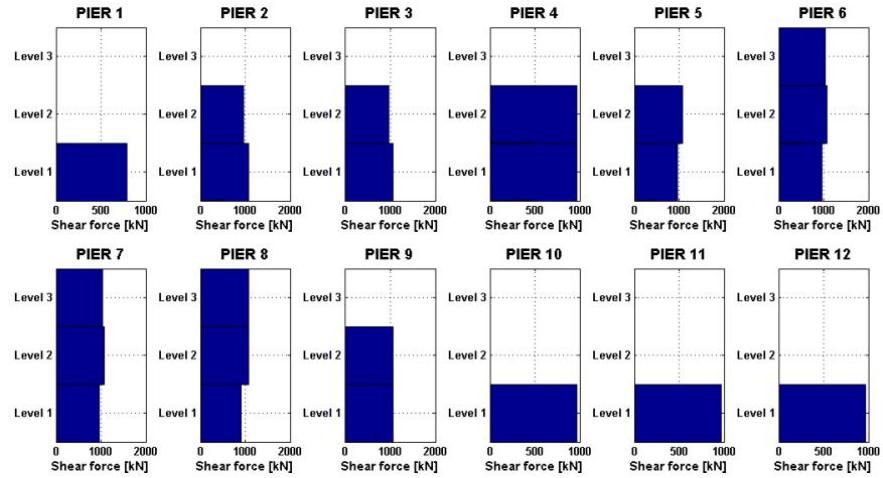
Figure 5.61 Maximum shear force in the transverse beam
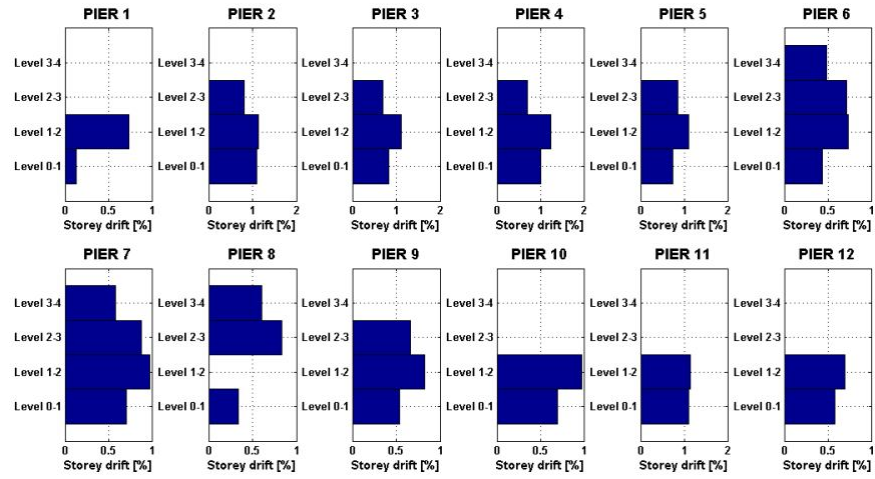
Figure 5.62 Maximum inter-storey drift
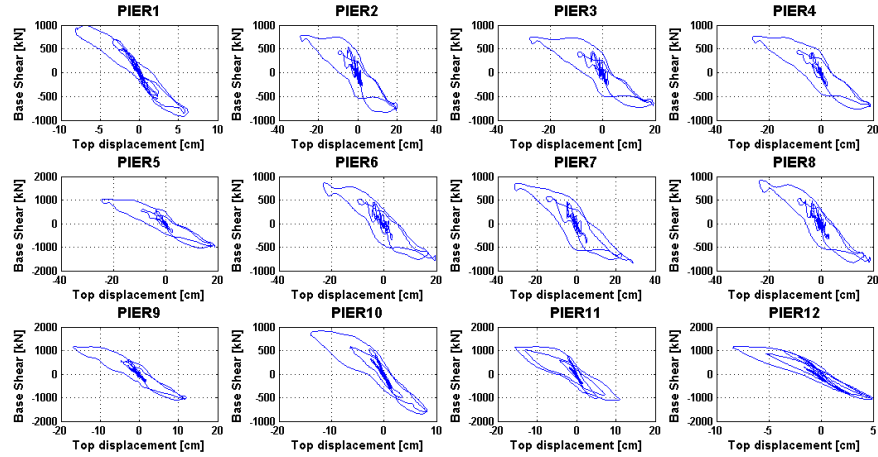
Figure 5.63 Hysteretic cycle response of piers
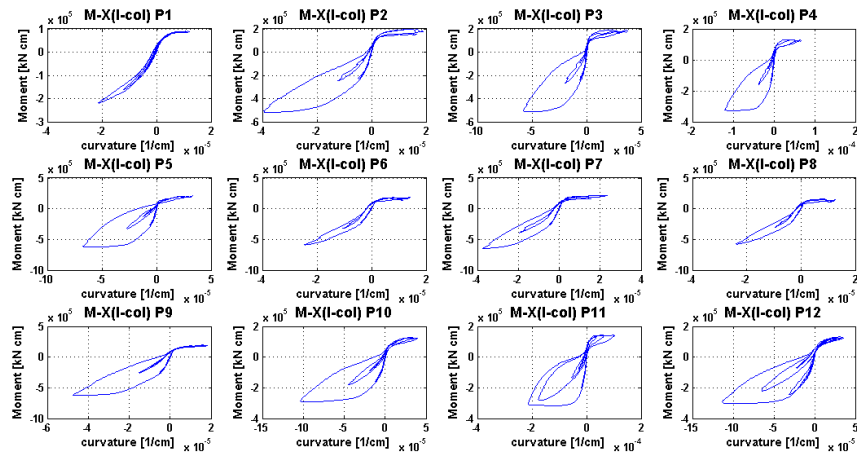
Figure 5.64 Moment-curvature cycles at bottom section of the left column of each pier
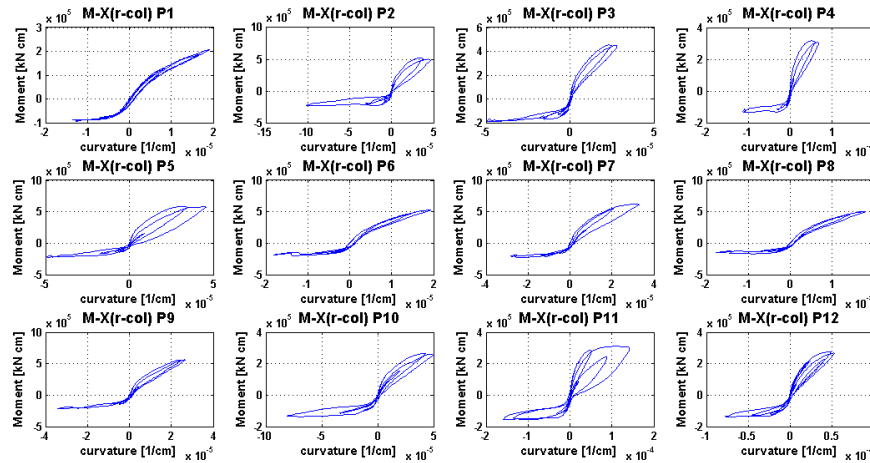
Figure 5.65 Moment-curvature cycles at bottom section of the right column of each pier

The level of shear damage in the transverse beam is also high as confirmed by the hysteretic behaviour shown in (Fig. 5.66, 5.68 and 5.70). The maximum shear deformation is 3×10^{-3} and 6×10^{-3} for pier #9 and #11 respectively, which correspond to an extensive shear cracking pattern as already shown in (Paolacci & Giannini, 2012).

In fact, for pier #12 has been demonstrated that 1% of drift corresponds to the shear failure of the transverse beam. Because the level of drift reached during the analysis is about 1% for pier #11 and 0.8 % for pier #9, hence extensive shear damage is expected, at least at 1st and 2nd level of piers.

The plastic flexural deformation of the transverse beam appeared to be not very high (ductility 3-4) with a limited number of cycles as shown in (Figures 5.67 and 5.69). Therefore a limited flexural damage level is expected.
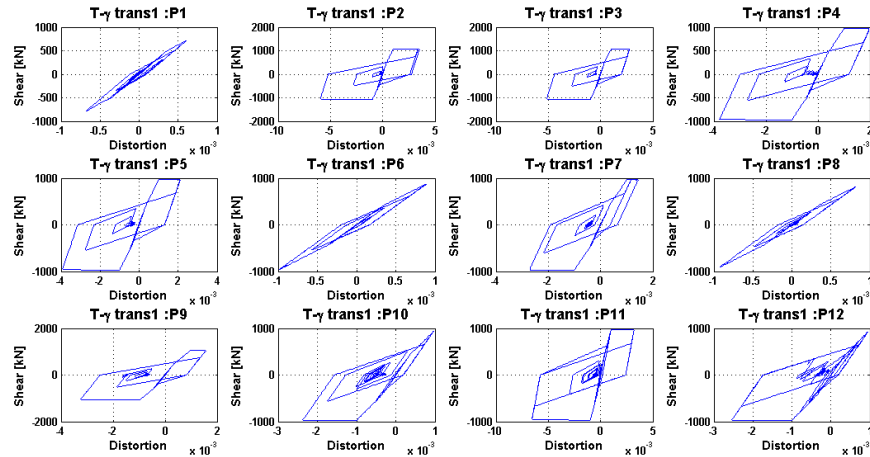
Figure 5.66 Shear force-deformation cycles of the transverse beam at 1st level of each pier
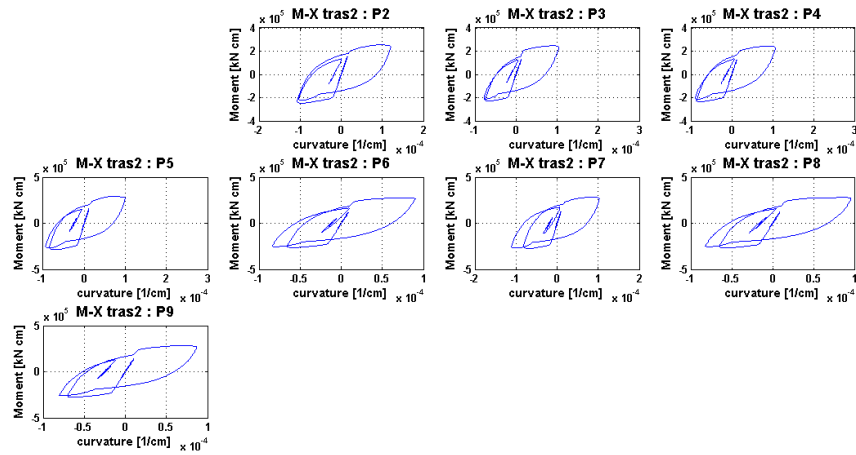
Figure 5.67 Moment-curvature cycles of the transverse beam at 2nd level of each pier
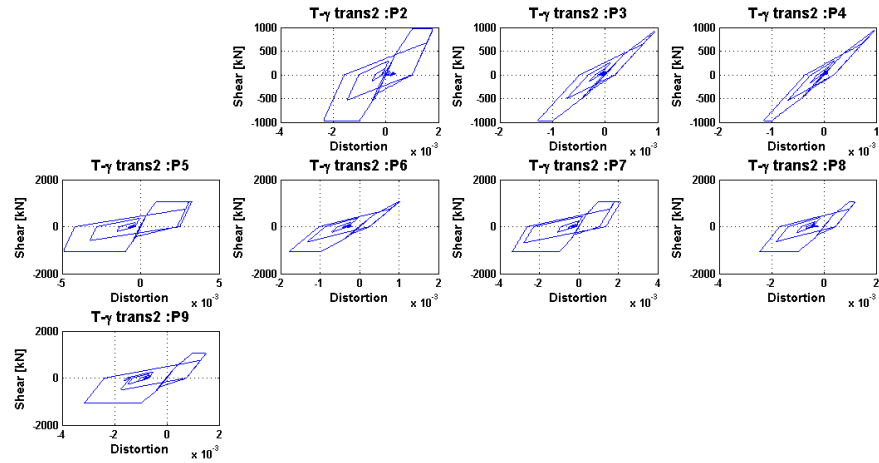
Figure 5.68 Shear force-deformation cycles of the transverse beam at 2nd level of each pier
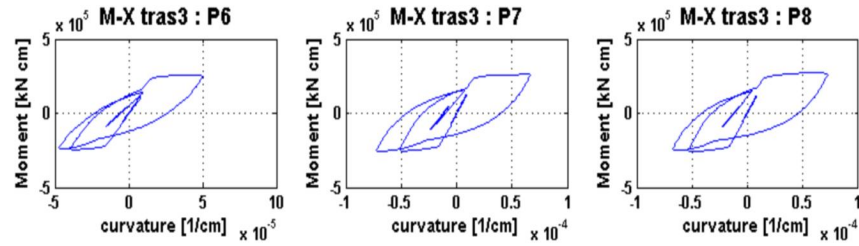
Figure 5.69 Moment-curvature cycles of the transverse beam at 3rd level of each pier
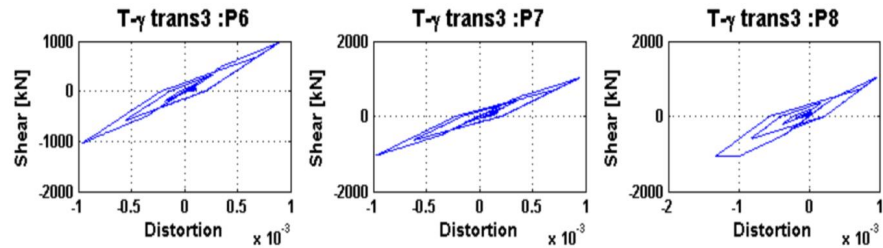
Figure 5.70 Shear force-deformation cycles of the transverse beam at 3rd level of each pier

5.2.4 Simulation of NL response of the Isolated configuration

The same input signals have been used for Isolated case. It is only worth to observe in the response spectra a significant amplification level around the period of the isolated viaduct (~ 2sec) values of spectral accelerations higher than 0.15g for WE component and 0.4 g for NS component. So, according to the design, an important reduction of the seismic effects is expected.

5.2.4.1 Simulation of the seismic test under SLS condition

The deck and piers maximum transversal displacement are displayed in (Fig. 5.71), in red and blue respectively. The maximum transverse displacement is about 18cm; the latter is found at the 6th pier. The maximum lateral displacement of the piers is about 14 cm (Pier #7). The deformed shape of the deck exhibits the maxima at mid-span, as expected. The maximum relative displacements occur for the deck between Piers 4 and 9.
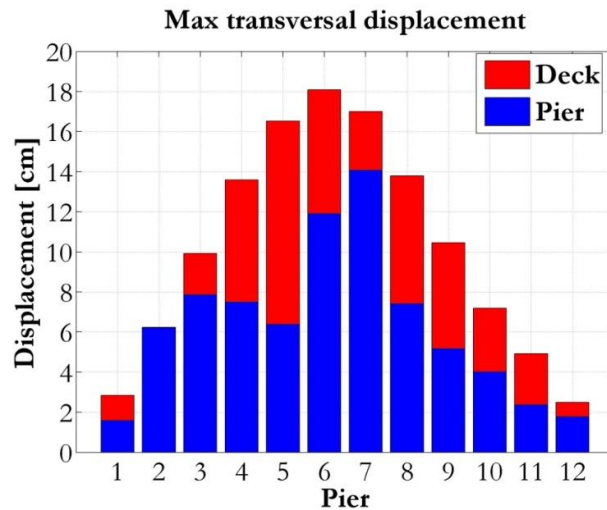
Figure 5.71 Deck and piers maximum transversal displacement

The difference between the displacements of the piers and the bridge deck is due to the devices activation. Figure 5.72 shows the hysteretic behaviour of the devices during the sample strong motion. The devices are activated for a first sliding shear of about 100 kN, as expected from a simplified analysis (i.e. $V = \mu * N \approx 0.04 * 2500 = 100kN$). It is also found that the highest energy dissipations for the devices installed on the top of piers between piers n.4 and 9 confirm the maximum relative displacements shown in (Fig. 5.72).

Additionally, the activation of the device causes the limitation of the transmitted shear from the deck to the piers; the latter behave elastically, thus inhibiting the onset of structural and non-structural earthquake-induced damage. Figures 5.73 and 5.74 illustrate the maximum base shear in the piers and the maximum storey drift for each pier, respectively.
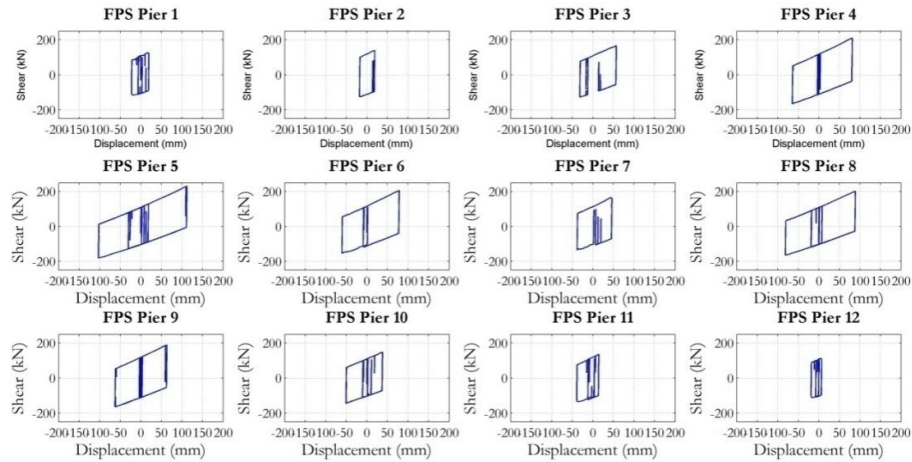
Figure 5.72 Hysteretic behaviour of the devices during the strong motion
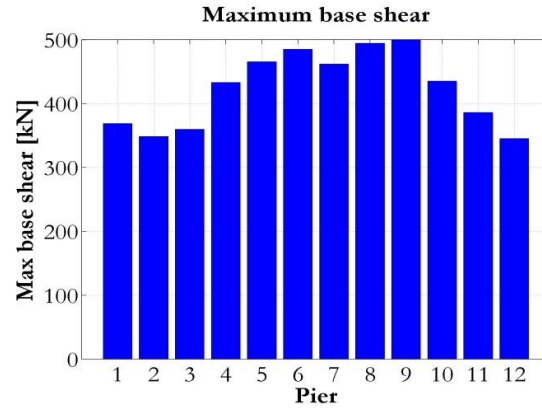
Figure 5.73 Maximum base shear

It was found in (De Risi & Di Sarno, 2011) that the first yielding of the bridge system is obtained for a base shear of about 500 kN. It is worth noting that Figure 78 proves that all the maximum base shear are lower than the latter yielding value, hence the occurrence of the inelasticity is prevented.
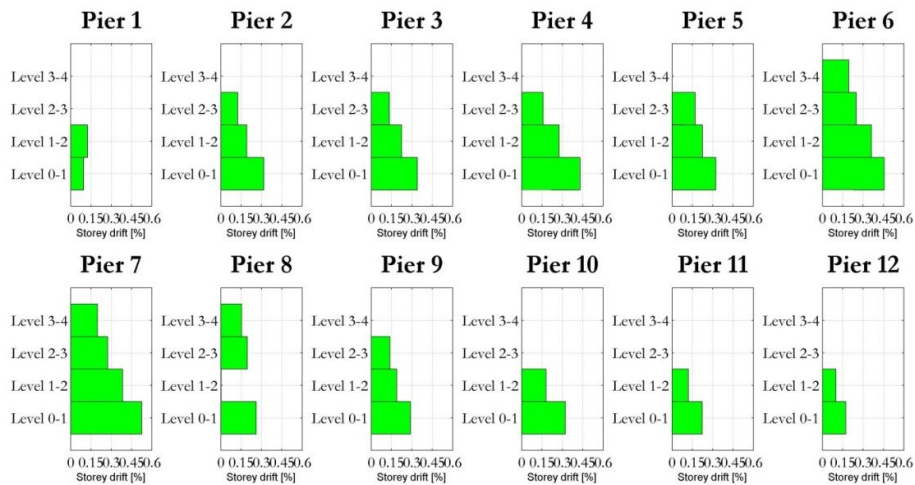
Figure 5.74 Maximum inter-storey drift
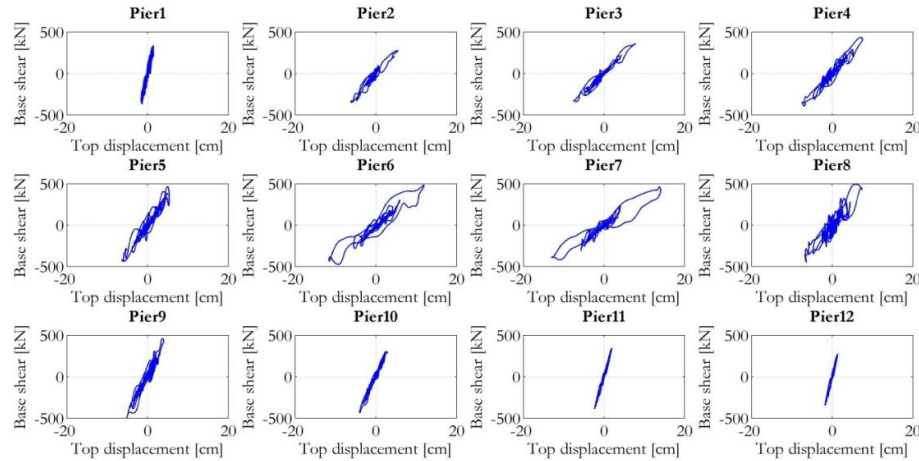
Figure 5.75 Hysteretic behaviour of the piers

As also observed in (Alessandri et al. 2012), the drift corresponding to the shear failure of transverse beam or to the failure of beam-column joints, is about 1%. All the values depicted in Figure 79 are lower or equal to 0.5%, thus the damage is avoided. Figure 5.75 provides the hysteretic behaviour of the single piers of the Rio-Torto bridge. It shows that the behaviour of the piers 9 and 11 is nearly linear.

The insignificant irregular response that can be observed in the behaviour of the pier 9 is caused primarily by the shear behaviour of the transverse beams, that is slightly activate, as shown in (Figure 4.76).
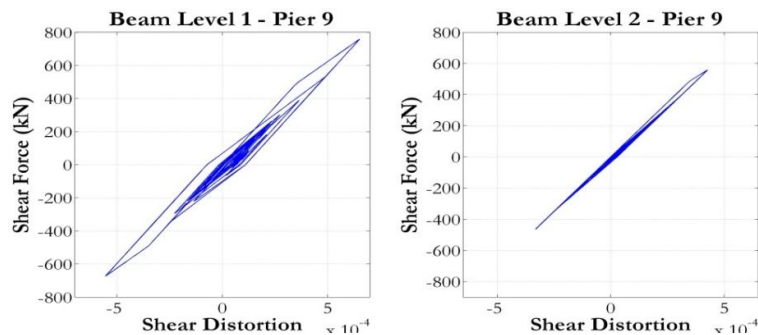
Figure 5.76 Hysteretic behaviour of the transverse beam

Further information and figures on the hysteretic behaviour of the other components of the viaduct are provided in Appendix B-1.

5.2.4.2 Simulation of the seismic response under ULS condition

Figure 5.77 shows the deck and piers maximum transversal displacement in red and blue respectively.
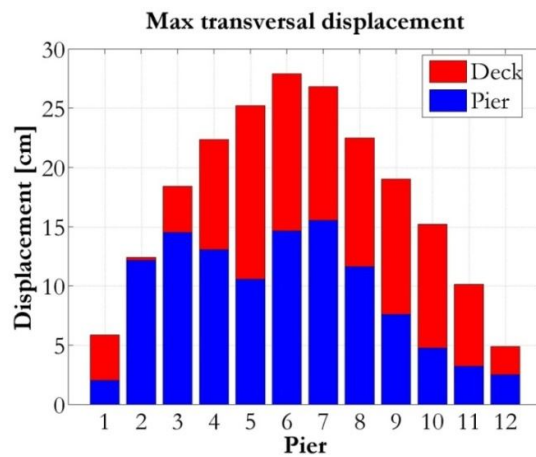
Figure 5.77 Deck and piers maximum transversal displacement

As stated earlier, the variations between the two depicted displacements are due to the devices activation. Figure 5.78 provides the hysteretic behaviour of the devices during the strong motion.
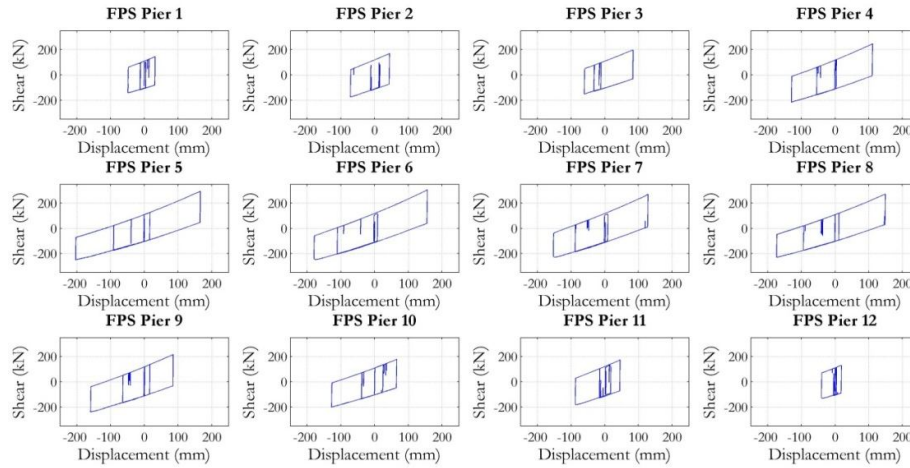
Figure 5.78 Hysteretic behaviour of the devices during the strong motion

The devices are activated for a first sliding shear of about 100 kN, as expected from a simplified analysis (i.e. $V=\mu*N\approx0.04*2500=100$ kN). It is worth to note that the activation of the device causes the limitation of the transmitted shear from the deck to the piers, which remain elastic. Figures 84 and 85 display the maximum base shear in the piers and the maximum storey drift for each piers, respectively.
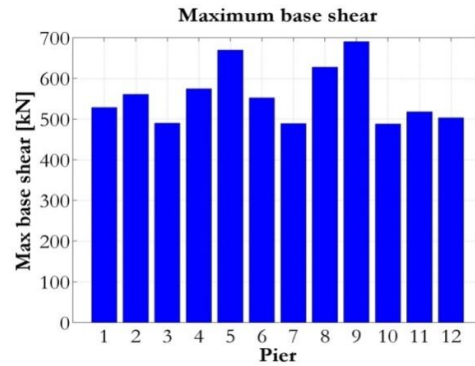
Figure 5.79 Maximum base shear

In (De Risi & Di Sarno, 2011), it was shown that the maximum strength is obtained for a base shear higher than 700 kN. Figure 5.79 proves that the maximum base shears are lower than the above base shear.
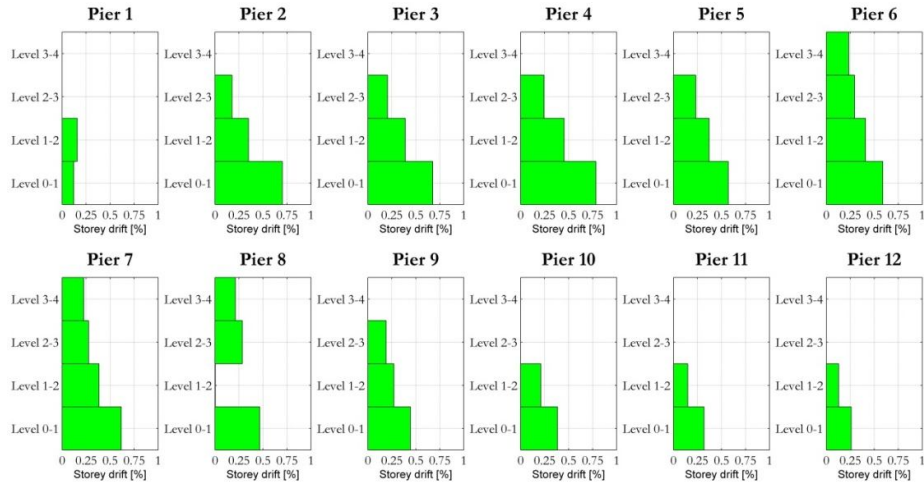
Figure 5.80 Maximum inter-storey drift
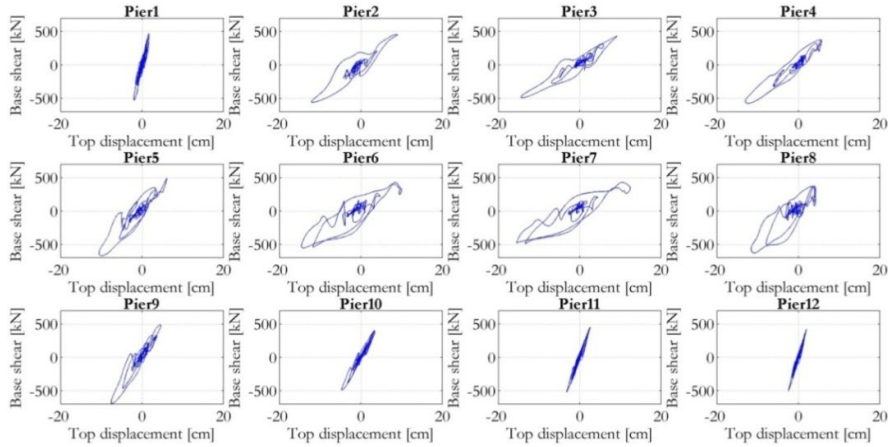
Figure 5.81 Hysteretic behaviour of the piers

As observed in (Di Sarno & Giannini, 2011), the drift corresponding to the shear failure of transverse beam or to the failure of beam-column joints is about 1%. All the values depicted in (Figure 5.81) are lower or equal to 0.7%, then the damage is avoided.

The hysteretic behaviour of each pier is summarized in (Fig. 5.81). It can be observed that the behaviour of the piers 9 and 11 are linear. The noise that can be observed in the behaviour of the pier 9, is due to shear behaviour of the transverse beam at first and second levels as well as flexural activation of the first level transverse beam. Additional information on the hysteretic behaviour of the other components of the viaduct are included in Appendix B-2.

6. MOCK UP'S DESIGN AND PSD TEST SETTING UP

The mock-ups design and the preliminary setting up of instruments and computers in the laboratory are essential steps of any large-scale experimental testing. The discussion here held on the scaling problem of and the detailing design of the pier mock-ups. The design and scaling has been verified for the Isolators too.

On the other hand, the setting up details done by ELSA laboratory technicians of the PsD testing the laboratory environment are discussed by showing the instruments and control strategy of both piers and Isolators. Subsequently, a reduced OpenSEES model used in the PsD testing and model updating in each step have been shown in this chapter.

6.1. Description of the Mock up's

6.1.1 Scaling

When performing an experimental test on a specimen the problem of scale reduction needs to be addressed. This is solved by making use of a dimensional analysis governed by the well-known Buckingham Theorem. A suitable scale reduction factor should be assumed in order to reduce lengths (Geometry and displacements) at a level compatible with the requirements of the experimental setup, especially in terms of maximum capacity of the actuators (Forces). This automatically reduces the cost of the experiment.

Thus the only reduction factors to be selected are those of length and forces. The others can be evaluated by a dimensional analysis. If we

assume that the model is made of the same material of the prototype, stress and strain can be kept constant. Forces and displacements are reduced by S^2 and S respectively, while the reduction factors of time and acceleration may be selected according to the needs of the test (Kumar et al. 1997), as shown in Table 6.1. If the acceleration is kept constant, the scale factor of time is simply $\sqrt{S}$ as the second Newton's law indicates.

Table 6.1 Scale factors used in PsD test

Quantity	Dimension	Scale Factor
Length	L	S
Mass	M	S^{-2}
Time	T	$\sqrt{S}$
Frequency	1/T	$1/\sqrt{S}$
Stress	$ML^{-1}T^{-2}$	1
Strain	L/L	1
Velocity	LT^{-1}	
Acceleration	LT^{-2}	1
Force	MLT^2	S^{-2}
Stiffness	MT^2	S

Considering the constraints for the construction and the positioning of the specimens in the laboratory, in particular the dimensions of the reaction wall and of the access door, a reduction scale of 1:2.5 was selected. So the specimens for pier 9 and 11 are going to be 11.5m and 7m, respectively.

6.1.2. Flexural and shear strength scaling

The correct flexural strength of columns and transverse beams was achieved with a rigorous geometrical scaling of the prototypes, including the diameters of reinforcement and their position. In particular for the columns of both piers 9 and 11, plain steel bars with diameters of 8 and 10 mm were used to respect the similitude requirements, given that the

original diameters of the prototype were 20 and 24 mm, with a small approximation for the 24 mm diameter bars.

Regarding the shear strength the problem deserves particular attention. Many authors in the past have clarified the problem (Krawinkler et al. 1988). In particular, it is necessary to scale diameter and spacing of stirrups to have a correct strength and confinement effect. Concerning piers 9 and 11, scaling of shear strength is particularly important for the transverse beams, while for the columns it is less of an important issue, owing to their high shear strength. For the transverse reinforcement of the transverse beam, with 8 mm diameter stirrups at maximum spacing of 20 mm for the prototype, a scaled diameter of 3 mm diameter stirrups with a spacing of 8 mm was selected. Consequently, whereas a correct scaling of the confinement effect is respected, the shear strength is slightly underestimated, but considered acceptable for the test campaign. The total shear strength can be calculated according to (Priestley & Verma, 1997).

$$V_t = V_c + V_s + V_p \tag{6.1}$$

$$V_c = k\sqrt{f_c}\,0.8A_c \tag{6.2}$$

$$V_s = \left(\frac{A_{sw}}{s_s}\right)f_y D cot\theta + \frac{sin\beta A_{sp}}{s_p}f_y D\ (cot\theta + cot\beta) \tag{6.3}$$

$$V_p = Ptan\alpha \tag{6.4}$$

where k is a curvature ductility-dependent coefficient, fc is the compressive concrete strength, f_y is the steel strength, Ac is the cross section area, Asw is the stirrups area and Asp is the area of inclined rebars (with angle β) and spacing s_s and sp respectively. P is the normal force and α is the angle of inclination of the ideal line connecting the normal forces at top and bottom of the element. D is the distance between rebars at the top and bottom of the section. For example, the shear strength of pier 11 assuming *k=0.2*, corresponding to a ductility of 3, *fc=26 MPa,*

fy=350 MPa, s$_s$=20 cm, sp=114 and *θ=45°* cm, leads to *Vc=390 kN, Vs=520 kN.*

Because *P=0* approximately, the total strength of the transverse beam of pier 11 is *V$_t$=900 kN.* Consequently, a correct reduced scale model should have a shear strength *V$_t$=900/2.5^2 = 144 kN,* obtained using stirrups with a diameter of 3.2 mm. Since the closest diameter available on the market is 3, then even if the confinement effect is respected, given that the spacing was correctly scaled, the actual strength of the scaled model is *V$_s$=81.6 kN.* The approximation can be considered acceptable.

6.1.3. Scaling of the bond slip phenomenon

More delicate is the scaling effect on concrete-steel bond conditions. Past experimental tests have shown that scaling may have a relevant influence on the bond of deformed bars, especially in terms of slippage and crack propagation (Ichinose et al. 2004). In the case of plain steel bars, its influence can still be considered significant (Pinto & Mancini, 2009, Bazant et al. 1988). However, since experimental evidence has demonstrated that in this case the anchorage effect of hooks prevails (Fabbrocino et al. 2005), the adopted geometrical scaling can be accepted.

According to the scaling effect described in the previous paragraphs the specimens were designed by Roma Tre. For example, in (Fig. 6.1) the reinforcement of the cap-beam and of a transverse beam of pier 9 is shown. The full drawings of both the mock-ups are presented in AppendixC.
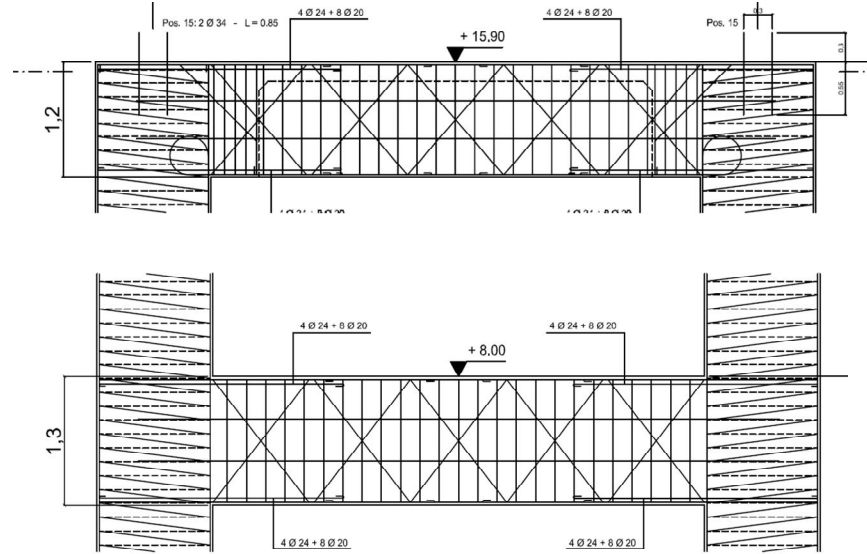
Figure 6.1 Reinforcement of cap and transverse beam and of the tall pier

6.1.4. Scaling of the FP devices

According to (De Risi & Di Sarno, 2011), the full scale model of FP isolators designed according to displacement-based design should have a Radius R=3000 mm and a friction coefficient equal to 4%. The permanent loads axial force is approximately 7500 kN, whereas the seismic axial force is about 2800 kN. The constitutive law corresponding to the above parameters is therefore the following (Fig. 6.2):
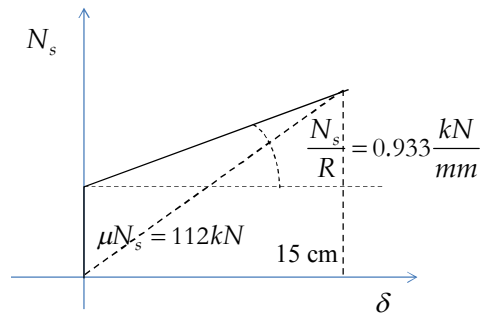
Figure 6.2 Constitutive low relationships

The effective stiffness corresponding to a displacement level of 15 cm is:

$$K_{eff} = \frac{N}{R} + \frac{\mu N}{D} = \frac{2800}{3000} + \frac{0.04 \times 2800}{150} = 1.68\ kN/mm \tag{6.5}$$

Consequently the effective period is equal to

$$T_{eff} = 2\pi \sqrt{\frac{m}{K_{eff}}} = 2\pi \sqrt{\frac{N}{gK_{eff}}} = 2\pi \sqrt{\frac{2800}{9810 \times 1.68}} = 2.58\ sec \tag{6.6}$$
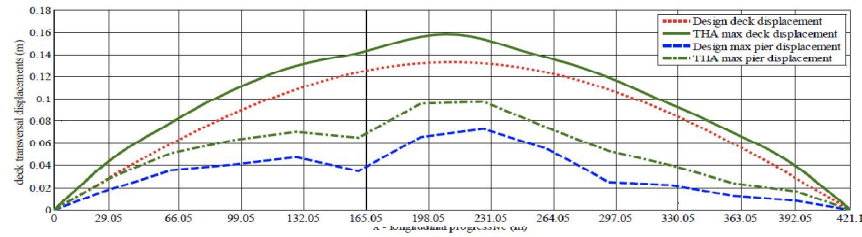
Figure 6.3 Maximum deck displacements

In (Fig. 6.3) is shown the performance of the viaduct in terms of displacement based on non-linear dynamic analyses on a refined model as shown in (De Risi & Di Sarno, 2011). The mode of failure of the piers is mainly given by shear failure of the transverse beams.

In order to respect the similitude requirements, the 1:2.5 reduced scale model of FP isolators should have the following characteristics:

Radius: $R=3000 /2.5 = 1200$ mm
Friction coefficient: $\mu=4\%$

In fact, the equivalent stiffness and the effective period becomes respectively

$K_{eff}=0.672\ kN/m$ and

$T_{eff}=1.63\ sec.$

6.2. Geometry and detailing of the pier mock up's

In the test campaign, two specimens of the piers of the Rio-Torto viaduct were constructed and tested experimentally with the PsD testing technique. The first specimen, related to pier 11; is a 2 level 1-bay pier with a total height (including the base) of 700 cm. The second specimen, related to pier 9, is a 3 level 1-bay pier with a total height of 1150 cm. The base of both piers is rectangular, 600 cm long and 280 m wide (Fig. 6.4 and Fig. 6.5). The full drawings and steel detailing could be found on Appendix (C).
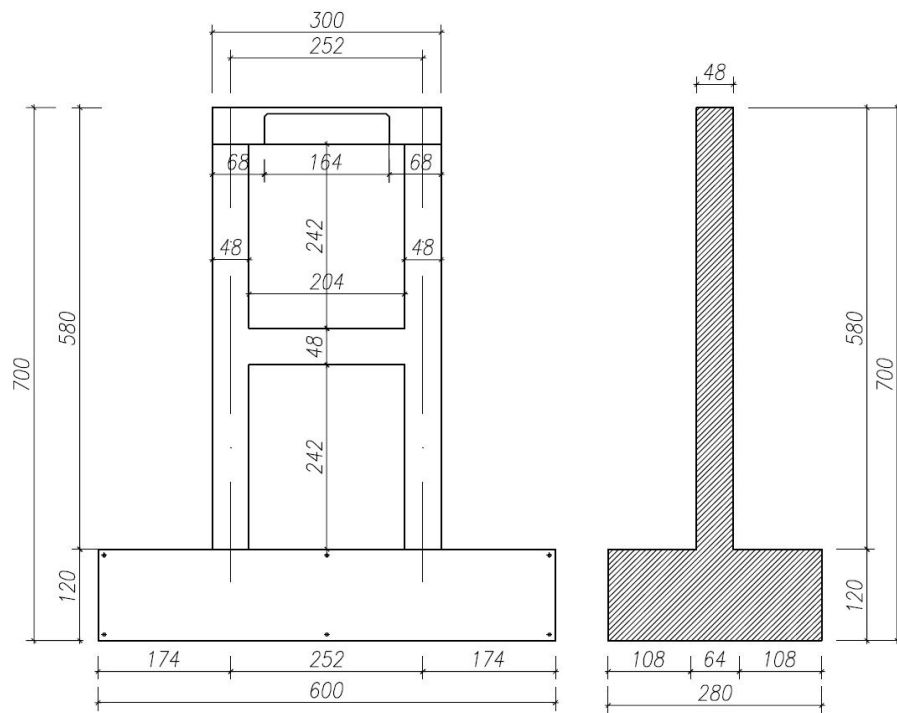
Figure 6.4 Geometry of pier 11

Figure 6.5 Geometry of pier 9

6.3. Gravity loads

The vertical load on the piers is the result of a combination of the load applied by the actuators and the self-weight load of the testing rig elements as indicated in Table 6.2 and Table 6.3.

Table 6.2 Gravity load on the Pier 9 by different elements

Loading frame (1)	1842 kg
Vertical actuators (2)	552 kg
Horizontal actuators (½×2)	1097 kg
Load Cell (2)	127 kg
Total	**3618 kg**

Table 6.3 Gravity load on the Pier 11 by different elements

Loading frame (1)	1702 kg
Vertical actuators (2)	552 kg
Horizontal actuators (½×2)	1097 kg
Load Cell (2)	127 kg
Total	

6.4. Scaled isolation system setting up

Below is shown the test setup regarding the isolation mock-ups. There is a first steel plate fixed at the strong floor of the lab on which are located the first two devices. For these two isolators the sliding surface is pointing upwards. On these two devices is located a second steel plate, linked to the horizontal actuator, that is free to move horizontally along the transverse direction of the bridge. On the top face of this plate are located the other two isolation devices, whose sliding surfaces are pointing downwards. These two devices host another steel plate loaded by the axial load generated by four vertical actuators.

The four vertical actuators are controlled trough a feedback system allowing the steel plates to move horizontally; the above system can also accommodate the vertical displacements of the plates due to sliding of the curved surface of the devices.

A fixed vertical load resulting from the self-weight of the testing rig, load cells and actuators acts on the devices and is computed as follows: middle plate (7.6 kN), top plate (22.6 kN), four vertical actuators (4 x 2.7 = 10.83kN), four load cells related to the vertical jacks (4 x 0.7 = 2.75 kN) and half of the horizontal actuator along with the connecting flange ((7.7+0.6)/2 = 4.5 kN), for a total load of 48.2 kN, about 50 kN considering also the isolators and other small components (bolts, the tubes, etc). For this reason, in the numerical analysis for the calibration of the devices mechanical properties, this value will be accounted for by adding it to the axial load applied through the vertical jacks.

The design mechanical properties of the devices are a curvature radius R equal to 3000 mm and a friction coefficient μ_f equal to 4%. Considering that the scale factor S equal to 2.5 employed for the experimental tests, the mock up's properties are R and μ_f equal to 1200 mm and 4%, respectively.
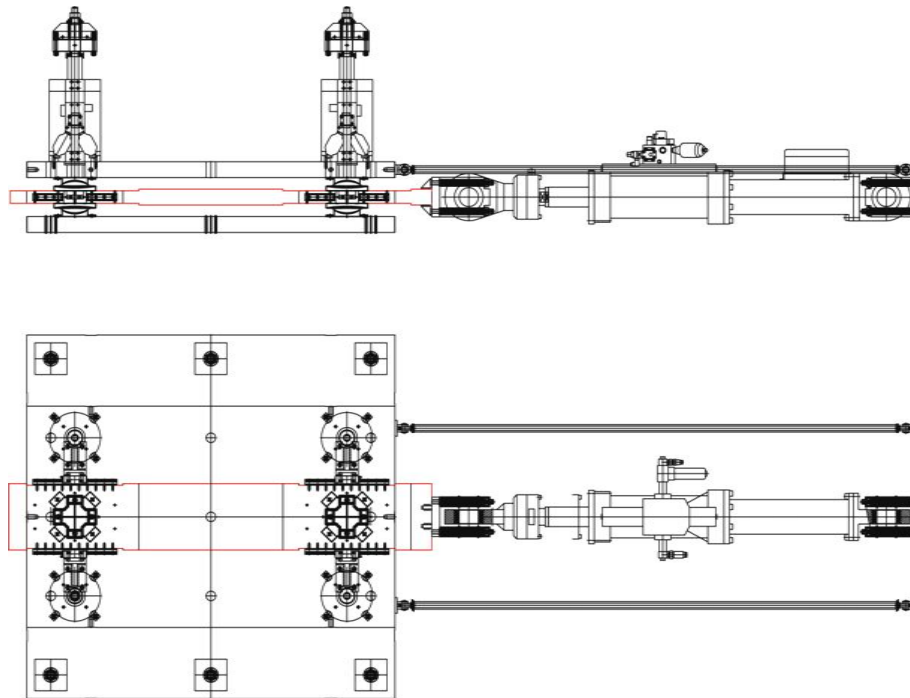
Figure 6.6 Isolation devices test setup

6.5. Materials mechanical properties of the piers

To fully characterize the concrete of the two piers, a series of compression tests were performed at JRC using 15×15×15 cm cube specimens. The aggregate design mix of concrete was performed using a maximum aggregate dimension of 3 cm, in order to have short-term properties compatible with the expected behaviour of the piers. The average value of the cubic strength obtained is about 41 MPa and

consequently a cylindrical strength of about 34 MPa. This value is in line with the strength value of the concrete used for the construction of the real piers.
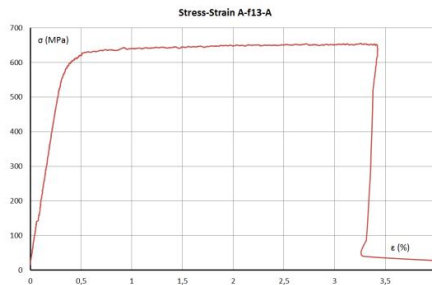
Figure 6.7 Stress-Strain behaviour of test A-fi3-A for plain 3mm steel bar
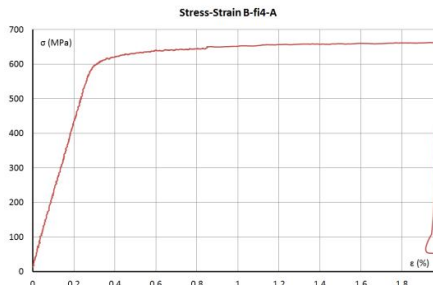
Figure 6.8 Stress-Strain behaviour of test A-fi4-A for plain 4mm steel bar
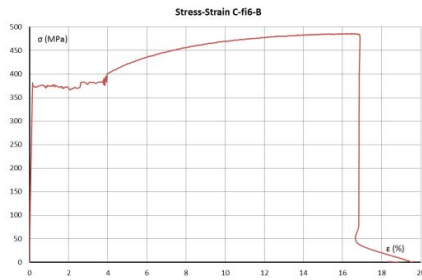
Figure 6.9 Stress-Strain behaviour of test C-fi6-B for plain 6mm steel bar
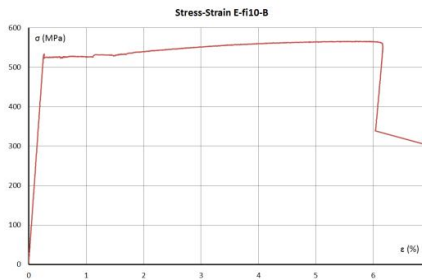
Figure 6.10 Stress-Strain behaviour of test E-fi10-B for plain 10mm steel bar

The class of the steel reinforcement used for the construction is not known. Since at that time AQ42 steel was commonly used in Italy, corresponding to a mean strength of 350 MPa (Verderame & Stella, 2001), this value was adopted for design strength of the steel bars of the specimens. This consists of smooth rebars of diameter 3, 4, 8 and 10 mm, on which direct tensile tests for the evaluation of the constitutive law of steel were carried out, obtaining an average value of 350 MPa. (Fig. 6.7 - 6.10) show examples of stress-strain curves.

The bond mechanism of straight steel bars and bars with circular hooks was characterized by pull-out tests within an experimental campaign carried out at the University Roma Tre (Paolacci & Gennini, 2012). This is discussed previously in section 3.4.

6.6. Testing Methods

Although the Pseudo-Dynamic (PsD) test method not the main topic of this thesis, it is important to give an overview about to more clarify the method used for experimental tests.

The Pseudo-Dynamic (PsD) test method combines the numerical time integration of the equations of motion of a structure, properly condensed on a limited number of degrees-of-freedom (DoF), and the experimental measurement of the reaction forces resulting from this motion, applied by means of actuators. This hybrid analytical/experimental character is taken into account when introducing the subtructuring technique (Dermitzakis & Mahin, 1985), allowing to obtain the dynamic response of a structure with only a part, usually the most vulnerable one, present in the laboratory.

The European Laboratory for Structural Assessment (ELSA) laboratory has been involved from some years in the development of the continuous PsD testing method (Magonette et al. 2001), consisting of a PsD test with no hold period that avoids the load relaxation problem and increases the signal/noise ratio, and consequently improving the quality of the results. It allows also a considerable reduction of the test duration and provides much cleaner measurements.

This testing method, which is nowadays the only one used at ELSA, was implemented by means of a synchronous process with a short control period (2ms) and a small time step for the time integration.

Within this framework, it is straightforward to add some DoFs in the process of controlling the structure, providing that the total number of DoFs remains small and the numerical structure elastic. This *monolithic* approach cannot be followed when the number of DoFs increases or when the numerical structure is nonlinear, as for RETRO. In this case *two* processes should be ran in parallel, the first one responsible for the numerical structure and the other one responsible for the motion of the physical structure in the lab, preserving the smooth character of the continuous method. These two processes, should have *different time steps* (It is virtually impossible to ensure that, within the effective clock duration - 2ms - of one laboratory time step, the analytical process is able to successively perform all the tasks required for advancing its solution, in particular when non-linearities are present). It should also use *different time integration schemes* (conditional stability of the laboratory explicit central difference scheme is easy to fulfill, but the numerical structure should use an implicit scheme, to manage the larger time step and the larger number of DoFs).

Starting from the domain decomposition scheme presented in (Gravouil & Combescure, 2001), it was shown that it is possible to transform this essentially staggered asynchronous procedure in an inter-field parallel procedure suitable to work with one synchronous process, keeping most of the original characteristics of the scheme (Pegon & Magonette, 2002). The non-linear case was also investigated and a combination of a non-iterative Operator Splitting strategy (Nakashima et al. 1993, Combescure & Pegon, 1997), and of a non-linear condensation technique was proposed to handle the analytical structure (Pegon & Magonette, 2005). This distributed scheme, including experimental results obtained in 2005 when testing an isolator is described in detail in (Pegon et al. 2008, Bonelli & Bursi, 2008).

For the RETRO project, the research implementation performed for the validation tests of 2005 was insufficient. RETRO includes a much larger specimen, some of them (the piers) accumulating damage in an

irreversible way. It was thus needed to substantially upgrade the substructuring implementation of 2005, in order to have during the tests the same standards for error and alarm management, the same input (plus the additional requested information specific of substructuring), the same output definition (adding few substructuring related variables) as what is the current state-of-the art in continuous PsD testing at ELSA.

As with all substructured tests performed in the past at ELSA, the software used for the numerical part is Cast3M (Millard et al. 1993), a multi-purpose finite element code which was also slightly modified in order to introduce the non-linear models used during the tests.

6.7. Setting Up and Instrumentation

6.7.1. Testing rig

To load the piers model in the laboratory a steel frame was designed to simulate the effect and load transfer of the bridge deck. At the same time the loading frame provided anchorage points for actuators, two for horizontal and two for vertical loading at each pier.

Figure 6.11 shows the two piers as they were installed at ELSA. At the top of each of the piers the loading frame is secured with bolts anchored in the piers' concrete beams. The loading frame (Fig. 6.12 and. 6.13) provides about "0.80 m" lever arm for the horizontal actuators applying horizontal displacements and measuring forces during testing.

Actuators installed (rendered blue in Fig. 6.11) at the top of every pier's column applied vertical load by tensioning a Dywidag bar passing through piers and being anchored at the footing. Vertical load was applied to the piers before the start of the PsD test.

For each of the two piers there was also a seismic isolator set-up installed. It was positioned on the strong floor in front of the piers using their

footing as a support for the horizontal actuators. Seismic actuators were mounted on a strong steel plate with a middle plate on top of them. Then another set of isolators, turned upside down, was mounted on the middle plate with another steel plate on top of them. The bottom steel plate was bolted to the strong floor of the laboratory. The middle steel plate was connected to an actuator which applied horizontal displacements during the tests. The top steel plate was braced with two beams that blocked horizontal displacements while allowing vertical displacements so that the isolators could work properly. The vertical load was applied by four actuators installed on the top plate by pulling a bar fixed at the bottom plate. Drawings of the isolator set-up are shown in (Fig. 6.14 and 6.15).
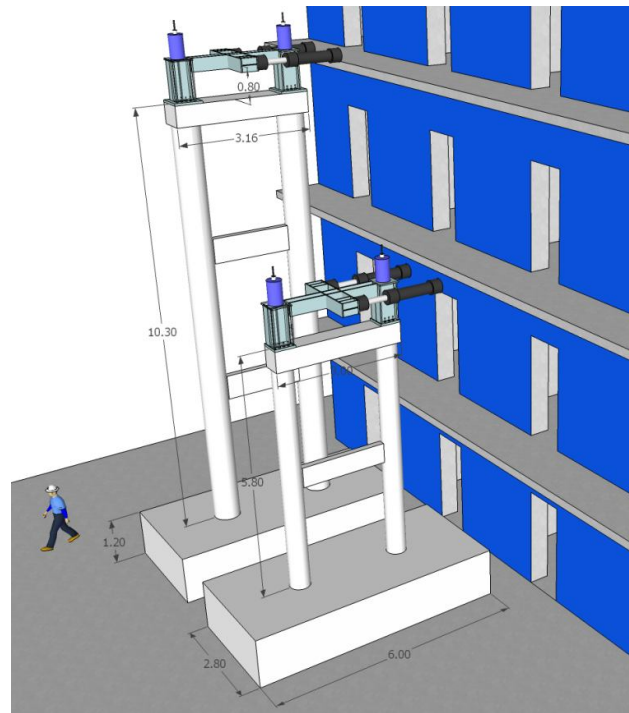
Figure 6.11 Mock-up of the RETRO piers in ELSA

Figure 6.12 Loading frame of Pier 9

Figure 6.13 Loading frame of Pier 11

Figure 6.14 Cross section of the isolator set-up
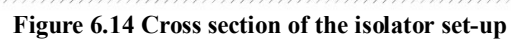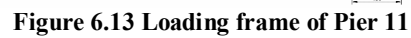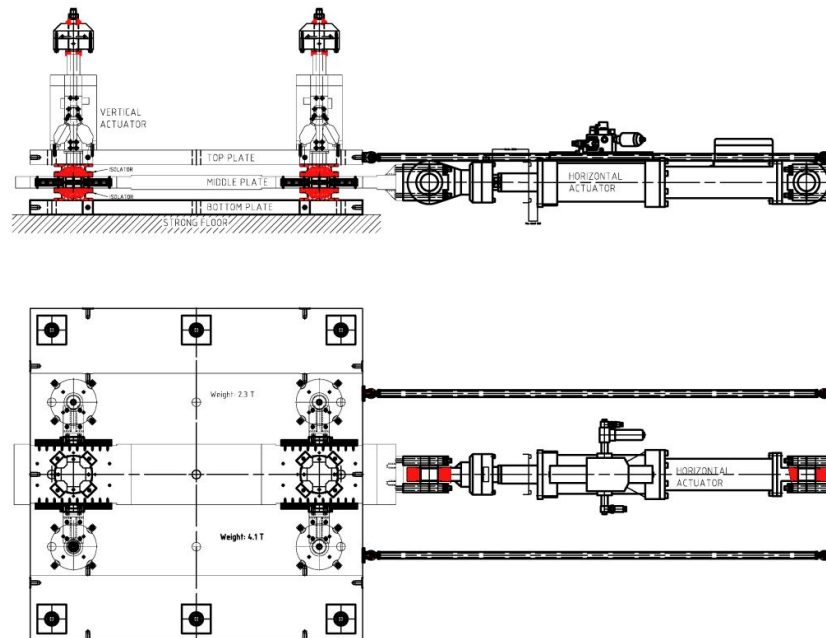
Figure 6.15 Top and side view of the isolator set-up

6.7.2. Control Strategy

The test setup consisted of 18 actuators (see Fig. 6.16 – 6.18). At ELSA, every actuator has associated typically a TEMPOSONICS displacement transducer, measuring the displacement of the piston with respect to the cylinder, a load cell, measuring its applied axial force and some other sensors for the oil pressure at the chambers and for the servo-valve spool displacement. For this setup, the horizontal actuators also had a HEIDENHAIN displacement transducer measuring the displacement at a point of the specimen with respect to a fixed reference frame. These measurements, as well as the reference target and the servo-valve command are dealt, for every actuator, by a SLAVE controller, which is also in charge of the PID algorithm to compute the servo-valve command. A number, of up to four SLAVE controllers, are connected to a MASTER controller that exchanges all signals at the controller with a sampling period of 2ms within the ELSA testing system (Pegon & Molina, 2008).

The MASTER controller uses a DLL program that, by interacting with all those signals relative to the SLAVE controllers, is able to manage different kinds of tests, such as cyclic, monolithic PsD (with all the analytical substructure inside of the MASTER DLL) or distributed PsD (with the analytical substructure running in a separate computer network).
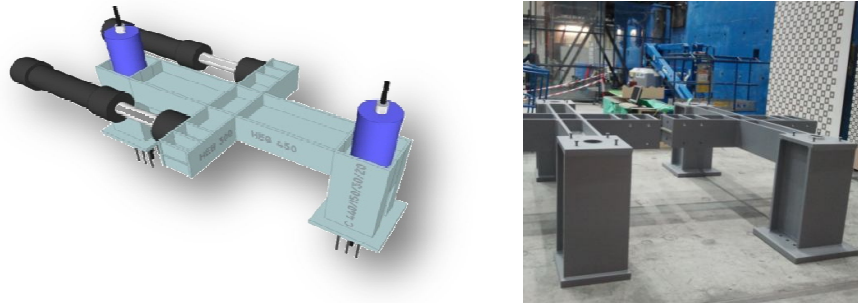
Figure 6.16 (a) Horizontal actuators used in ELSA Lab; (b) Steel frame used to connect the actuators to the piers
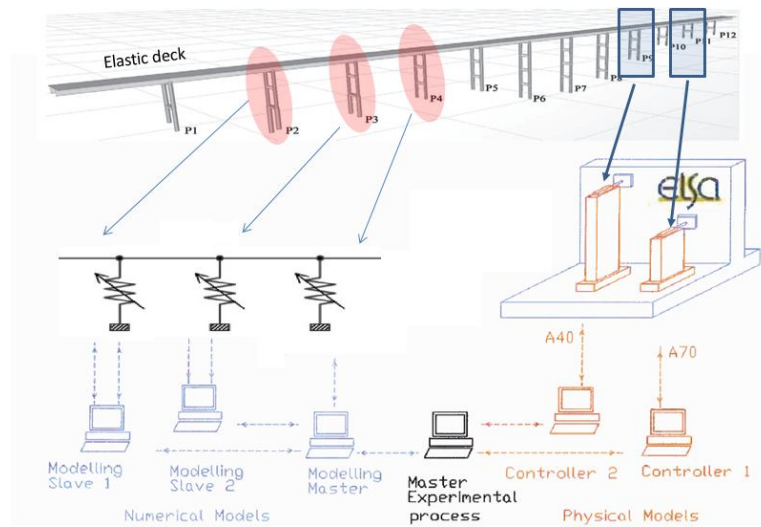
Figure 6.17 PsD test setting up
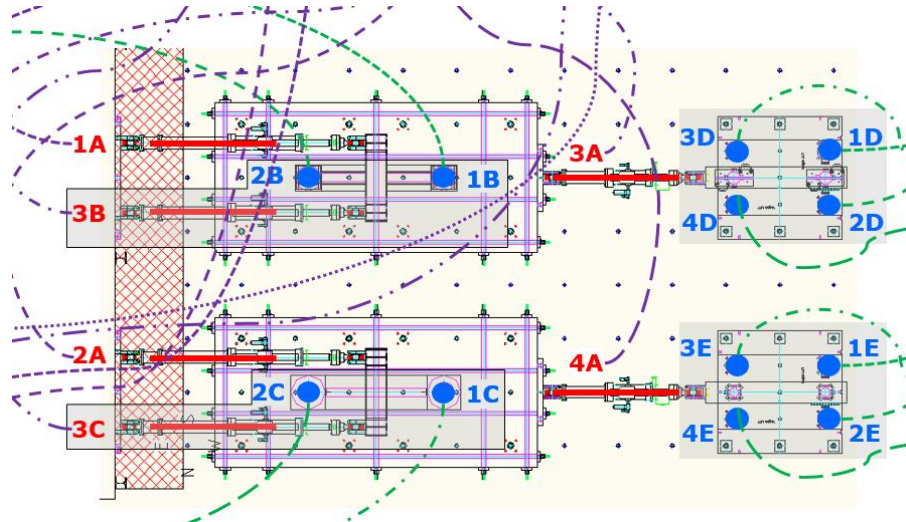
Figure 6.18 Actuator map setting up

6.7.3. Piers control

In order to introduce the gravity load coming from the deck, not present physically in the laboratory, every pier was loaded by two vertical actuators, one at the West column and one at the East column of the pier. The East column of the pier was the closest one to the reaction wall.

These vertical actuators were always used in force control with a constant specified target force of -450 kN during the tests in which they were used. The force was measured by a load cell between the piston and the end nut of the DIWIDAG bar. This steel bar was passing through the load cell and the piston, going inside of the column and fixed at the bottom of the foundation. At the beginning of the test, the target force was increased by a cosine function growing from zero up to the specified value. In the case of the seismic tests, the initial phase of gradual increase of the vertical load has negative time abscissa and the earthquake phase starts at zero time.

Once the pier had the constant vertical load applied by the vertical actuators, two horizontal actuators working in displacement control imposed the cyclic or PsD target, so that the translation was imposed without any torsion. The transducer used as feedback for these actuators was a digital optical HEIDENHAIN encoder measuring the movement of the upper steel loading rig in the axis of the actuator and with respect to the reference frame resting on the strong floor. For every pier, the SLAVE controller for the South (closer to the controllers) horizontal actuator received its digital target from MASTER A, which was the only MASTER used for running a PsD method through its DLL, whereas the North horizontal actuator had its SLAVE belonging to a different MASTER. The signal of the target for the North actuator was communicated in analogue form between the affected MASTER controllers. In a similar manner, for the PsD tests, the force applied by the North actuator was communicated back to MASTER A as an analogue signal so that it could be computed in the restoring force within the equation of motion together with the force applied by the South actuator.

6.7.4. Control of isolators

Each isolator setup had four vertical actuators positioned at the corners of the upper rectangular plate and numbered 1…4. Actuators 1 (South-West) and 2 (North-West) applied a total specified force:

$$F_{WEST} = F_1 + F_2 \tag{6.7}$$

With centre on the West column of isolators. Actuators 3 (South-East) and 4 (North-East) applied a total specified force

$$F_{EAST} = F_3 + F_4 \tag{6.8}$$

With centre on the East column of isolators, the control of the four actuators was based on the imposition of Eq. 6.7 and Eq. 6.8 plus two additional constraints. The rolling rotation was imposed to be null, or

138

equivalently, by using the TEMPOSONICS displacements of the four pistons with respect to the cylinders:

$$T_1 - T_2 + T_3 - T_4 = 0 \qquad (6.9)$$

And, finally, warping was controlled by imposing null warping moment, $M_\omega = 0$, or equivalently:

$$F_1 - F_2 - F_3 + F_4 = 0 \qquad (6.10)$$

Equations 6.7 through 6.10 are equivalent to the set of constraints:

$$
\begin{aligned}
F_1 &= F_{WEST} - F_2 \\
F_2 &= F_1 - F_3 + F_4 \\
F_3 &= F_{EAST} - F_4 \\
T_4 &= T_1 - T_2 + T_3
\end{aligned} \qquad (6.11)
$$

In practice, the constraints were imposed by controlling three actuators with feedback in force (F_1, F_2 and F_3) and the last one with feedback in displacement (T_4). The standard formula for the control error as input to the PID control algorithm

$$e=\{Target\}-\{Feedback\} \qquad (6.12)$$

$$
\begin{aligned}
e_1 &= \{F_{WEST}-F_2\}-\{F_1\} \\
e_2 &= \{F_1-F_3+F_4\}-\{F_2\} \\
e_3 &= \{F_{EAST}-F_4\}-\{F_3\} \\
e_4 &= \{T_1-T_2+T_3\}-\{T_4\}
\end{aligned} \qquad (6.13)
$$

For the four vertical actuators, the value of the four targets, as defined by Eq. 6.13, was computed by the MASTER controller associated to these

four actuators. Depending on the kind of test, F_{WEST} and F_{EAST} had a constant value of -450 kN or varied with an addition term, according to either a specified random history or a proportion of the pitching moment introduced by the horizontal actuators of the respective pier. In fact, the value of the force applied by the horizontal actuators of the respective pier was communicated to this MASTER by analogue signals. The initial phase of gradual increase of the vertical forces from zero to -450 kN was done with a cosine history and simultaneously for the piers and isolators.

Every isolator setup had a horizontal actuator for imposing the same deformation on the four isolators through the guided medial beam. This actuator was used in displacement control by using a HEIDENHAIN encoder measuring the displacement of that beam with respect to the strong floor. The SLAVE of this actuator belonged to MASTER A, which was communicating the target to it as computed from the equation of motion in the PsD tests, including the isolator specimens.

6.8. Sensors and acquisition system

In the transverse section of the pier, a number of LVDT sensors were installed in order to measure local deformation and global displacements. Figure 6.19 shows three wire sensors on pier 9 to measure global displacement at each level of the transverse beams, together with 74 sensors installed in different levels above the column base, lower and upper beam-column joints and in the transverse beams. Each transverse beam was divided into four parts; each part with one diagonal, right, left, upper and lower sensors, as shown in (Fig. 6.20)
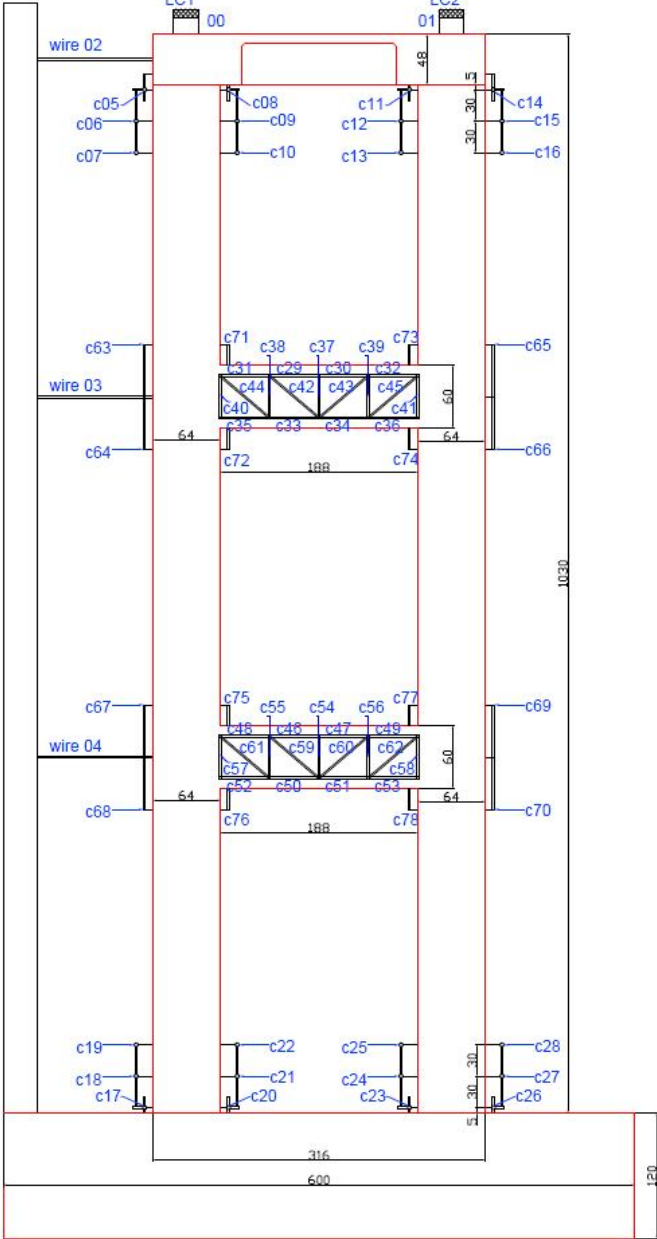
Figure 6.19 LVDT sensors map of pier 9 tests

Figure 6.20 LVDT sensors on the transverse beam

Table 6.4 shows the number, position, length and name of each sensor on pier 9

Table 6.4 LVDT sensors table for pier 9

Channel #	Length	Typology	Name	Channel #	Length	Typology	Name	Channel #	Length	Typology	Name
00		LC 1	cover A	20	25,00	LVDT 50 mm	Lo_lx_rx2	40	34,00	LVDT 50 mm	L1_co_rx2
01		LC 2	cover B	21	25,00	LVDT 50 mm	Lo_lx_rx3	41	61,30	LVDT 50 mm	L1_di_lx1
02		Wire s.	top. wire	22	05,00	LVDT 50 mm	Lo_rx_lx1	42	61,30	LVDT 50 mm	L1_di_rx1
03		Wire s.	mid. wire	23	25,00	LVDT 50 mm	Lo_rx_lx2	43	61,30	LVDT 50 mm	L1_di_lx2
04	15,00	LVDT 50 mm	L2_lx_lx1	24	25,00	LVDT 50 mm	Lo_rx_lx3	44	61,30	LVDT 50 mm	L1_di_rx2
05	25,00	LVDT 50 mm	L2_lx_lx2	25	05,00	LVDT 50 mm	Lo_rx_rx1	45	44,00	LVDT 50 mm	L1_ou_lt
06	25,00	LVDT 50 mm	L2_lx_lx3	26	25,00	LVDT 50 mm	Lo_rx_rx2	46	44,00	LVDT 50 mm	L1_ou_lb
07	05,00	LVDT 50 mm	L2_lx_rx1	27	25,00	LVDT 50 mm	Lo_rx_rx3	47	44,00	LVDT 50 mm	L1_ou_rt
08	25,00	LVDT 50 mm	L2_lx_rx2	28	51,00	LVDT 50 mm	L1_tp_lx1	48	44,00	LVDT 50 mm	L1_ou_rb
09	25,00	LVDT 50 mm	L2_lx_rx3	29	51,00	LVDT 50 mm	L1_tp_rx1	49	20,00	LVDT 50 mm	L1_in_lt
10	05,00	LVDT 50 mm	L2_rx_lx1	30	51,00	LVDT 50 mm	L1_tp_lx2	50	20,00	LVDT 50 mm	L1_in_lb
11	25,00	LVDT 50 mm	L2_rx_lx2	31	51,00	LVDT 50 mm	L1_tp_rx2	51	20,00	LVDT 50 mm	L1_in_rt
12	25,00	LVDT 50 mm	L2_rx_lx3	32	51,00	LVDT 50 mm	L1_bt_lx1	52	20,00	LVDT 50 mm	L1_in_rb
13	15,00	LVDT 50 mm	L2_rx_rx1	33	51,00	LVDT 50 mm	L1_bt_rx1				
14	25,00	LVDT 50 mm	L2_rx_rx2	34	51,00	LVDT 50 mm	L1_bt_lx2				
15	25,00	LVDT 50 mm	L2_rx_rx3	35	51,00	LVDT 50 mm	L1_bt_rx2				
16	05,00	LVDT 50 mm	Lo_lx_lx1	36	34,00	LVDT 50 mm	L1_co_m				
17	25,00	LVDT 50 mm	Lo_lx_lx2	37	34,00	LVDT 50 mm	L1_co_lx1				
18	25,00	LVDT 50 mm	Lo_lx_lx3	38	34,00	LVDT 50 mm	L1_co_rx1				
19	05,00	LVDT 50 mm	Lo_lx_rx1	39	34,00	LVDT 50 mm	L1_co_lx2				

A similar sensor map was prepared for Pier 11. Figure 6.21 shows two wire sensors to measure the global displacement at each level corresponding to the transverse beams, and 49 sensors installed in different locations to measure local deformations. Table 6.5 shows the sensors map of pier 11.

Figure 6.21 LVDT sensors map of pier 11 tests
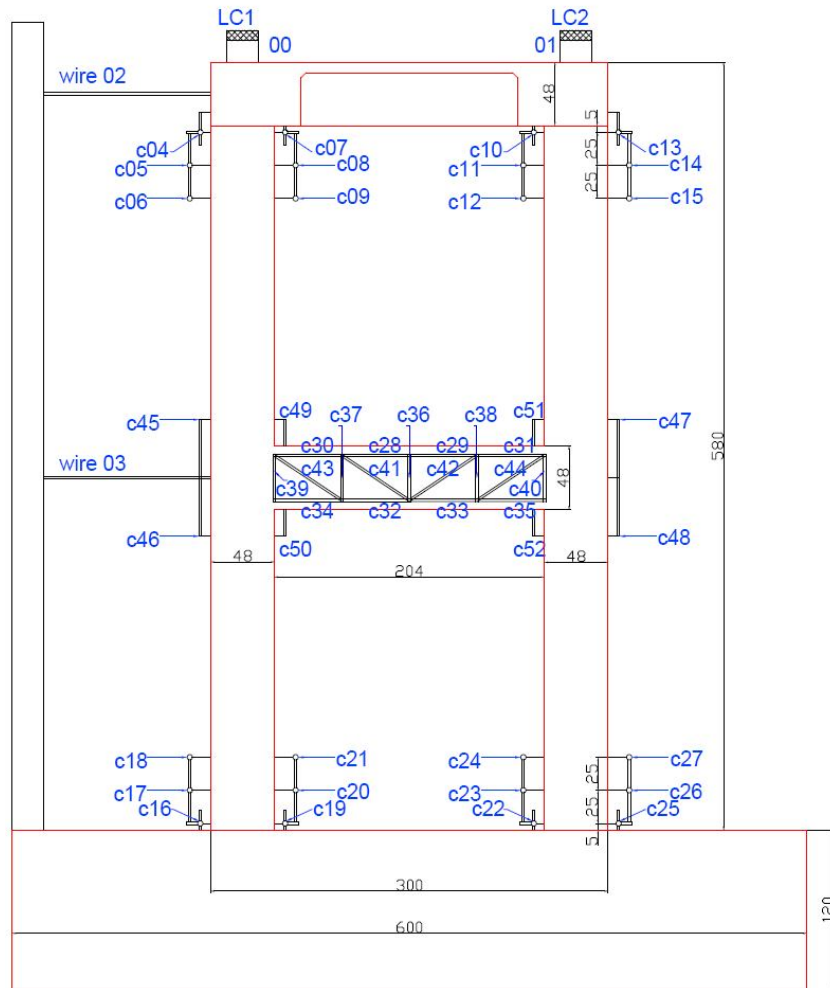
Table 6.5 LVDT sensors table for pier 11

Channel #	Length	Typology	Name	Channel #	Length	Typology	Name	Channel #	Length	Typology	Name	Channel #	Length	Typology	Name
00		LC 1	cover A	20	05,00	LVDT 50 mm	Lo_lx_rx1	40	40,00	LVDT 50 mm	L2_co_lx2	60	61,70	LVDT 50 mm	L1_di_rx1
01		LC 2	cover B	21	30,00	LVDT 50 mm	Lo_lx_rx2	41	40,00	LVDT 50 mm	L2_co_rx2	61	61,70	LVDT 50 mm	L1_di_lx2
02		Wire s.	lev3. wire	22	30,00	LVDT 50 mm	Lo_lx_rx3	42	61,70	LVDT 50 mm	L2_di_lx1	62	61,70	LVDT 50 mm	L1_di_rx2
03		Wire s.	lev2. wire	23	05,00	LVDT 50 mm	Lo_rx_lx1	43	61,70	LVDT 50 mm	L2_di_rx1	63	44,00	LVDT 50 mm	L1_ou_lt
04		Wire s.	lev1. wire	24	30,00	LVDT 50 mm	Lo_rx_lx2	44	61,70	LVDT 50 mm	L2_di_lx2	64	44,00	LVDT 50 mm	L1_ou_lb
05	15,00	LVDT 50 mm	L3_lx_lx1	25	30,00	LVDT 50 mm	Lo_rx_lx3	45	61,70	LVDT 50 mm	L2_di_rx2	65	44,00	LVDT 50 mm	L1_ou_rt
06	30,00	LVDT 50 mm	L3_lx_lx2	26	05,00	LVDT 50 mm	Lo_rx_rx1	46	47,00	LVDT 50 mm	L1_tp_lx1	66	44,00	LVDT 50 mm	L1_ou_rb
07	30,00	LVDT 50 mm	L3_lx_lx3	27	30,00	LVDT 50 mm	Lo_rx_rx2	47	47,00	LVDT 50 mm	L1_tp_rx1	67	20,00	LVDT 50 mm	L1_in_lt
08	05,00	LVDT 50 mm	L3_lx_rx1	28	30,00	LVDT 50 mm	Lo_rx_rx3	48	47,00	LVDT 50 mm	L1_tp_lx2	68	20,00	LVDT 50 mm	L1_in_lb
09	30,00	LVDT 50 mm	L3_lx_rx2	29	47,00	LVDT 50 mm	L2_tp_lx1	49	47,00	LVDT 50 mm	L1_tp_rx2	69	20,00	LVDT 50 mm	L1_in_rt
10	30,00	LVDT 50 mm	L3_lx_rx3	30	47,00	LVDT 50 mm	L2_tp_rx1	50	47,00	LVDT 50 mm	L1_bt_lx1	70	20,00	LVDT 50 mm	L1_in_rb
11	05,00	LVDT 50 mm	L3_rx_lx1	31	47,00	LVDT 50 mm	L2_tp_lx2	51	47,00	LVDT 50 mm	L1_bt_rx1	71	44,00	LVDT 50 mm	L1_di_lx2
12	30,00	LVDT 50 mm	L3_rx_lx2	32	47,00	LVDT 50 mm	L2_tp_rx2	52	47,00	LVDT 50 mm	L1_bt_lx2	72	44,00	LVDT 50 mm	L1_ou_lb
13	30,00	LVDT 50 mm	L3_rx_lx3	33	47,00	LVDT 50 mm	L2_bt_lx1	53	47,00	LVDT 50 mm	L1_bt_rx2	73	44,00	LVDT 50 mm	L1_ou_rt
14	15,00	LVDT 50 mm	L3_rx_rx1	34	47,00	LVDT 50 mm	L2_bt_rx1	54	40,00	LVDT 50 mm	L1_co_m	74	44,00	LVDT 50 mm	L1_ou_rb
15	30,00	LVDT 50 mm	L3_rx_rx2	35	47,00	LVDT 50 mm	L2_bt_lx2	55	40,00	LVDT 50 mm	L1_co_lx1	75	20,00	LVDT 50 mm	L1_in_lt
16	30,00	LVDT 50 mm	L3_rx_rx3	36	47,00	LVDT 50 mm	L2_bt_rx2	56	40,00	LVDT 50 mm	L1_co_rx1	76	20,00	LVDT 50 mm	L1_in_lb
17	05,00	LVDT 50 mm	Lo_lx_lx1	37	40,00	LVDT 50 mm	L2_co_m	57	40,00	LVDT 50 mm	L1_co_lx2	77	20,00	LVDT 50 mm	L1_in_rt
18	30,00	LVDT 50 mm	Lo_lx_lx2	38	40,00	LVDT 50 mm	L2_co_lx1	58	40,00	LVDT 50 mm	L1_co_rx2	78	20,00	LVDT 50 mm	L1_in_rb
19	30,00	LVDT 50 mm	Lo_lx_lx3	39	40,00	LVDT 50 mm	L2_co_rx1	59	61,70	LVDT 50 mm	L1_di_lx1				

6.9. Reduced Model in Opensees for PSD testing

The cumbersome OpenSEES model of the Rio Torto viaduct did not comply with computational resources of the experimental equipment. Therefore, its rigorous reduction was developed for the purpose of PsD testing, and this is done by Politecnico di Torino team-work, following is the description of the model.

The dynamic substructuring approach was selected (Klerk, 2008). As a result, deck, piers isolator pairs were considered as substructures prone to be replaced by their physical counterparts.

Since higher modes of piers were not excited, the static Guyan reduction (Guyan, 1965) was successfully applied to obtain Single-Degree-of-Freedom (S-DoF) reduced piers. Each translational interface DoF between the pier and the deck was retained, whilst the remainder was discarded. The static condensation procedure is detailed in (Abbiati et al

2014). Reduced S-DoF piers were extended to the nonlinear range through Modified Bouc-Wen springs. They allowed for reproducing the hysteretic behaviour of OpenSEES piers. The resulting differential model of each pier reads,

$$m\ddot{x} + c\dot{x} + r = -f \cdot a_g\left(t\right) + g\left(t\right)$$

(6.14)

$$\dot{r} = \left[\frac{\rho \cdot A}{\left(1 + \alpha \cdot x^2\right)} - (\beta \cdot \mathrm{sgn}(\dot{x} \cdot r) + \gamma) \, | \, r \, |^n \right] \cdot \dot{x}$$

(6.15)

Where m, c and f are the linear parameters of the reduced pier obtained from the Guyan reduction, whilst ρ, A, β, γ and n are the parameters of the Modified Bouc-Wen spring. In detail, A was assumed equal to the linear stiffness of the S-DoF reduced pier, whilst ρ was introduced to represents its average degradation. γ and n parameters were assumed equal to 0 and 1, respectively. In order to replicate the softening behaviour of OpenSEES models, the softening factor α was introduced. Each single reduced S-DoF pier was considered as a stand-alone Single-Input-Single-Output (SISO) system for the purpose of the identification of its nonlinear parameters.

OpenSEES time histories were taken as reference signals. In detail, the transversal force measured at the cap beam level $g(t)$ and the seismic accelerogram $a_g(t)$ were considered as inputs, whilst the displacement response at the same location was considered as output(Abbiati et al 2014). The validation of the reduced model comparison to the refined model for Pier 9 is shown in figure (Fig. 6.22).
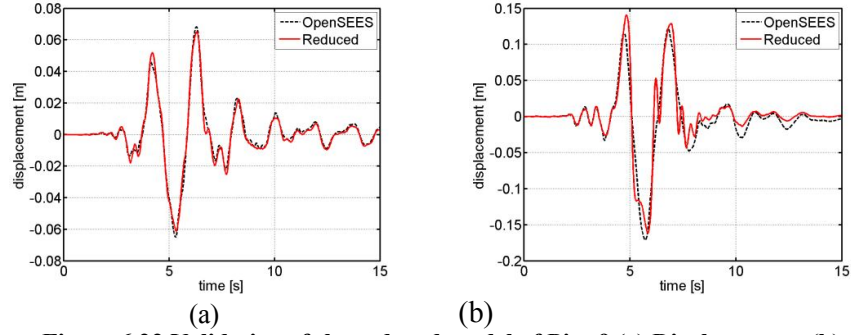
Figure 6.22 Validation of the reduced model of Pier 9 (a) Displacement, (b) Dissipated energy histories at ULS

With regard to isolator pairs, OpenSEES*single surface FP bearing* elements were substructured through the bilinear state space model proposed by (Mostaghel, 1999). Figure 6.23 depicts both a schematic of the bilinear oscillator of Mostaghel and the entailing hysteretic loop.

Figure 6.23 (a) Hysteretic loop for the bilinear system, (b) bilinear S-DoF system after Mosthagel (1999)

The system of differential equations governing the behaviour of the bilinear system depicted in (Fig.6.25) breads:

$$\begin{cases} m \cdot \ddot{x} + c \cdot \dot{x} + \alpha k x + (1-\alpha) k u = \overline{P}_0 \cdot p(t) \\ \dot{u} = \dot{x} \left(\overline{N}(\dot{x}) \overline{M}(u-\delta) + M(\dot{x}) N(u+\delta) \right) \end{cases} \qquad (6.16)$$

Where $N, M, \overline{N}$ and $\overline{M}$ are polynomials of the signum function. The state space variable u represents the slip displacement. The integration of Eq. 6.15 defines the response of any non degenerating hysteretic bilinear system under a given load.

α, δ and *k* parameters were identified with respect to OpenSEES recorded output histories considering the isolator as SISO system. Figure 6.24 compares hysteretic loops and dissipated energy histories of the right OpenSEES isolator installed on Pier #9 to its reduced counterpart at ULS.

(a)   (b)
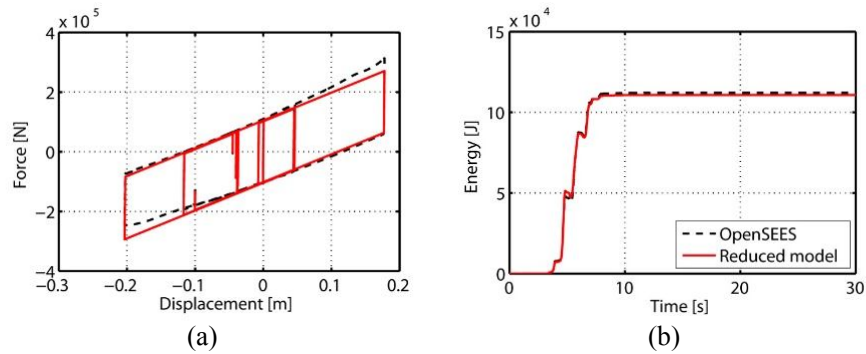
Figure 6.24 Dynamic response of right isolator of Pier 9 at ULS: a) Hysteretic loop; b) dissipated energy

Nonlinear parameters of both piers and isolator pairs were identified with the MATLAB pattern search algorithm; they can be found in (Paolacci et al 2014b). Moreover, the deck was further condensed to its transversal DoFs for testing purposes.

Reduced models of the bridge in both the non-isolated and the isolated cases were implemented by assembling substructured parts for validation purposes. Figure 6.25 shows a schematic of the reduced model of the non-isolated bridge provided with nonlinear S-DoF piers and node numbering enabled.
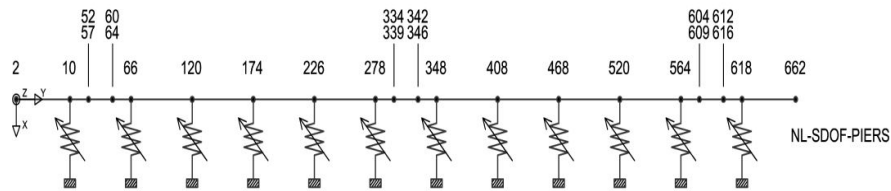
Figure 6.25 Plan view of the reduced model of the bridge in the non-isolated case

Nonlinear time history analyses at both limit states proved the effectiveness of the reduced model in reproducing the dynamic response of the OpenSEES reference. As a result sub-structured component were successfully implemented in the Cast3M FE code (Millard, 1993) as Numerical Substructures (NSs) for PsD tests at the ELSA laboratory of the Joint Research Centre of Ispra (VA), Italy. In detail, the last upgrade of the ELSA controller software embeds the parallel partitioned time integration algorithm developed by (Pegon and Magonette, 2002), i.e. the PM method. Its subcycling features allowed for interfacing and synchronizing the Cast3m FE code and the controller to perform continuous PsD testing with nonlinear NSs. Figure 6.26 compares cap beam level transversal displacement responses of Pier #9 of OpenSEES and reduced models to measure experimental response of the non-isolated bridge at both limit states (Paolacci et al. 2014b)

As can be appreciated in (Figure 6.26), experimental responses of Pier #9, which agree with predictive OpenSEES simulations, confirmed the effectiveness of tailored NSs.
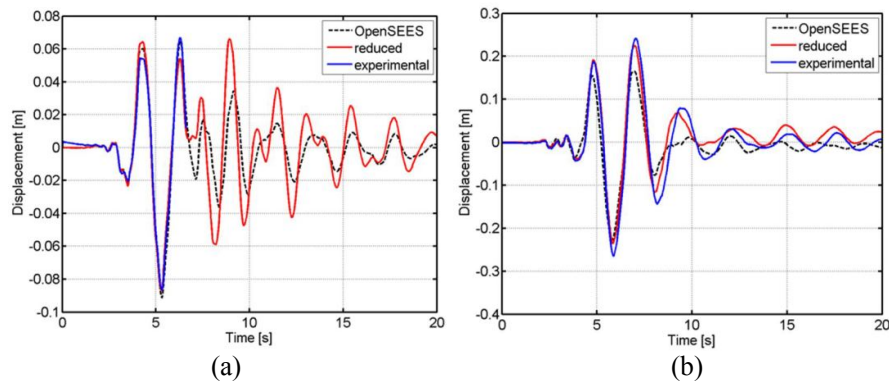
Figure 6.26 Cap beam level transversal displacement responses of Pier 9 in the non-isolated case at (a) SLS; (b) ULS

In order to simulate a consistent degradation of physical and numerical piers, a novel testing protocol was conceived and applied. It was based on recursive model identification and updating sessions aimed at propagating

damage experienced by specimens to numerical piers (Paolacci et al 2014a,b, Alessandri et al 2013). A careful description of this procedure can be found in (Abbiati et al 2014).

7. EXPERIMENTAL RESULTS

7.1. Testing program

Along the line of the PsD testing at JRC, the program was consequently subdivided in two groups of tests, one for the assessment of the seismic behaviour of the Rio-Torto viaduct and the other one for the assessment of the effectiveness of FP bearings for its seismic protection. Table 7.1 shows the most significant tests performed during the PsD test campaign.

Table 7.1 List of significant tests performed during the RETRO test campaign

Name	Description	Parameters	Type of test	Physical Part
d03	TestonIsolator_P9	V = 450 kN D = 50,40,30,20,10mm	Cyclic displacements	Isolator_P9
f03	Preliminary test for the stiffness of pier 11	V = 450 kN D=1.5 mm	Cyclic displacements	Pier 11
f04	Preliminary test for the stiffness of pier 9	V = 450 kN D=2 mm	Cyclic displacements	Pier 9
k06	Non Isolated Bridge 10% SLS	PGA=10% SLS	PsD test	Pier 9 & 11
k07	Non Isolated Bridge 100% SLS	PGA=100% SLS	PsD test	Pier 9 & 11
m01	Only physical isolators	V = 450,225,175 kN, H = 30 mm, 1.88 mm/s,	Cyclic displacements	Isolator_P9 & P11
l01	Isolated Piers case 100% SLS	PGA=100% SLS, μ=4% (design value)	PsD test	Pier 9 & 11 +Isolator_P9
l02	Isolated Piers case 100% ULS	PGA=100% ULS, μ=4% (design value)	PsD test	Pier 9 & 11 +Isolator_P9
p02	Isolated Piers case 70% ULS	PGA=70% ULS, μ=4% (design value)	PsD test	Pier 9 & 11 +Isolator_P9
k09	Not Isolated Bridge 100% ULS	PGA=100% ULS	PsD test	Pier9&11

r01	Pier 9-Isolator case 65% ULS	PGA=65% ULS μ=7% (actual value)	PsD test	Isolator_P9
r02	Pier 9-Isolator case 80% ULS	PGA=80% ULS μ=7% (actual value)	PsD test	Isolator_P9
r03	Pier 9-Isolator case 90% ULS	PGA=90% ULS μ=7% (actual value)	PsD test	Isolator_P9
k10	Aftershock - Non Isolated 100% ULS after test k09	PGA=100% ULS after a first sequence of 100%ULS (k09)	PsD test	Pier 9 & 11
k12	Aftershock - Non Isolated 200% ULS after test k10	PGA=200% ULS	PsD test	Pier 9 & 11

At the first phase of testing, the entire control system is checked, and a first characterization of the system is carried out, including the evaluation of the fundamental frequencies and the damping of the viaduct. The test was executed in a linear curve with a random signal of limited intensity level (maximum ground acceleration 0.01g).

Following the check of the control system, a set of characterization tests of the cyclic behaviour of the FP bearings provided by ALGA S.p.A. was executed (*tests d03, m01*). The tests consist of harmonic displacements with different amplitudes, frequencies and axial forces. A minimum of three values of axial forces, frequencies and amplitudes were considered, for a total of 27 tests.

A static characterization of the two piers (initial stiffness) followed with an application of cyclic displacements at the top of the models (*tests f03, f04*). This phase aimed at providing the elastic stiffness of the two piers. In particular, a monotonic static displacement, including the corresponding unloading phase, was applied to each pier and the restoring force was measured. The maximum displacements applied to piers 9 and 11 were equal 1 cm and 0.5cm, respectively.

Subsequently, a dynamic characterization of the bridge using the SLS accelerogram with a low intensity level was performed (*test k06*). The goal of this phase was to define the dynamic characteristics of the bridge

(fundamental frequency and damping). The excitation used was the East-West record of May 29th with an intensity level scaled to 0.01 g.

The first PsD test was performed on the entire bridge on the non-isolated condition, using the 100% East-West record of May 29[th](PGA=0.25g). This test (*k07*) was planned to induce slight damage on the non-isolated piers (hairline cracks on the transverse beams and at the bottom section of columns), representative of low return period earthquakes.

Afterwards, seismic tests of the isolated bridge in SLS and ULS conditions were performed (*test l01, p02*). Given that the cyclic tests on the FP bearings showed a friction coefficient of 7% greater than the designed one 4%, and that the isolators of pier 11 were working improperly, the tests were executed simulating in the numerical piers the presence of μ=4% and using only the physical isolators of pier 9 with a reduced vertical load to obtain μ=4% as well. For pier 11 the isolator was numerically simulated. The effectiveness of the FP bearings in protecting the bridge was demonstrated with the presence of (almost) a linear behaviour of physical as well as numerical piers for the SLS condition and with the presence of a limited damage condition experienced both by the physical as well as the numerical piers for the ULS condition. Since the isolator shows different behaviour than the designed one, three reduced signal tests on the physical pier 9 and physical isolator of pier 9 configuration with full vertical load were carried out. The three tests consider 65%, 80% and 90% reduction of the ULS signal, respectively. The effectiveness of the physical FP bearings in protecting the bridge were demonstrated in the different cases of reduction signals (*tests r01, r02, r03*).

Finally, to ascertain the seismic vulnerability of the non-isolated bridge a seismic test of the non-isolated bridge using the North-East record of May 29 with PGA=0.27g (ULS) was carried out (*tests k09*). In this phase, piers 9 and 11 experienced significant levels of damage (extensive crack pattern in the beams, crack opening at the base and at the top section of

the columns) as already foreseen by previous numerical simulations. The seismic test of the non-isolated case for the 100% ULS accelerogram was repeated in order to demonstrate the aftershock effects on the already damaged bridge (*test k10*). Finally, a seismic test on the non-isolated bridge for beyond-design condition using a 200% ULS accelerogram was executed (*test k12*).

7.2. Isolators and specimens characterization

According to the testing program presented above, in what follows the main results for each test phase will be presented and commented. In particular, the main results on the characterization of the isolators and of the single pier specimens will be firstly introduced. After that the results of the PsD test on the non-isolated and isolated configurations will be presented. Given that during the characterization of the isolators a higher friction coefficient was measured, the PsD test on the isolated configuration was executed using a combination of numerical and physical isolators.

7.2.1 Cyclic characterization of the FPS isolator

In order to characterize the cyclic behaviour of the isolators, several tests were performed (not indicated in Table 7.1): a first group of tests, taking as a guide the paper by (Lomiento et al. 2013), (*tests b22, b23*), and a series of cyclic test with variable velocities and amplitudes.

7.2.1.1 Cyclic tests following the Lomiento et al. procedure

The testing protocol used in the paper of (Lomiento et al.), consisted of two sinusoidal cycles of 200 mm amplitude, repeated at different velocities (peak velocity of the sinus ranged between 0.25 and 1000 mm/s) with a constant vertical load. Between every two-wave pattern and the following, a certain waiting time was imposed in order to avoid

overheating of the device. The authors conclude that the friction coefficient of the isolators is mainly affected by:

1.   A "load effect": The friction coefficient diminishes with the applied vertical load. This effect exists in similar amount at all the velocities for which it can be fully described without need to perform fast tests.

2.   A "cycling effect": The friction coefficient is smaller at the second consecutive cycle due to the temperature rise and this is more visible at higher velocities (over 10mm/s).

3.   A "velocity effect" that increases the friction coefficient at higher velocities. However this effect is sometimes hidden by the cycling (heating) effect that diminishes the friction.

4.   A "breakaway effect" or stick-slip effect that introduces a peak of the friction at the top and bottom of the sinus wave when the velocity is null (static friction coefficient). This last effect does not affect much the energy dissipation of the force-displacement cycle, but may dangerously modify the force demand on the isolated structure.

Having in mind that in the RETRO test campaign, the isolators can be different from the ones used in the paper, similar experiments were carried out within the range of the capacity of the setup. With respect to the tests that were performed before, there are two main differences:

➢ Firstly, the servo-valve of the horizontal actuator was changed for a bigger one in order to achieve higher velocities.
➢ Secondly, a waiting time of 5 minutes was adopted between patterns of different velocities, with constant displacement amplitude and vertical load.

RETRO ELSA [ISOL. at SHORT] (80: Controller Measured)
b22: V=450kN. H=30mm. 2 waves. Lamb=500...5. 13/08/2013
Master A Con 3 X
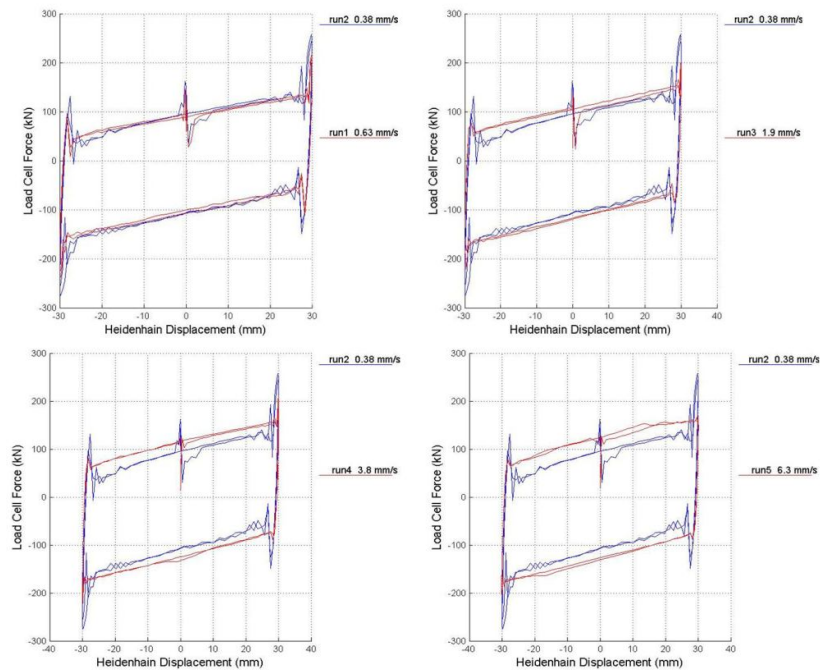
Figure 7.1 Sinusoidal test comparisons of runs at different velocities - *Test b22*

In (Fig. 7.1), the force-displacement loop at 0.38 mm/s is compared with loops at 0.63, 1.9, 3.8 and 6.3 mm/s, showing an increase of the friction at higher velocities. However, the cycling effect is not significantly observed for these velocities. Regarding the breakaway effect, it is quite limited for 6.3 mm/s, and becomes stronger at slower speeds, even though it does not seem to affect the dissipated energy. As a difference with respect to the results shown in the mentioned paper, the breakaway effect is observed here to be double (not only when accelerating from zero, but also when decelerating to zero). The only explanation for this may lay on the control characteristics. A similar test (test b23), was performed using as random pattern a time-history of displacement coming from a numerical simulation performed using the North-South 29 May record

(ULS) gave similar conclusions. An example of a random cycle is shown in (Fig. 7.2).
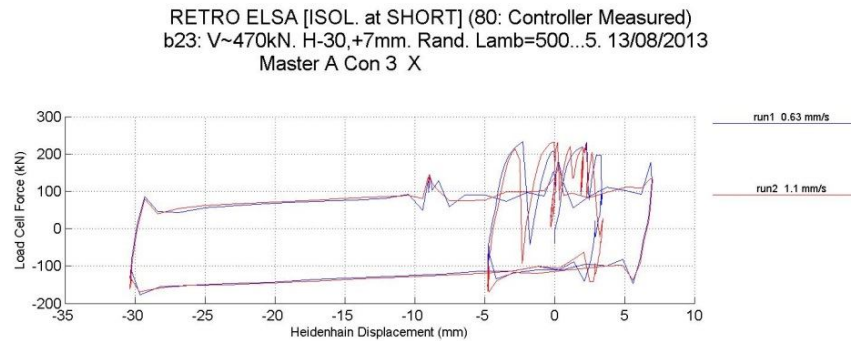
Figure 7.2 Random test comparisons of runs at different velocities - *Test b23*

7.2.1.2 Tests for different cycling velocities and amplitudes

Two types of cyclic tests that were repeated in identical conditions for both isolator setups with a constant vertical load of 450 kN per isolator were performed and compared. The first comparison regards tests b16 and d03 concerning respectively the isolators at the short and tall piers, in which runs of five sine cycles at a constant frequency of 1/100 Hz were imposed with amplitudes of 50, 40, 30, 20 and 10 mm. The maximum velocity at every amplitude ranged from 3.14 to 0.63 mm/s.

The cycles for the magnitudes in the scale of the laboratory and regarding the total horizontal force applied by the horizontal actuator on four isolators with respect to the common horizontal displacement are shown in Fig. 7.3 (for the isolator setup at the short pier) and in Fig. 7.4 (for the isolator setup at the tall pier).

156
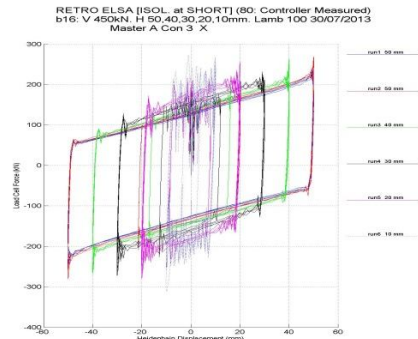
Figure 7.3 Test at variable amplitude, Isolator setup at short pier - *Test b16*
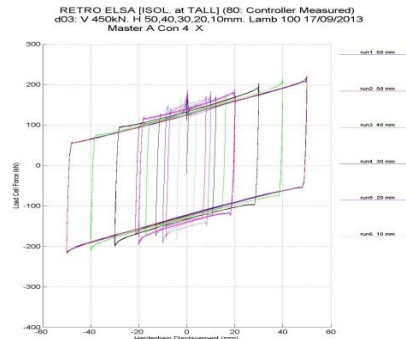
Figure 7.4 Test at variable amplitude, Isolator setup at tall pier- *Test d03*

A second comparison was regarding the tests on isolators at the short (b22) and tall piers (b02) in which trains of two sine cycles at a frequency varying between 1/500…1/5 Hz were imposed with constant amplitude of 30 mm. The maximum velocity at every frequency ranged from 0.63 to 37.7 mm/sec. However, due to the limitations of the testing setup at higher velocities, only the first five runs with frequencies of 1/500 to 1/30 Hz can be considered as valid for the analysis. The cycles obtained are shown in Figure 7.5 and 7.6 for the isolator setup at the short and tall piers, respectively.
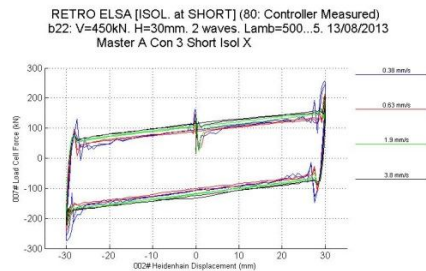
Figure 7. 5 Test at variable frequency, Isolator setup at short pier - *Test b22*
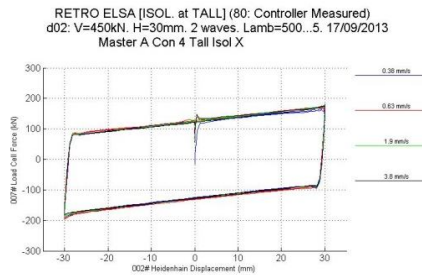
Figure 7.6 Test at variable frequency, Isolator setup at tall pier - *Test b22*

7.2.2 Static characterization of the specimens

The first tests performed on the piers at ELSA served for the identification of the initial stiffness as well as for the tuning of the PID control parameters of the actuators. In test f03, sine cycles of 1.5 mm were applied to the short pier, whereas in test f04, sine cycles of 2 mm were applied to the tall pier.

At the beginning of every test, the vertical load was gradually applied by the vertical actuators controlled in force. At every one of the two columns of the pier, the vertical actuator maintained a force of 450 kN that was constant during the imposition of the horizontal cycles. Several runs of two consecutive horizontal cycles, for the specified constant amplitude were imposed at the head rig of the pier. Eventually, the parameters of the PID controller for the horizontal actuator were changed at every run in order to show the possible effect in the quality of the control. By taking a complete single cycle of the significant runs from both tests, the equivalent linear stiffness and equivalent-viscous damping ratio were identified as shown in Table 7.2 following a standard procedure implemented at ELSA.

Table 7.2 Results of the static characterization of specimens

PIER	test	run	Amplitude (mm)	Stiffness(kN/mm)	Damping ratio
short	f03	3	1.5	11.03	0.0366
short	f03	4	1.5	11.01	0.0364
short	f03	5	1.5	11.00	0.0363
tall	f04	1	2	7.398	0.0393
tall	f04	2	2	7.341	0.0327
tall	f04	3	2	7.315	0.0286

Figure 7.7 and 7.8 show the force-displacement loops at one of the runs of Table 7.2 for piers 9 and 11 by taking the average of the displacement along the axes of both horizontal actuators of each pier and the total force applied by them.
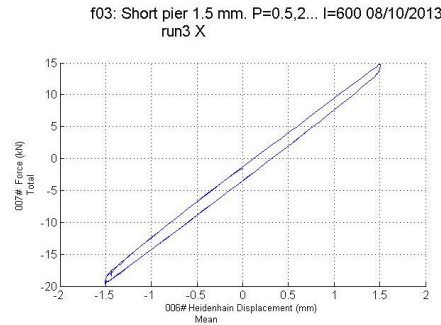
Figure 7.7 Force-displacement loops for short pier - *Test f03*
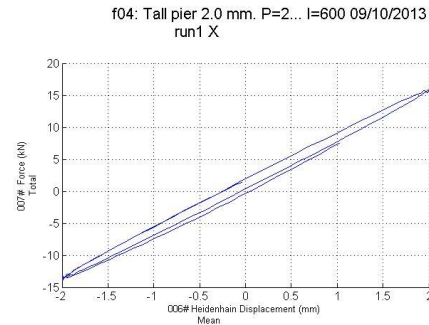
Figure 7.8 Force-displacement loops for tall pier *Test f04*

7.3. PsD test results on the entire viaduct

In this section the results of the PsD test on the entire isolated and non-isolated bridge are presented. The results are presented in terms of global quantities as displacement at the top of each pier and base shear, or in terms of local quantities measured in the specimens during the tests (curvatures or shear deformations, level of bond slip of bars, etc.). The global displacement of the piers is the average of the two horizontal actuators of the pier at the head rig. The represented force is not exactly the total force obtained by the addition of the forces at both actuators. In fact, the figures give the net total force on the pier, which is equal to the total force after removing the recentring horizontal force given by the tensioned dywidag bars inside of the columns of the pier, i.e.,

$$F_{Total}^{Net} = F_{Total} + K_{Geom}D \tag{7.1}$$

where a geometric stiffness *KGeom* (at the laboratory model scale), multiplies the horizontal displacement in order to provide the correction term.

For tests with large displacements k09, k10 and k12, the same kind of correction was used within the PsD algorithm before these forces were introduced as restoring forces within the equation of motion, taking again the values of geometric stiffness provided in Table 7.3 (at the prototype scale in this case).

Taleb 7.3 Geometric stiffness applied at piers

Laboratory model scale values		
Pier	Short (11)	Tall (9)
Height from basement bottom to vertical cylinder bottomH (m)	8	12.5
Total vertical load V (N)	9E+05	9E+05
Geometric stiffness –V/H (N/m)	-112500	-72000
Prototype scale values		
Pier	Short (11)	Tall (9)
Height from basement bottom to vertical cylinder bottom H=2.5*H (m)	20	31.25
Total vertical load V=2.5*2.5*V (N)	5625000	5625000
Geometric stiffness –V/H=–2.5*V/H (N/m)	-281250	-180000

7.3.1. PsD test results on the non-isolated viaduct

Test *k06* test was executed to check all instruments, LVDT sensors and hydraulic actuators; in addition to get an indication of the level of displacements and initial stiffness of the piers.

In test k07 the 100% SLS earthquake was applied on the as-built configuration; the curvature at the bottom section of one of the columns of pier 11 is shown in Figure 7.9. It demonstrates the slight amount of non-linearity in the columns during the test. Same notice could be observed in (Fig. 7.10) which shows the shear deformation of the transverse beam.
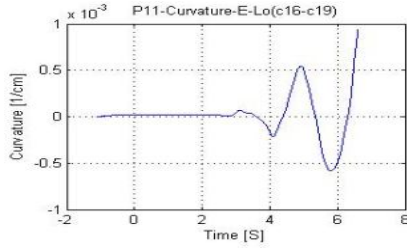
Figure 7.9 Curvature at the bottom section of the left column of pier 11 for *test k07*
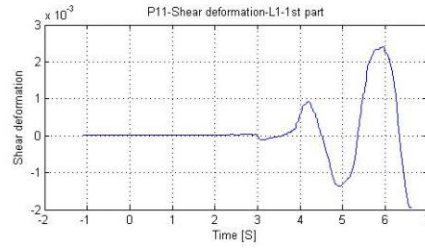
Figure 7.10 Shear Deformation in the transverse beam for *test k07*

In test *k07*, the global behaviour goes beyond the elastic limit, corresponding to the formation of hairline cracks due to shear damage at the transverse beam of piers 11 and 9; to avoid excessive damage in pier 11 the test was stopped at 6.6 s. In fact, the predicted level of displacement for Serviceability Limit State was about 3 cm for the tall pier and 1.6 cm for the short one: during the test the short pier reached a displacement of about 3 cm. This was mainly due to the excessive deformability of pier 11 with respect to the design values. The crack pattern observed after the test was very close to that predicted using the refined model, for which the maximum expected level of shear deformation γ was about 1×10^{-3}, very close to the obtained one.

The experimental curvature χ was evaluated in the as-built configuration with the equation $\chi = (\delta_1/B_1+\delta_2/B_2)/D$ as a function of displacements δ_1, δ_2 and include the slippage effect of rebars. δ_1 and δ_2 were measured by pairs of LVDTs at a distance B_1 and B_2 with respect to the base (Fig. 7.11).
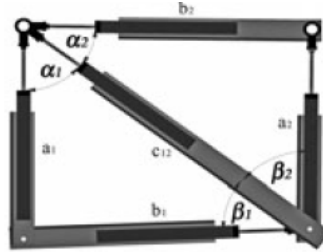
Figure 7.11 Parameters for the evaluation of the curvature in the columns
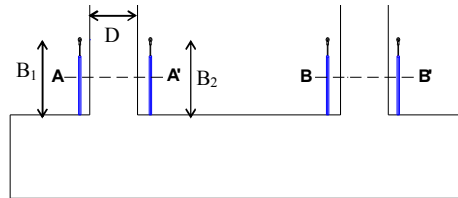
Figure 7.12 Parameters for the evaluation of the shear deformation

The evaluation of the mean value of shear deformation γ may be performed as $\gamma=(\Delta\alpha+\Delta\beta)/2$, whose symbols are indicated in (Fig. 7.12), where the arrangement of the sensors used is also shown. $\Delta\alpha =\alpha_0 - (\alpha_2+\alpha_1)$ and $\Delta\beta=\beta_0 - (\beta_2 +\beta_1)$ are the variations of the angles $\alpha=\alpha_2+\alpha_1$ and $\beta=\beta_2 +\beta_1$ with respect to the initial ones α_0 and β_0.

Similarly, a slight crack at the bottom section of piers 9 and 11 was detected as evidenced by the bond slip measured by the LVDT sensors placed at bottom of the columns. The maximum level of displacement was of the order of 0.2 mm, corresponding to a slight crack opening in the column. The nonlinear behaviour is clearly observed in (Fig. 7.13 and 7.14) which show the force-deflection cycles of pier 9 and 11 respectively for Test k07.
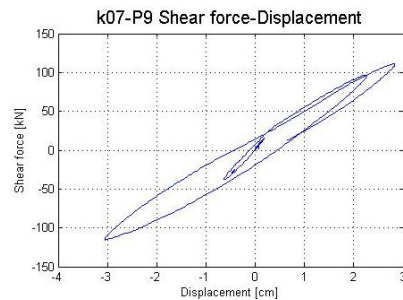
Figure 7.13 Force-Deflection cycle of Pier 9 (SLS PGA=100%) - *Test k07*
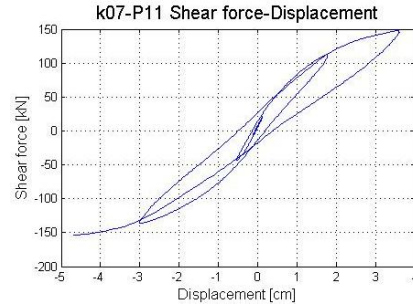
Figure 7.14 Force-Deflection cycle of Pier 11 (SLS PGA=100%) - *Test k07*

The configuration of the non-isolated viaduct was tested at the *k09 test* considering the 100% ULS earthquake. In this test, a significant shear crack pattern was observed in both piers in the transverse beams, in addition to some cracks between the cap beam and the column joints. Base-column opening was also evident during the cycles. Figure 7.15 and 7.16 show the force-deflection cycles, indicating the high non-linearity developed by both piers.
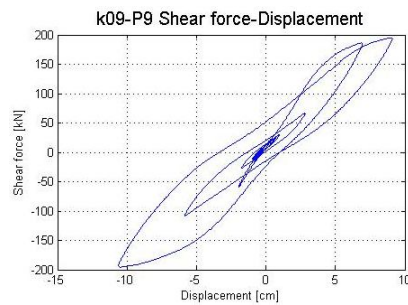
Figure 7.15 Force-Deflection cycle of Pier 9 (ULS PGA=100%) - *Test k09*
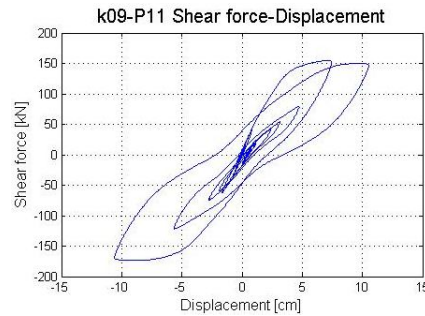
Figure 7.16 Force-Deflection cycle of Pier 11 (ULS PGA=100%) - *Test k09*

The shape of cycles confirm the results obtained during the test campaign carried out at University Roma Tre on 1:4 scale models of pier 12 (similar to pier 11) (Paolacci & Giannini, 2012). In fact, beyond the high deformability of both the piers, the absence of softening characterizes their cyclic behaviour, even for high levels of displacement.

A pronounced pinching phenomenon is also observed. This is mainly due to shear damage in the transverse beams and the large crack opening at the base of columns and the consequent fix-end rotation effect, which is characterized by an alternate closing and opening of cracks and, accordingly, the increase and decrease of stiffness. Similar phenomena can be noticed in the other piers, here simulated only numerically (Fig. 7.17a). The time history of top displacements and shear force of pier 11 is shown in (Fig. 7.17b).

(a)

(b)
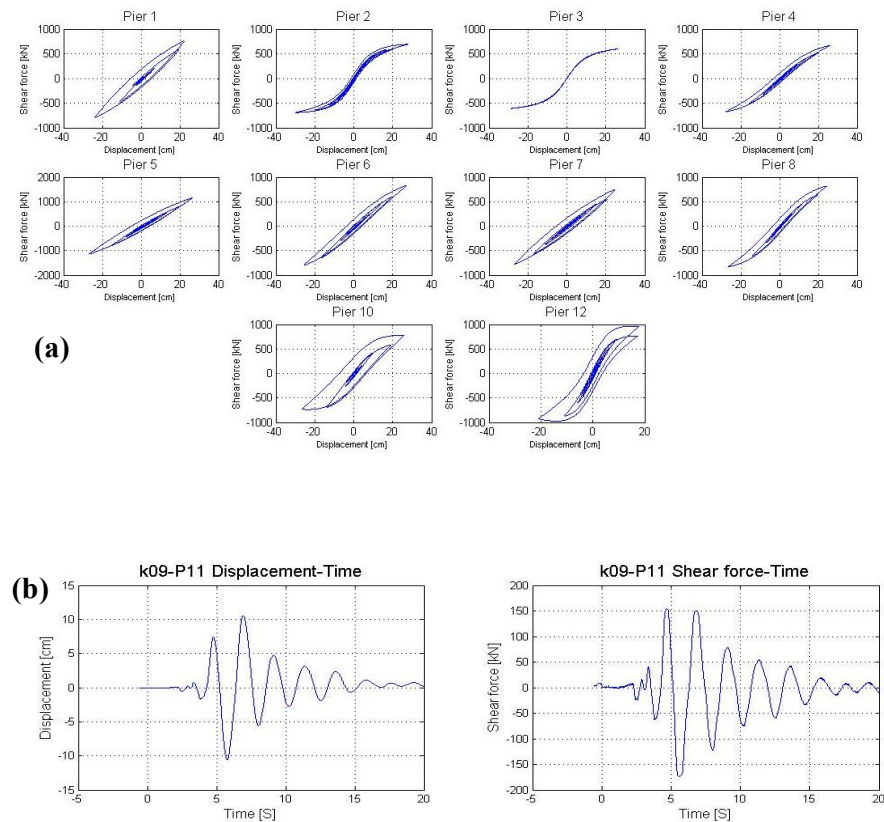
Figure 7.17 (a) Cycles of the remaining (numerical) piers (b) Displacement abd shear force curves - *Test k09*

164

Figure 7.18 Shear cracks pattern in the transverse beam of pier 11 after test k09

The high level of shear damage in the beams and the large amount of crack opening at the base and top of the column are seen clearly in (Fig. 7.18 and 7.19).

In order to assess the aftershock effects on the already damaged bridge, an exact repetition of *test k09* was carried out (*test k10*). The test aimed at verifying the level of degradation of non-linear behaviour and the level of damage of both piers. In addition, this will allow verifying the reliability of the adopted non-linear models in predicting the seismic behaviour of the damaged bridge under aftershocks (Paolacci et al. 2014a)
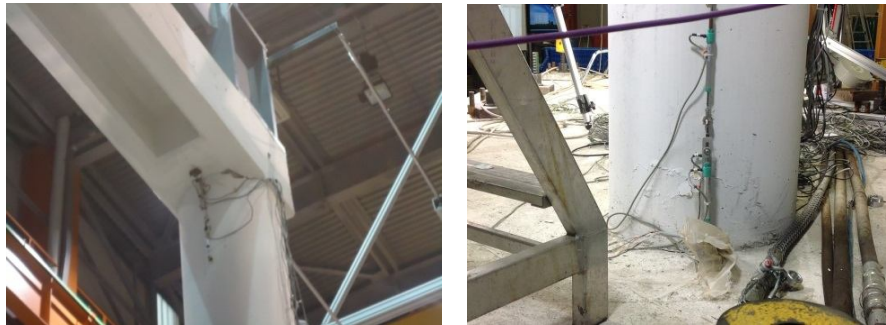
Figure 7.19 Crack opening at the top and bottom of pier 11 after test k09
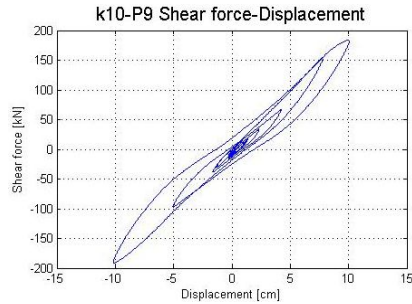
Figure 7.20 Force-Deflection cycle of Pier 9 - *test k10* (Aftershock PGA=100%)
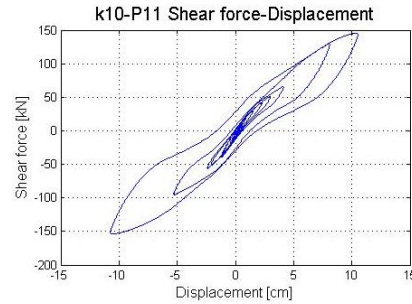
Figure 7.21 Force-Deflection cycle of Pier 11 - *test k10* (Aftershock PGA=100%)

From the test results (see Fig. 7.20 and 7.21), it can be noticed the existence of a general decrease of stiffness due to the increase of the fix-end rotation effect, given by the high slippage of the reinforcing bars at the top and bottom sections of columns. This effect was amplified by large openings of shear cracks in the transverse beams.

Finally, to test the piers in beyond-design conditions and quantify global failure in terms of local and global response, a test with PGA=0.54g (200% ULS) was performed. It is useful to remember that in literature (Alessandri & Giannini, 2013), the drift in shear failure condition of the transverse beams is 2%.
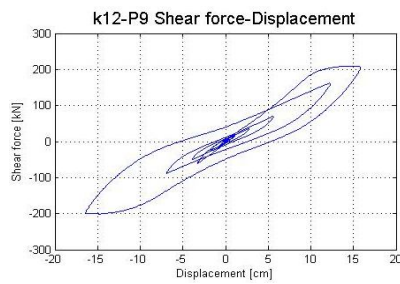
Figure 7.22 Force-Deflection cycle of tall Pier for *test k12* (PGA=200%)
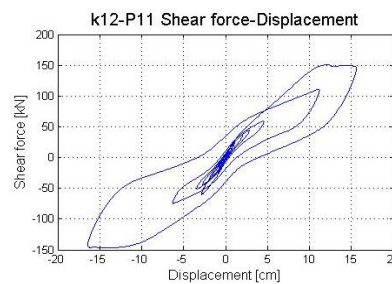
Figure 7.23 Force-Deflection cycle of Pier 11 for *test k12* (PGA=200%)

The hysteretic cycles are shown in (Fig. 7.22 and 7.23). Failure of the pier is confirmed by the maximum drift of 2.4% reached by the short pier. In fact, from the photos shown in (Fig. 7.24 - Fig. 7.28) it is possible to observe an extensive damage condition both for pier 9 and 11, even though the most important damage pattern was experienced in the short pier, especially in the transverse beam, whose typical shear cracking pattern is shown in (Fig. 7.24) and top column-cap beam crack is observed in (Fig. 6.25). A wide zone of cover spalling, characterized by an important buckling effect of the steel bars in the transverse beam of short pier is shown in (Fig. 7.26). A similar effect, even though less important, was present in the transverse beam at the first transverse beam of the tall pier (Fig. 7.27). In fact, only a drift of 1.2% was imposed, corresponding to a severe framework of damage in the transverse beam but far from the ultimate condition. The time-history of shear deformation is shown in (Fig. 7.29), which confirms the above assertions.

This test has also been useful to better appreciate the presence of the fix-end rotation phenomenon. In fact, a very large crack opening at the bottom section of all columns was noticed (Fig. 7.28 b,c). In addition, given the high level of imposed displacements, a slight buckling effect at the left column base of the short pier also took place (Fig. 7.28a). The curvature history of the left column of both piers is shown in (Fig. 10.29). There it can be noticed the high level of non-linearity given a level of curvature higher than the yielding limit.

Figure 7.24 Transverse beam damage on pier 11 after *test k12*

Figure 7.25 Crack opening at the top of a column in the Short pier after *test k12*

Figure 7.26 Blow up of the transverse beam damage on short pier after *test k12*
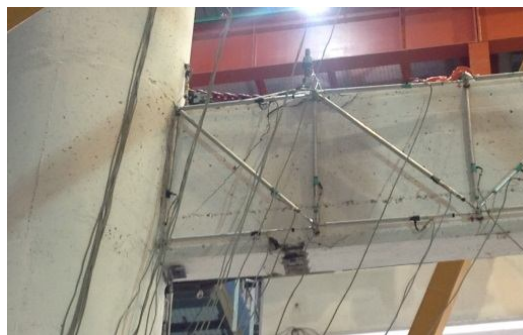
Figure 7.27 Crack pattern in the first transverse beam of tall pier after *test k12*
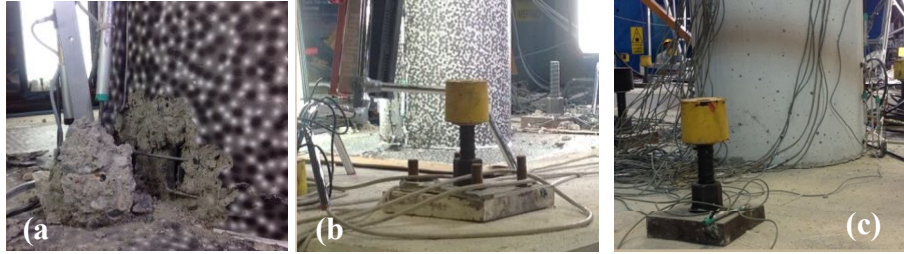
Figure 7.28 Crack opening and buckling phenomena at the bottom section of columns in the Short (a,b) and Tall pier (c) after *test k12*
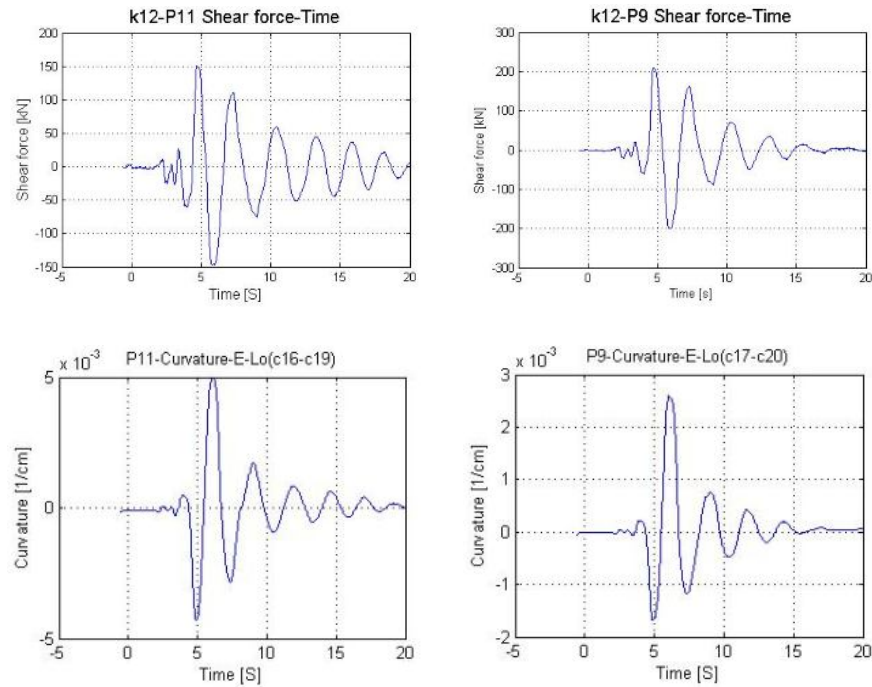
Figure 7.29 Time-History of the shear deformation at transverse beam of Tall (a) and Short pier (b), curvature at bottom section of left column of Tall (c) and Short pier – 200% ULS

All previous cycles are superimposed in (Fig. 7.30 and Fig. 7.31); they demonstrate the global stiffness decreasing effect due to the slippage of plain bars and the consequent fix-end rotation phenomenon. The large

non-linear deformations experienced by the other piers are shown in (Fig. 10.32).
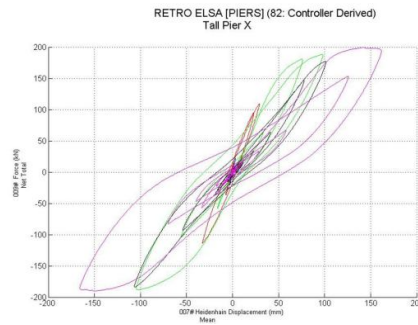
Figure 7.30 Force-Deflection cycles of Tall Pier for various level of testing – non-isolated bridge
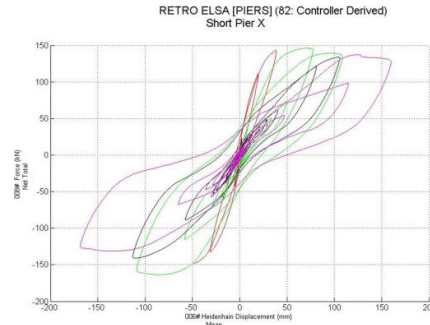
Figure 7.31 Force-Deflection cycles of Short Pier for various level of testing – non-isolated bridge
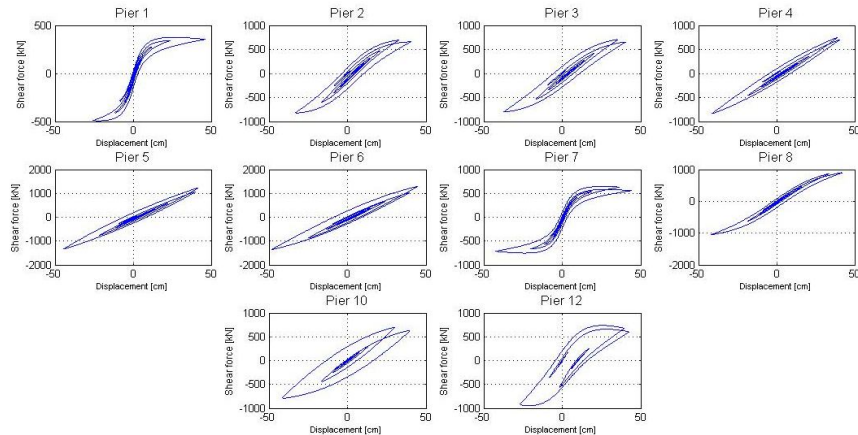
Figure 7.32 Hysteretic cycles of numerical piers – 200% ULS

7.3.2. PsD test results on the isolated viaduct

Several PsD tests were carried out on the isolated viaduct at SLS and ULS. Design and actual values of friction μ for the friction pendulum devices, namely $\mu = 4\%$ and $\mu = 7\%$, were considered along with the numerical and physical piers, respectively. During the tests, only the isolators connected to pier 9 (tall pier) were used as physical devices, as

170

the set of devices connected to pier 11 exhibited an irregular hysteretic response, as discussed in Section 7.2. Physical piers and isolators were considered for tests *l01* and *p02*, which correspond to the 100%SLS and 70% ULS, respectively. These latter tests employ the design value of friction, i.e. 4%. The bridge deck was assumed continuous, i.e. the saddles were eliminated when the isolation system was introduced at the base of the RC deck.

The bridge piers respond elastically when considering the 100%SLS as earthquake input. For example, Figure 7.33 and 7.34 compare the force-deflection cycles of piers 9 and 11 during tests *l01* and *k07*, i.e. considering the bridge system with and without friction isolators, respectively. The effectiveness of the FP bearings in protecting the bridge was proved by (almost) linear behaviour of the physical as well as of the numerical piers at SLS. Transverse beams also exhibited an elastic response at serviceability limit state, as shown by the shear deformation in the lower transverse beam of pier 11 during test l01 (Paolacci et al. 2014a).
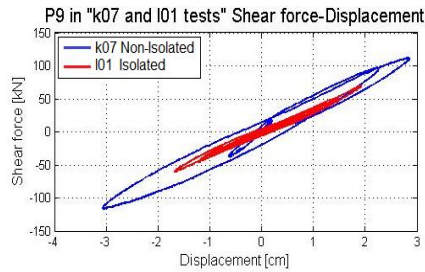
Figure 7.33 Force-Deflection cycle of Pier 9 during tests k07 and l01 (SLS PGA=100%)
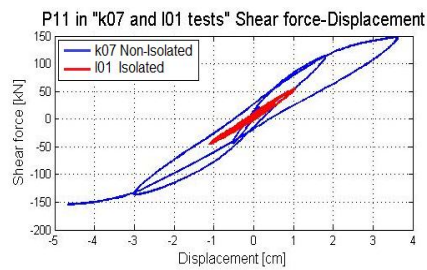
Figure 7.34 Force-Deflection cycle of Pier 11 during tests k07 and l01 (SLS PGA=100%)

The outcomes of the non-isolated bridge, i.e. test *k07*, have also been included as a benchmark. The linear elastic response of the piers stems also from the curvature at the bottom section of left column of pier 11 during test *l01*, and from the shear deformation, as depicted in Fig. 7.35

and Fig. 7.36. The hairline cracks on the transverse beams and at the bottom section of columns which appeared in the non-isolated configuration, namely in test *k07*, were not detected when base isolation devices were employed, i.e. for test *l01* (RETRO final report, 2014).
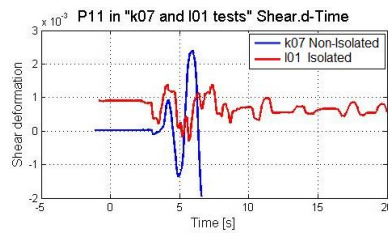
Figure 7.35 Shear Deformation in the lower transverse beam of pier 11 during tests k07 and l01 (SLS PGA=100%)
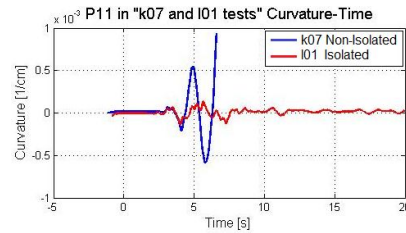
Figure 7.36 Curvature at the bottom section of left column of pier 11 during tests k07 and l01 (SLS PGA=100%)

The high effectiveness of the FP isolators along the entire bridge can be well appreciated in (Fig. 7.37), where the force-deflection cycles for the 100% ULS condition are shown for all the remaining piers in isolated and non-isolated conditions in *k09* and *l02* tests. The quite linear behaviour of all piers for the bridge in the isolated condition demonstrates the effectiveness of the isolation system in reducing the high vulnerability of this kind of bridges.
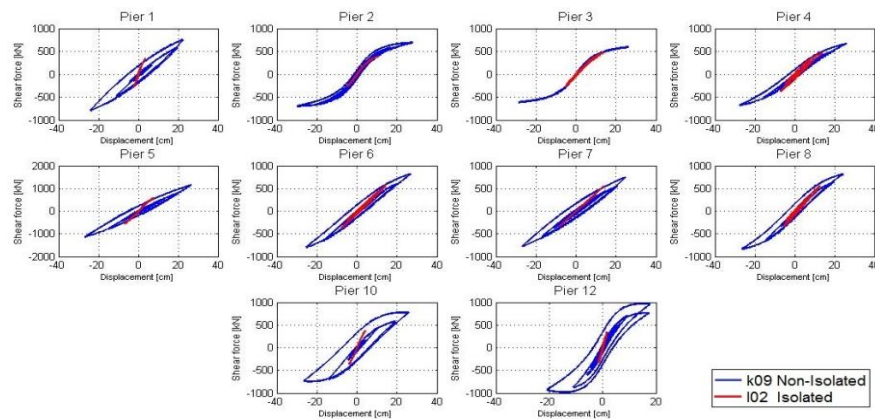
Figure 7.37 Hysteretic cycles of all piers for isolated and non-isolated bridge 100% ULS

Finally, the effectiveness of the isolation system has been also tested using a different configuration, where the physical components of the sample model comprise only isolator of pier 9 connected to that pier, where, as pier 9 and all other piers and isolators, are simulated numerically. For this configuration Tests r01, r02, r03 where performed, which correspond to acceleration equal to 65%, 80% and 90% of ULS, i.e. 0.25g. For such tests, the friction of the isolators is μ=7%; the latter friction value, which is derived experimentally, is significantly higher than the design value, i.e. 4%. From a practical standpoint, it is assumed that the use of higher friction may be caused, for instance, by inadequate selection of the devices, ageing phenomena, defects in the production, etc. The latter are realistic conditions that can occur in several projects.

The experimental response curves for tall and short piers are plotted in Figures 7.38 and 7.39. The force-deformation relationships are linear. The overall numerical shear force-deformation of the rest piers cycles are shown in Figure 7.40 for tests r01, r02 and r03. The figure shows that the behaviour remains linear in all piers.
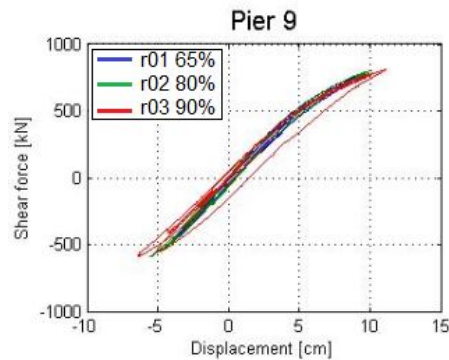
Figure 7.38 Force-Deflection cycle of Pier 9 during tests r01, r02 and r03 (ULS PGA=65%, 80% and 90%)
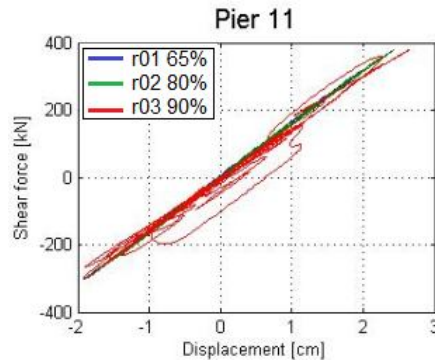
Figure 7.39 Force-Deflection cycle of Pier 11 during tests r01, r02 and r03 (ULS PGA=65%, 80% and 90%)
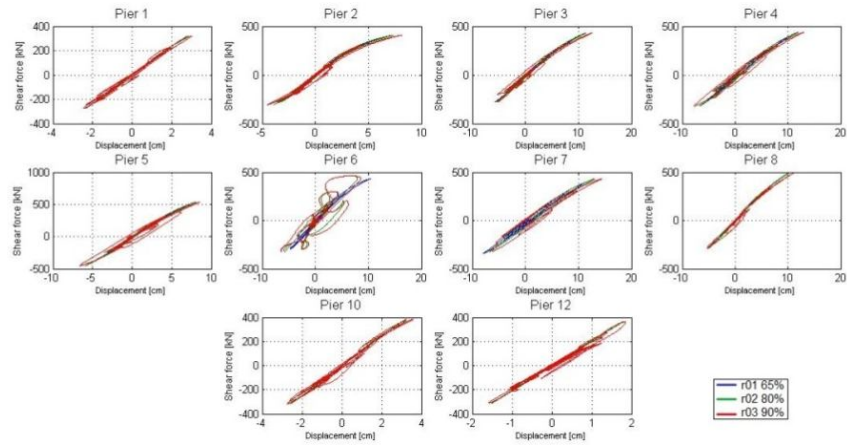
Figure 7.40 Numerical hysteretic cycles of all piers for isolated tests r01 65%, r02 80% and r03 90% respectively, all in ULS

8. CONCLUSIONS

The research study focused on experimental and numerical investigations of old bridges, designed mainly for gravity loads. Towards this aim, the seismic vulnerability of an existing Italian viaduct with portal frame piers (Rio-Torto Viaduct) is evaluated and an isolation system is designed using Friction Pendulum (FP) bearings.

The research has been developed in the framework of a comprehensive experimental test campaign, performed at ELSA Laboratory of JRC (Ipra, Italy). Two large-scale specimens (scale 1:2.5), 2 floors (total height is 7.0 m) and 3 floors (total height is 11.5 m) one-bay RC frame respectively, were built and tested using the PsD technique with sub-structuring. Two configurations of the sample bridge were considered: 1) "as-built" viaduct imposing several damage levels and 2) retrofitted viaduct using friction bearings. Natural records, based on a specific hazard analysis, were selected as earthquake input for the laboratory seismic tests.

In this thesis the main issues regarding the numerical simulation of the seismic response of the Rio- Torto reinforced concrete (RC) viaduct for the PsD test campaign have been presented and discussed. In this respect, both "as-built" and "isolated" configurations have been considered. In particular, a refined three-dimensional finite element (FE) non-linear model for the non-isolated case, developed in OpenSEES, is presented and discussed. Such a model encompasses the non-linear flexural deformations of members, the non-linear shear deformations of transverse beams and the bond-slip that is typically found in of RC structures with plain steel bars. The model has been calibrated on a previous experimental test results carried out at the University Roma Tre on 1:4 scaled specimens.

The refined FE model has been also adapted to simulate the seismic behavior of the deck-isolated bridge equipped with friction pendulum bearings. At this end, a special element already developed in OpenSEES has been used (*single FP Bearing*).

A series of seismic analyses were carried out, for both the "as-built" and the "isolated" configurations, aiming at assessing the bridge response at two different limit states: serviceability and ultimate limit state. The serviceability condition corresponds to the onset of hairline cracks formation in the transverse beam and at the columns base. At the ultimate limit state, the shear failure of the transverse beam and a high crack opening at the columns base occur. Consequently two different accelerograms were selected and used in the simulations. The latter records include the natural strong motions collected during the Emilia earthquake event of 29th May 2012, in Italy.

A detailed local and global response of the "as built" viaduct has been provided. The structural response has been a useful tool to design the PsD test campaign and validate the results comparing the response of the viaduct during the tests with the simulated response.

The simulations of the seismic response of the isolated viaduct showed the effectiveness of the isolators in reducing the stress level in the piers and consequently to reduce the damage level in all members.

A rational dynamic sub-structuring of the OpenSEES refined model of the bridge is presented for both non-isolated and isolated conditions. Reduced S-DoF piers based on Modified Bouc-Wen springs, simulating the global hysteretic responses of the portal frames has also been built. Bilinear state space models substructured isolator pairs, whilst the deck was condensed to its transversal displacement DoFs. Time history analyses of reduced models of the bridge made of substructured parts confirmed the effectiveness of tailored numerical substructures for PsD testing purposes.

During the PsD test campaign, an extensive damage pattern was detected, especially in the short physical pier, where the transverse beam has been subjected to a severe cracking damage due to shear forces. Additionally, a significant fix-end-rotation effect occurred at the base of the pier columns. The latter rotations were caused by the high bond slip effect of plain steel bars. In particular, an extensive damage pattern was detected during the test, starting at the 100% ULS and exacerbated at the 200% ULS, especially in the short pier, where the transverse beam was subjected to severe cracking damage due to shear. In addition, an important fix-end-rotation effect was noticed in both the piers, which comprise a large cracks opening at the bottom section of columns. This is due to the high bond slip effect typical of plain steel bars used for the construction of the specimens. In conclusion, the high vulnerability of the bridge has been fully proved and the need of a proper protection system has been highlighted.

Concerning base isolation, in view of the higher friction coefficient experimentally obtained for the scaled FP devices (7% with respect to the design target value of 4%), to assess the isolated configuration a combination of numerical and experimental sub-structuring of the PFS isolation systems was used to prevent damage in the piers; the reason of this difference is still under investigation. Nevertheless, the effectiveness of the isolation system in protecting the bridge was verified. The isolated bridge responded in a quasi linear-elastic mode at the 100% ULS earthquake: base shear was reduced approximately by half for both piers, and their displacements were reduced in average to 30% and 20% with respect to the "as-built" configuration.

Finally, it is worth to say that the present state-of-art in the field of existing bridges is still need to be improved, it is thus urgent to propose reliable procedures for assessing the seismic vulnerability of existing bridge structures. The goal of supporting seismic codes by comprehensive guidelines for the seismic assessment and retrofit of existing bridges

should be one of the priorities, and the results of this thesis go certainly in this direction.

REFERENCES

1965

- Guyan J (1965) Reduction of stiffness and mass matrices. AIAA,N. 3
- Newmark, N.M., 1965. A method of computation for structural dynamics. Journal of the Engineering Mechanics Division, 3:67-94

1968

- Craig R and Bampton M (1968) Coupling of substructures in dynamic analysis. AIAA, N. 6

1973

- Menegotto M. and Pinto P.E. (1973). Method of Analysis for Cyclically Loaded R.C. Plane Frames Including Change in Geometry and Non-Elements Behaviour of Elements under Combined Normal Force and Bending. Proc. of IABSE Symposium on Resistance and Ultimate Deformability of Structures Acted on by Well Defined Repeated Loads, Vol.13, 1973: 15-22

1983

- FHWA-ATC. "Retrofitting guidelines for Highway Bridges" Report ATC-06-2, Applied Technology Council, Redwood City, California, 1983.

1985

- Dermitzakis S. N. and Mahin. S. A., (1985), Development of substructuring techniques for on-line computer controlled seismic performance testing. Technical report, Earth.Eng. Research Center, Univ. of California, Berkeley, CA, USA, 1985. Report No. UCB/EERC-85/04.

1988

- Krawinkler, H., (1988). "Scale effects in static and dynamic model testing of structures." 9th World Conference on

Earthquake Engineering, Tokyo-Kyoto, Japan, Vol. VIII, 1988; 865–876.

➢ Bazant Z, Sener S. "Size Effect in Pullout Tests." ACI Materials Journal 1988; 5: 347–351

1990

➢ Zayas, V.A., Low, S.S., Mahin, S.A., 1990, A simple pendulum technique for achieving seismic isolation, Earthquake Spectra, 6(2), 317–33.;

1991

➢ Mokha, A., Constantinou, M.C., Reinhorn, A.M., 1991, Experimental study of friction-pendulum isolation system, Journal of Structural Engineering (ASCE), 117(4), 1201–17.

1993

➢ M. Nakashima, T. Akazawa, and O. Sakaguchi. (1993). Integration method capable of controlling experimental error growth in substructure pseudo dynamic test.AIJ J. of Struct. Constr. Engng., 454:61–71.

➢ Millard A. (1993). CASTEM 2000, Guide dutilisation. Saclay, France. Rapport CEA 93/007.

1994

➢ CEN 1994. Eurocode 8—Structures in Seismic Regions—Design—Part 2: Bridges. Comitè e Europaèen de Normalisation: Brussels, 1994.

➢ Priestley M.J.N., Verma R., and Xiao Y., "Seismic Shear Strength of Reinforced, Concrete Columns," ASCE Journal of Structural Engineering, Vol. 120, 8, Aug., 1994, pp. 2310-2329.

1995

➢ FHWA. Seismic Retrofitting Manual for Highway Bridges, Publ. FHWA-RD-94 052, Federal Highway Administration, 1995.

1996

➢ Priestley MJN, Seible F, Calvi GM. (1996). Seismic Design and Retrofit of Bridges. Wiley:New York.

180

1997

➤ Kumar S., Itoh Y., Saizuka K., Usami T. (1997), Pseudodynamic Testing of Scaled Models, Journal of Structural Engineering. 123: 4.

➤ Combescure D. and Pegon P. (1997), α-operator splitting time integration technique for pseudodynamic testing: error propagation analysis. Soil Dynamics & Earthquake Engineering, 16:427–443.

➤ FEMA "NEHRP Guidelines for the Seismic Rehabilitation of Buildings" (1997). Building Seismic Safety Council, BSSC-FEMA publication 237, Washington, DC, USA, 1997.

1998

➤ Vecchio FJ, Collins MP. (1998), "Predicting the response of reinforced concrete beams subjected to shear using the modified compression field theory." ACI Structural Journal; 85(3): 258–268.

➤ Balan T., Filippou FC, Popov EP. (1998), "Hysteretic Model of Ordinary and High Strength Reinforcing Steels". Journal of Structural Engineering, American Society of Civil Engineers 1998; 124(3): 288–297

1999

➤ D'Ambrisi A, Filippou FC. (1999). Modelling of cyclic shear behaviour in RC members.Journalof Structural Engineering ASCE; 125(3): 1143–1150.

➤ Mostaghel, N. (1999). Analytical Description of Pinching, Degrading Hysteretic Systems. Journal of Engineering Mechanics, 125(2), 216–224. doi:10.1061/(ASCE)0733-9399(1999)125:2(216)

2000

➤ Makris, N. and Chang, S. [2000] "Effect of viscous, viscoplastic and friction damping on the response of seismic isolated structures", Earthquake Engineering & Structural Dynamics, Vol. 29, No. 1, pp. 85-107

- Giannini R. (2000), Mathazard: a program for seismic hazard analysis, University Roma Tre
- Bentz EC. (2000). Sectional Analysis of Reinforced Concrete Members", PhD Thesis, Department of Civil Engineering, University of Toronto, 2000, 310

2001

- Verderame G.M., Stella A., Cosenza E., "Le proprietà meccaniche degli acciai impiegati nelle strutture in c.a. realizzate negli anni '60", X Congresso Nazionale L'ingegneria Sismica in Italia, Potenza-Matera 9-13 settembre 2001.
- G. Magonette. (2001), Development and application of large-scale continuous pseudodynamic testing technique. Phil. Trans. R. Soc. Lond. A, 359:1771–1799.
- Gravouil A. and CombescureA.. (2001), Multi-time-step explicit-implicit method for nonlinear structural dynamics. Int. J. Numer. Meth.Engng, 50:199–225.

2002

- Chang S., Makris N., Whittaker E. Thompson A. (2002), Experimental and analytical studies on the performance of hybrid isolation systems, Earthquake EngngStruct. Dyn.31:421–443
- Pegon P and Magonette G., (2002). Continuous PsD testing with non-linear substructuring: presentation of a stable parallel inter-field procedure. JRC-Special publication No.SPI.02.167.
- Hildago PA, Jordan RM, Martinez MP. (2002). An analytical model to predict the inelastic seismic behaviour of shear-wall reinforced concrete structures. Engineering Structures; 24: 85–98.

2003

- Sohn H, Farrar CR, Hemez FM, Shunk DD, Stinemates DV, Nadler BR (2003) A review of structural health monitoring literature: 1996-2001. Los Alamos National Laboratory Report, LA-13976-MS.

➤ Pinto AV, Molina J, Tsionis G., (2003), Cyclic tests on large-scale models of existing bridge piers with rectangular hollow cross-section. Earthquake Engineering and Structural Dynamics 2003; 32(13): 1995–2012.

2004

➤ Ichinose T, Kanayamab AY, Inouec Y, Bolander JE Jr., (2004), Size effect on bond strength of deformed bars. Construction and Building Materials 2004; 18: 549–558.

2005

➤ CEN 2005. Eurocode 8: Design of structures for earthquake resistance – Part 3: Assessment and retrofitting of buildings, 2005.

➤ Fabbrocino G., Verderame G.M., Manfredi G., (2005). Experimental behaviour of anchored smooth rebars in old type reinforced concrete buildings. Engineering Structures27, 1575–1585.

➤ Feldman LR, Bartlett FM. Bond Strength Variability in Pull-out Specimens with plain Reinforcement. ACI Structural Journal 2005; 102(6): 860–867.

➤ Pegon P. and Magonette G. (2005). Continuous PsD testing with non-linear substructuring: using the operator splitting technique to avoid iterative procedures. JRC-Special publication No.SPI.05.30.

➤ Lee DH, Choi E, Zi G. (2005), Evaluation of earthquake deformation and performance for RC bridge piers. Engineering Structures; 27: 1451–1464

2006

➤ FHWA-MCEER. Seismic retrofitting manual for Highway Structures. Part 1- Bridges, 2006.

➤ Fenz, D.M. and Constantinou, M.,C. (2006). Behaviour of the double concave friction pendulum bearing. Earthquake Engineering and Structural Dynamics, 35, 1403-24

➤ Marin, C.C., 2006. Experimental and analytical study of the XY-Friction Pendulum (XY-FP) bearing for bridge

applications, Ph.D thesis, State University of New York at Buffalo, Buffalo, New York

➢ Krawinkler H., Fazin Z., (2006), Simplified Perdormance Based Earthquake Engineering. Technical report, Blume Earthquake Eng Center, Univ. of Satnford, CA, USA, 2006. Report No. 169.

2007

➢ Priestley, M.J.N., Calvi, G.M., Kowalsky, M.J., 2007. Displacement-Based Seismic Design of Structures. IUSS PRESS, Pavia, Italy

➢ Zhao J, Sritharan S. (2007). Modelling of strain penetration effects in fiber-based analysis of reinforced concrete structures. ACI Structural Journal; 104(2): 133–141

➢ Ceresa P, Petrini L, Pinho R. (2007). Flexure-shear fiber beam-column elements for modelling frame structures under seismic loading – state of art. Journal of Earthquake Engineering; 11: 46–88

2008

➢ P. Pegon. Continuous PsD Testing With Substructuring. In O. S. Bursi and D. J. Wagg, editors, Modern Testing Techniques for Structural Systems, Dynamics and Control.CISM, 2008.

➢ Bonelli, A., Bursi O.S., He L., Magonette G., Pegon P. (2008). Convergence analysis of a parallel interfield method for heterogeneous simulations with dynamic substructuring. Int. J. Numer. Meth.Engng, 75:800–825.

➢ Pegon, P., Molina, F. J. and Magonette, G. , 2008, Continuous pseudo-dynamic testing at ELSA. Hybrid Simulation; Theory, Implementation and Applications, ed. SaoumaV.E.andSivaselvan M. V. (Taylor & Francis/Balkema) 79-88.

2009

➢ Pinto P.E., Mancini G., (2009), Seismic assessment and retrofit of existing bridges, The state of Earthquake

Engineering Research in Italy: the ReLUIS-DPC 2005-2008 Project, 111-140, © 2009 Doppiavoce, Napoli, Italy.

➢ Verderame GM, Ricci P, De Carlo G, Manfredi G. Cyclic bond behaviour of plain bars. Part I: Experimental investigation, Construction and Building Materials 2009; 23(12): 3499–3511.

➢ Verderame GM, Ricci P, De Carlo G, Manfredi G. Cyclic bond behaviour of plain bars. Part II: Analytical investigation. Construction and Building Materials 2009; 23(12): 3512–3522

➢ Marefat M.S., Masood S., Shirazi H., Rostamshirazi R., Khanmohammadi M., (2009), Cyclic Response of Concrete Beams Reinforced by Plain Bars, Journal of Earthquake Engineering, 13:463–481.

➢ Pinto PE, Mancini G. Seismic assessment and retrofit of existing bridges. Final Report, Reluis DPC project, 2005–2009, (2009). (http://www.reluis.it)

2010

➢ Paolacci, F., Mohamad, A., (2010). Preliminary considerations on the seismic behaviour of the Rio-TortoViaduct. RETRO' project, Report n°1, 2010

➢ Schellenberg A. (2010). Single Concave Friction Pendulum Bearing Element. Opensees Wiki. Available at http://opensees.berkeley.edu/wiki/index.php/Single_ Concave_Friction_Pendulum_Bearing_Element Date last accessed, Dec. 31th 2012

2011

➢ Fernandes C., Melo J., Varum H., Costa A., (2011), Cyclic behaviour of a two-span RC beam built with plain reinforcing bars, Civil Engineering 55/1 (2011) 21–29, doi: 10.3311/pp.ci.2011-1.03

➢ De Risi, R., Di Sarno, L., Della Corte, G., Paolacci F., Marioni A., and Taucer, F. (2011). Seismic analysis and retrofitting of an existing RC highway bridge Part II: Analysis of the isolated

bridge. Proceedings of the 14th Italian National Conference on Earthquake Engineering, Bari, CD Rom.

2012

➢ Bursi, O. S., Ceravolo, R., Erlicher, S. and ZanottiFragonara, L. (2012), Identification of the hysteretic behaviour of a partial-strength steel–concrete moment-resisting frame structure subject to pseudodynamic tests. Earthquake Engng. Struct. Dyn., 41: 1883–1903. doi: 10.1002/eqe.2163.

➢ Paolacci, F. and Giannini, R. (2012), An experimental and numerical investigation on the cyclic response of a portal frame pier belonging to an old reinforced concrete viaduct. Earthquake Engng. Struct. Dyn., 41: 1109–1127. doi: 10.1002/eqe.1175

2013

➢ Arani, K.K., Marefat, M.S., Di Ludovico, M., Prota, A., Manfredi, G., (2013), Hysteretic cyclic response of concrete columns reinforced with smooth bars, Bulletin of Earthquake Engineering 11 (6) , pp. 2033-2053

➢ Alessandri, S., Corritore, D., Derisi, R., Di Sarno, L., Mohamad, A.,Paolacci, F., Yenidogan, C., (2013). Numerical Simulation of the Siesmic response of the Rio-Torto Viaduct for PsD test Compaigon. RETRO' project, Report n°2, 2013

➢ Della Corte, G., De Risi, R., Di Sarno, L., (2013), Approximate method for transverse response analysis of partially isolated bridges, Journal of Bridge Engineering 18 (11) , pp. 1121-1130

➢ Lomiento G., Bonessio N. and Benzoni G., (2013), Journal of Earthquake Engineering (2013): Friction Model For Sliding Bearings Under Seismic Excitation, DOI: 10.1080/13632469.2013.814611.

➢ Alessandri, S., Giannini, R. and Paolacci, F. (2013), Aftershock risk assessment and the decision to open traffic on bridges. Earthquake Engng. Struct. Dyn., 42: 2255–2275. doi: 10.1002/eqe.2324

2014

- ➤ Paolacci F., Pegon P., Molina F., Poljansek M., Giannini R., Di Sarno L., Abbiati G., Mohamad A., Bursi O., Taucer F., Ceravolo R., Fragonara L., De Risi R., Sartori M, Alessandri S., Yenidogan C., (2014). Assessment of the Seismic Vulnerability of an RC Viaduct with Frame Piers and Study of the Effectiveness of Different Isolation Systems through Pseudodynamic Tests on a Large Scale Model. "RETRO". SERIES Project No: 227887. TA Final Report.

- ➤ Paolacci F., Di Sarno L., Pegon P., Molina F. J., Poljansek M., Bursi O.S., Abbiati G., Ceravolo R., Erdik M., De Risi R., Mohamad A. (2014a), Assessment of the seismic behaviour of a retrofitted old R.C. highway bridge through PsD testing. SERIES Concluding Workshop - Joint with US-NEES "Earthquake Engineering Research Infrastructures", JRC-Ispra, May 28-30, 2013.

- ➤ Paolacci F., Di Sarno L., De Risi R., Abbiati G., Mohamad A., Malena M., Corritore D. (2014b). Refined and Simplified Numerical Models of an Isolated Old Highway Bridge for PsD testing. Joint with US-NEES "Earthquake Engineering Research Infrastructures", JRC-Ispra, May 28-30, 2013.

APPENDIX A – Photographic of mock up's construction

Figure A.1 Foundation Steel work

Figure A.2 Longitudinal and spiral steel in the columns

Figure A.3 Transversal beam construction

Figure A.4 Concrete pouring on beams

Figure A.5 Prestressing bars at top of the piers

Figure A.6 Completed Construction piers

Figure A.7 Piers inside ELSA lab

Figure A.8 Connecting hydraulic actuators at the top of piers

APPENDIX B-1 – Isolated configuration – response to 29th May 2011 (WE component) Emilia Earthquake (SDC)
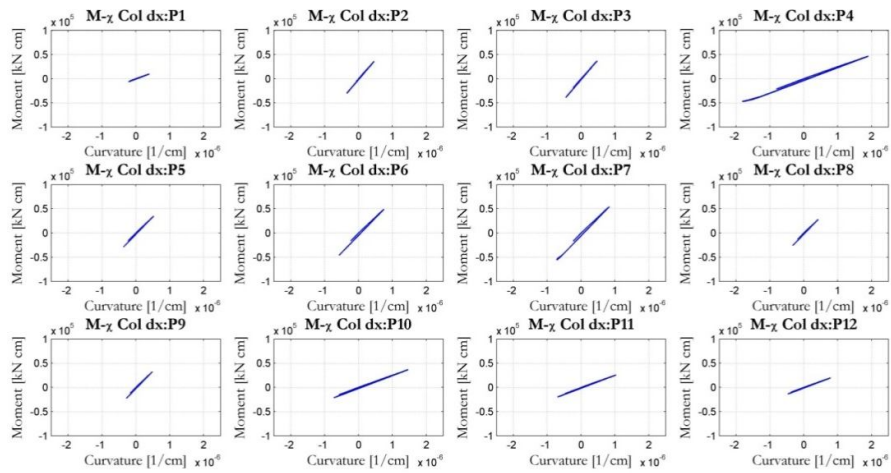
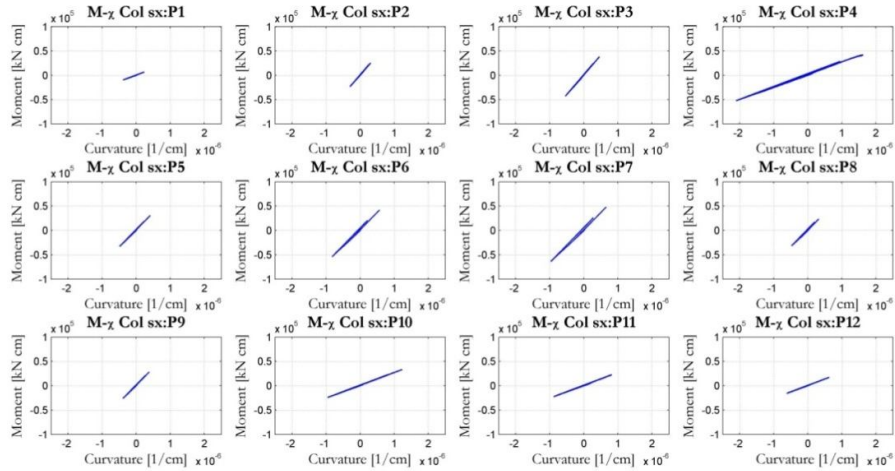Figure A1 - Moment-Curvature for the right column of the pier.

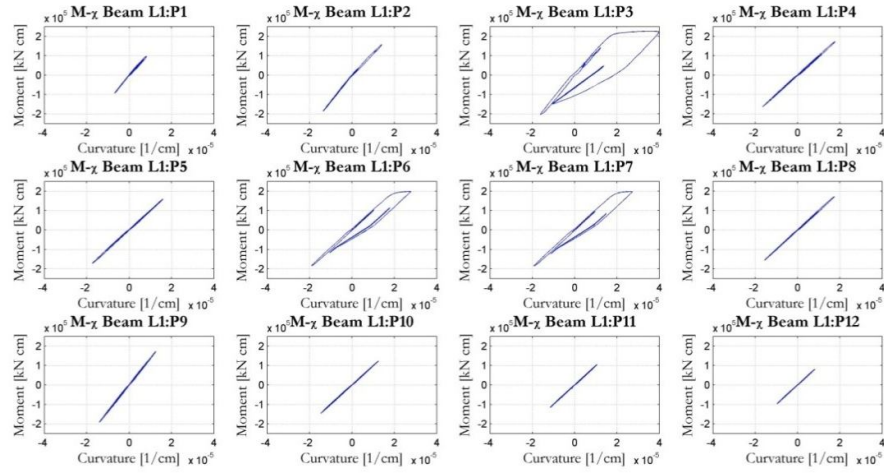Figure A2 - Moment-Curvature for the left column of the pier.

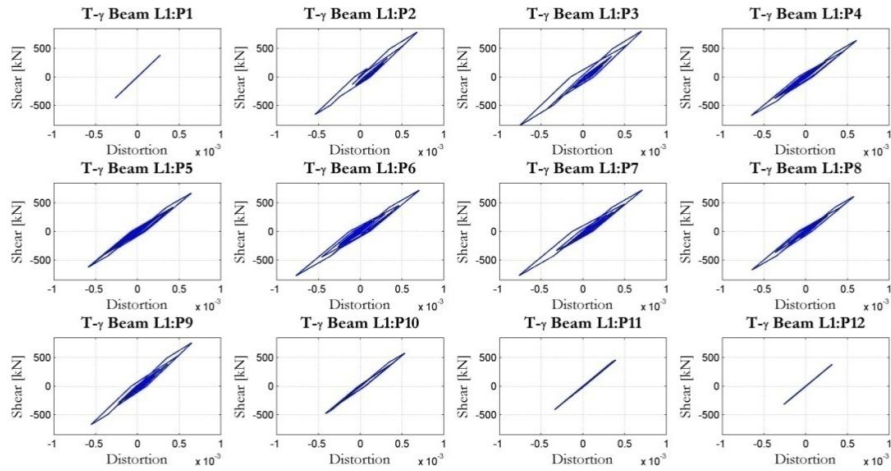**Figure A3 - Moment-Curvature for the transverse beam at first level.**

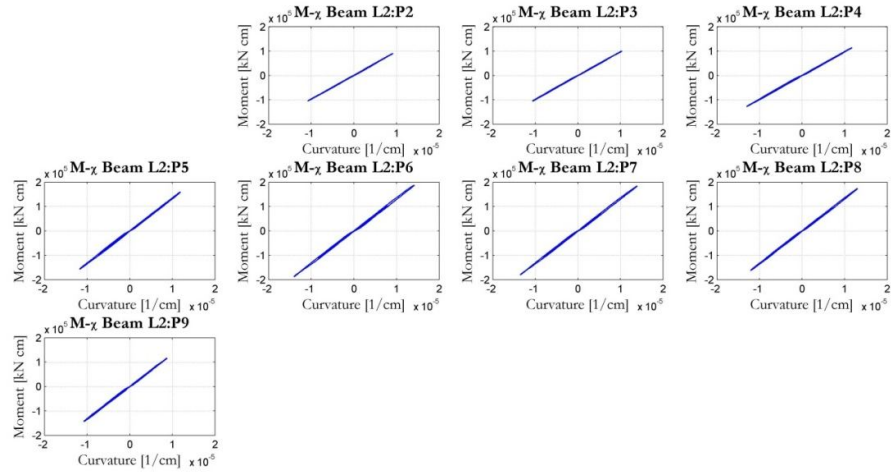**Figure A4 - Shear-Distortion for the transverse beam at first level.**

Figure A5 - Moment-Curvature for the transverse beam at second level.

Figure A6 - Shear-Distortion for the transverse beam at second level.

Figure A7 - Moment-Curvature for the transverse beam at third level.

Figure A8 - Shear-Distortion for the transverse beam at third level.

APPENDIX B: Isolated configuration – response to 29th May 2011 (NS component) Emilia Earthquake (ULS)
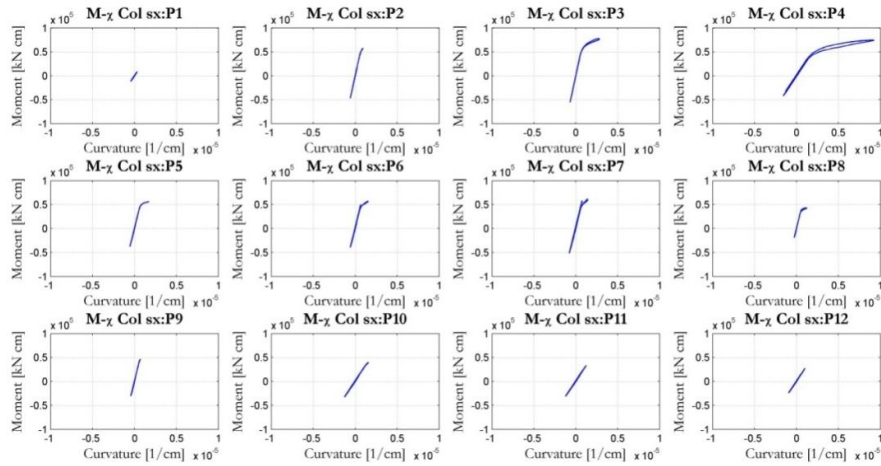
Figure B1 - Moment-Curvature for the right column of the pier.
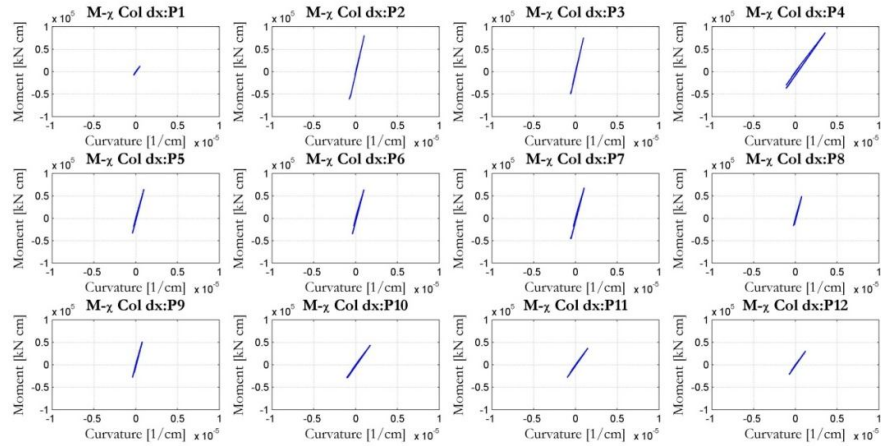
Figure B2 - Moment-Curvature for the left column of the pier.
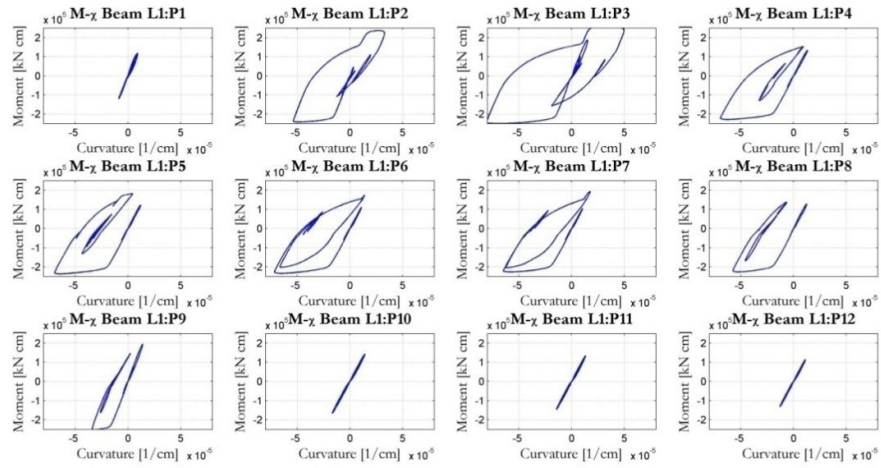
Figure B3 - Moment-Curvature for the transverse beam at first level.
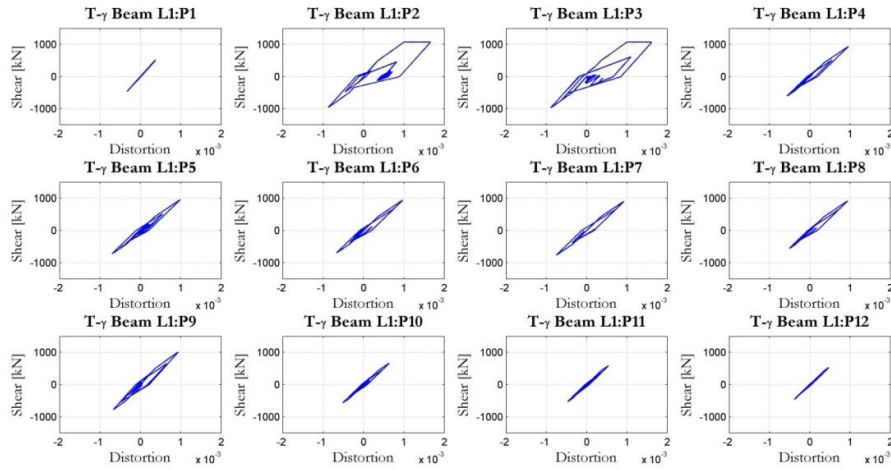
Figure B4 - Shear-Distortion for the transverse beam at first level.
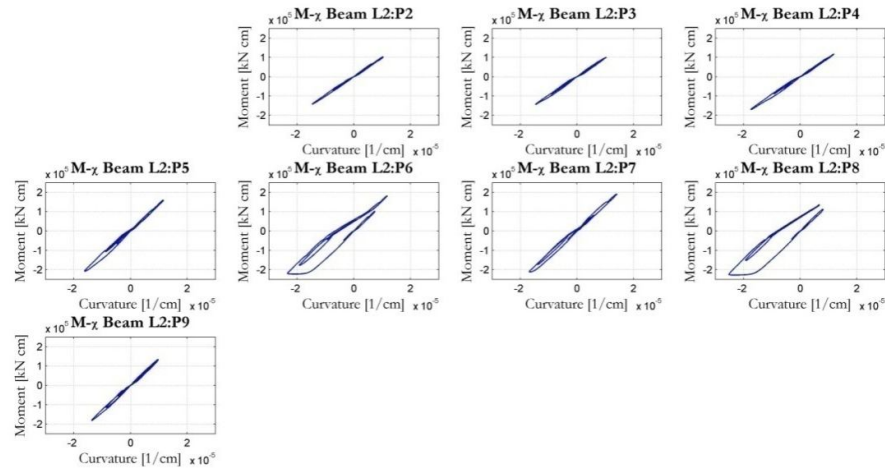
Figure B5 - Moment-Curvature for the transverse beam at second level.
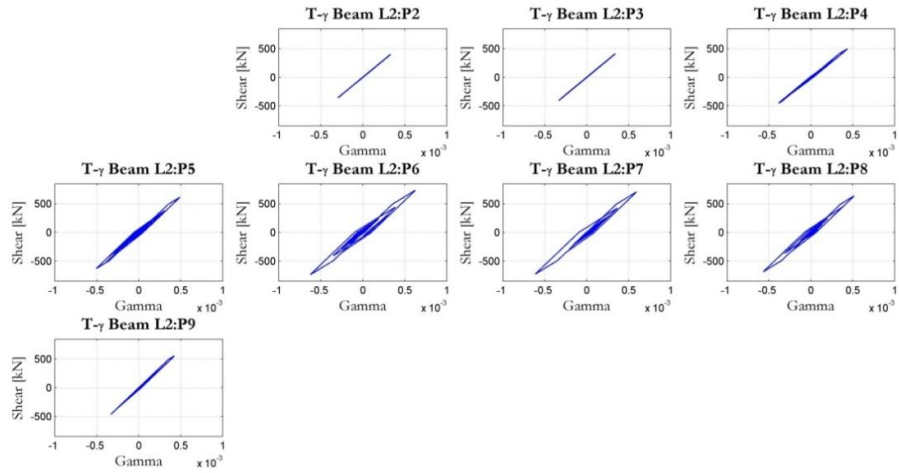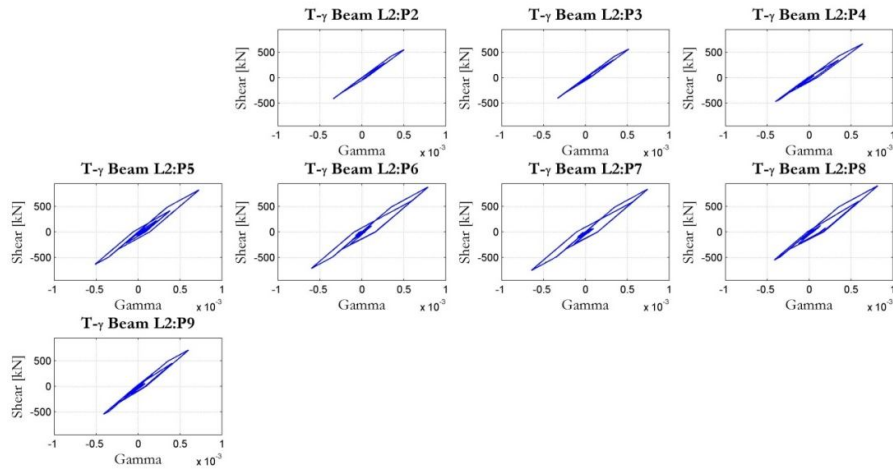

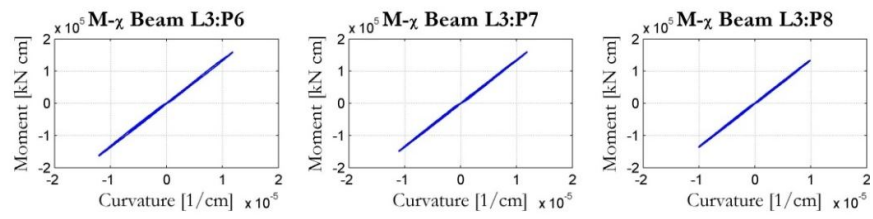**Figure B6 - Shear-Distortion for the transverse beam at second level.**

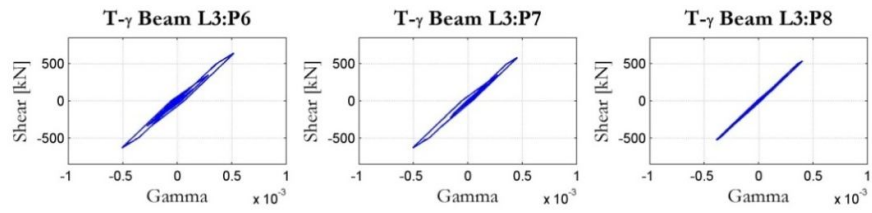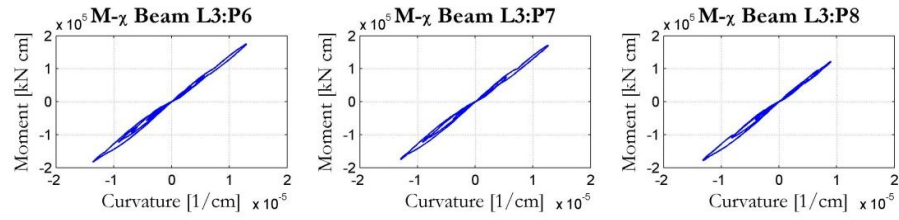**Figure B7 - Moment-Curvature for the transverse beam at third level.**
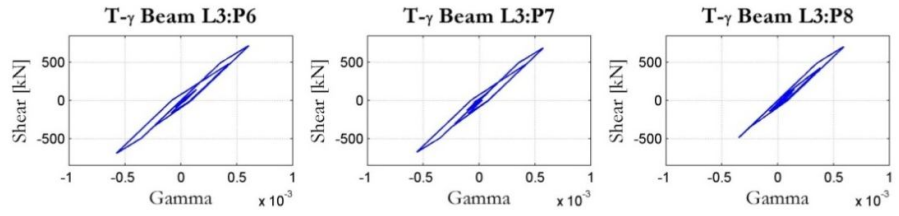
Figure B8 - Shear-Distortion for the transverse beam at third level.

APPENDIX C: MOCK-UP DRAWINGS

Pier 9 : overall dimensions

Table : 1

PIER 9

Section B-B

158
252
48
84 148 84
268
64 60 64
188
284
60
310
1150
1030
120
174 252 174
600

Section A-A

64
1030
1150
120
108 64 108
280

600
50 100 100 100 100 100 50
40
100
280
252
B B
100
40
64 64
Tube ⌀ 125 for passing prestressing bar
Tube ⌀ 125 for passing prestressing bar

Plane view

Description of tables for pier 9

Table : 2

PIER 9

252

48

268

60

284

1030

1150

310

120

174   252   174

600

Reinforcement layout of cap beam = TABLE 3

Reinforcement layout of 2nd transverse beam = TABLE 4

Reinforcement layout of 1st transverse beam = TABLE 5

Reinforcement layout of foundation = TABLE 6

Reinforcement layout of columns = TABLE 7

Reinforcement layout of cap beam

Table : 3

TOP BEAM PIER 9

Section E-E

Pos. 27 1+1Ø4/10 cm L = 68 cm

Pos. 16 e pos 23
314
1+1#8 Ltot=306 cm (upper and lower for each stem)

Pos. 17
296
17#4 Ltot=306

Pos. 18
130   130
1+1#8 Ltot=331 cm (for each stem)
130   40   130

Pos. 19   Pos. 19
98   98
1+1#8 Ltot=179 cm (for each stem)   1+1#8 Ltot=179 cm (for each stem)
32   66   40   40   66   32

Pos. 20   Pos. 20
56   56
2+2#8 Ltot=137 cm (for each stem)   2+2#8 Ltot=137 cm (for each stem)
24   32   40   40   32   24

Pos. 21   Pos. 21
48   32   48
6#8 Ltot=205 cm   6#8 Ltot=205 cm

Pos. 22   Pos. 22
56   56
5#4 Ltot=168 cm   5#4 Ltot=168 cm
56   56

Pos. 28 1Ø4/10 cm L = 108 cm

Pos. 29 16Ø4 L = 184 cm

Pos. 30 1Ø4/10 cm L = 26 cm

Section D-D

Hole Ø 125 for prestressed bar   Hole Ø 125 for prestressed bar

Reinforcement layout of 2nd transverse — Table : 4

Reinforcement layout of 1st transverse

Table : 5

Reinforcement layout of foundation

Table : 6

DETAIL 1

Anchor bars "Dywidag"

Plane view

Hole Ø125
Hole Ø75

206

Reinforcement layout of colums — Table: 7

Pier 11 : overall dimensions

Table : 8

PIER 11

Section B–B

Section A–A

Plane view

Tube φ 125 for passing prestressing bar

Tube φ 125 for passing prestressing bar

Description of tables for pier 11
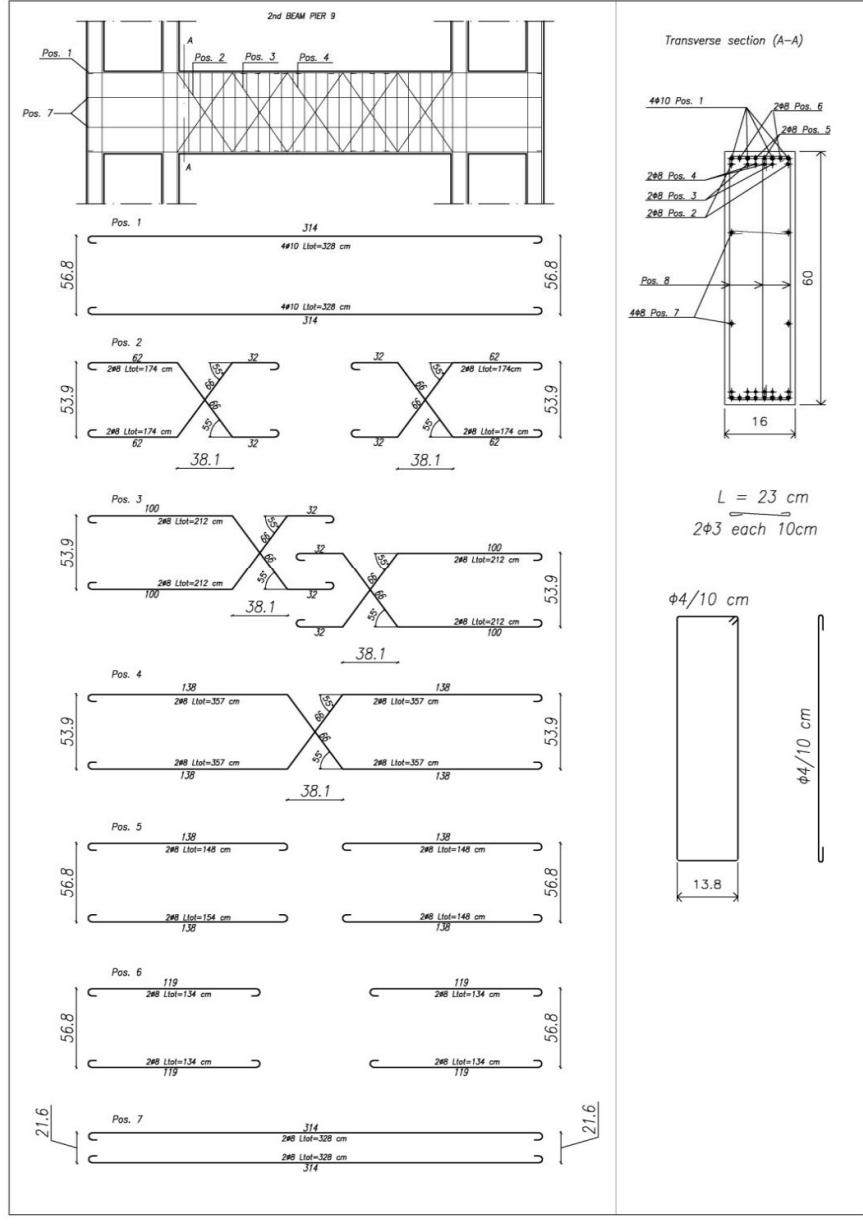
Table : 9

PIER 11

Reinforcement layout of cap beam = TABLE 10

Reinforcement layout of 1st transverse beam = TABLE 11

Reinforcement layout of foundation = TABLE 12

Reinforcement layout of columns = TABLE 13
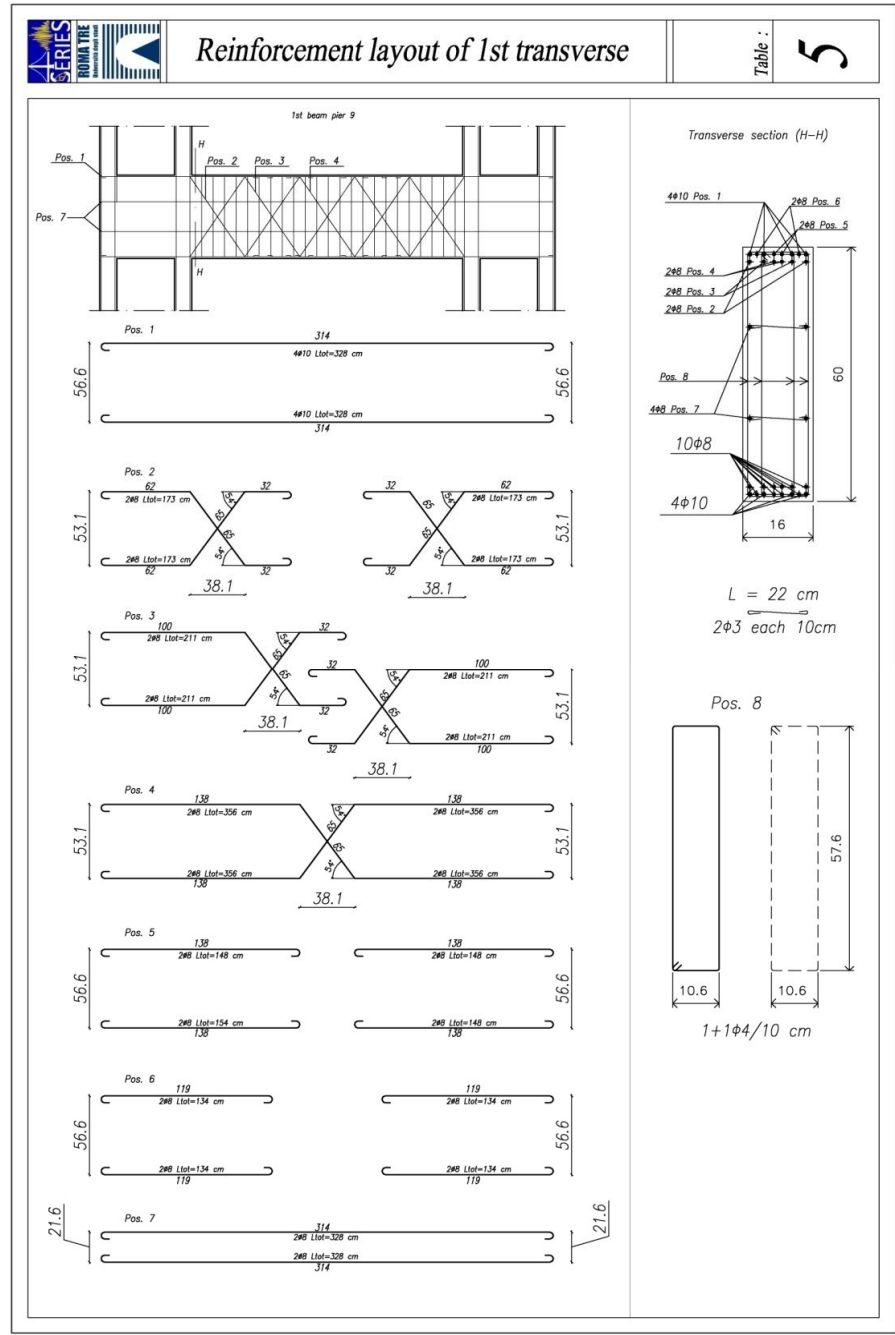
300
252
48
242
48
580
242
174
252
174
600

Reinforcement layout of cap beam — Table: 10
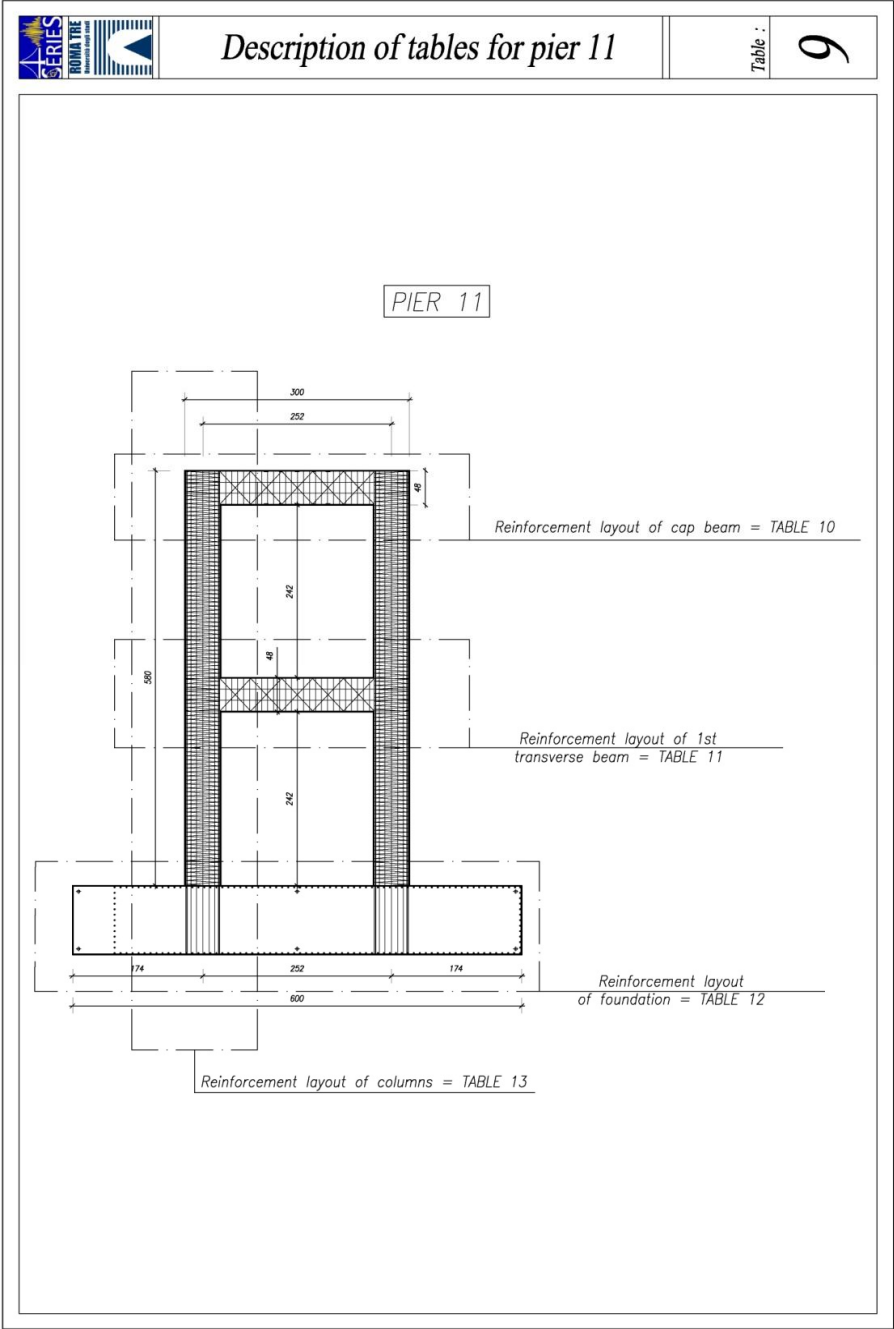
Reinforcement layout of 1st transverse — Table: 11

Reinforcement layout of foundation

DETAIL 1

Anchor bars "Dywidag"

Plane view

Hole ø125   Hole ø75

Hole ø125 for prestressing bar

Table ø125 for prestressing bar

* Ribbed bars B460C

Reinforcement layout of colums

Table : 13

48

48

Section B-B

16ɸ8
Pos. 16

2ɸ8

Tube ɸ 125
for passing
prestressing
bar

48

B   B

STEEL COLUMN

398
16ɸ8 Ltot=410 cm

160
16ɸ8 Ltot=172 cm

354
16ɸ8 Ltot=375 cm

196
16ɸ8 Ltot=208 cm

Cylindrical stirrups ɸ 3/5.6 cm

45.6

5.6

Hooke detail

4 cm

2.4 cm

Tube ɸ 125 for
passing
prestressing
bar